Application of Mixture Theory to solid tumors and normal pressure hydrocephalus

by

Andrijana Burazin

A thesis
presented to the University of Waterloo
in fulfillment of the
thesis requirement for the degree of
Doctor of Philosophy
in
Applied Mathematics

Waterloo, Ontario, Canada, 2013

I hereby declare that I am the sole author of this thesis. This is a true copy of the thesis, including any required final revisions, as accepted by my examiners.

I understand that my thesis may be made electronically available to the public.

Abstract

In this Thesis, the theory of poroelasticity, namely the Mixture Theory version – a homogenized, macroscopic scale approach used to describe fluid flow through a porous medium – is employed in three separate cases pertaining to a biological phenomenon.

The first investigation explores the behavior of interstitial fluid pressure (IFP) in solid tumors. Thus, in Chapter 2, a Mixture Theory based approach is developed to describe the evolution of the IFP from that in a healthy interstitium to the elevated levels in cancerous tumors. Attention is focused on angiogenesis, a tightly regulated process in healthy tissue that provides all necessary nutrients through the creation of new blood vessels. Once this process becomes unruly within a tumor, angiogenesis gives rise to an abnormal vasculature by forming convoluted and leaky blood vessels. Thus, the primary focus of the model is on the capillary filtration coefficient and vascular density as they increase in time, which in turn elevates the tumor IFP. Later, the Mixture Theory model is extended to simulate the effects of vascular normalization, where the cancer therapy not only prunes blood vessels, but reverts the chaotic vasculature to a somewhat normal state, thereby temporarily lowering the tumor IFP.

In Chapter 3, the validity of an assumption that was made in order to facilitate the mathematical calculations is investigated. In addition to all of the Mixture Theory assumptions, it is assumed that the pore pressure p is proportional to the tissue dilatation e. This assumption is examined to determine how appropriate and accurate it is, by using a heat type equation without the presence of sources and sinks under the assumption of a spherical geometry. The results obtained under the proportionality of p and e, are compared with the results obtained without this assumption. A substantial difference is found, which suggests that great care must be exercised in assuming the proportionality of p and e.

The last application is reported in Chapter 4 and it investigates the pathogenesis of normal pressure hydrocephalus. In a normal brain, cerebrospinal fluid (CSF) is created by the choroid plexus, circulates around the brain and the spinal cord without any impediment, and then is absorbed at various sites. However, normal pressure hydrocephalus occurs when there is an imbalance between the production and absorption of CSF in the brain that causes the impaired clearance of CSF and the enlargement of ventricles; however, the ventricular

pressure in this case is frequently measured to be normal. Thus, a mathematical model using Mixture Theory is formulated to analyze a possible explanation of this brain condition. Levine (1999) proposed the hypothesis that CSF seeps from the ventricular space into the brain parenchyma and is efficiently absorbed in the bloodstream. To test this hypothesis, Levine used the consolidation theory version of poroelasticity theory, with the addition of Starling's law to account for the absorption of CSF in the brain parenchyma at steady state. However, the Mixture Theory model does not agree with the results obtained by Levine (1999) which leads one to conclude that the pathogenesis of normal pressure hydrocephalus remains unknown.

To conclude the Thesis, all three applications of Mixture Theory are discussed and the importance and contribution of this work is highlighted. In addition, possible future directions are indicated based on the findings of this Thesis.

Acknowledgements

Dr. Tenti has been a great inspiration throughout my PhD journey at UW, and I will forever be indebt and grateful to him for his mentoring. He has enlightened me with knowledge and has encouraged me throughout the good times and the bad times to become more self-confident. None of my efforts, especially this thesis, would have been possible without him.

Dr. Sivaloganathan with his good spirits and sense of humor always had a calm demeanor in any situation. I will forever admire his dedication to the Biomedical research group - in the way he bridges multidisciplinary research to tackle biomedical problems. And thus, this thesis would not have been the same without his editing and piecing of ideas together.

I would like to thank all the past and present members of the Biomedical research group. You have helped me grow - academically and non-academically alike. I wish you all the best in your future endeavors.

Helen Warren, you have been a wonderful help and very motherly, especially when I had my conundrums and odd ends to figure out. Stephanie Evers, you have been awesome, and I truly appreciated our conversations.

To my loving family, this definitely would not have been easy without you all! Thanks Chris for your support and being there, and of course, for your alma mater card.

For dd.

Contents

List of Tables

List of Figures

Chapter 1

Introduction

The aim of this Thesis is to report the results of three separate investigations with a common theme – the application of the theory of poroelasticity via the Mixture Theory approach, to biological tissue.

The first application – reported in Chapter 2 – is of interest to oncological research, as it investigates the behavior of interstitial fluid pressure (IFP) in solid tumors. For quite a long time, IFP has been known to be higher than the hydrostatic pressure of healthy interstitium. Young et al. (1950) claimed that the IFP may be an essential factor in the dissemination of malignant tumors. Their experimental results showed that the IFP of tumors is higher than that of normal tissue. This phenomenon has been confirmed by other studies of solid tumors (Guillino et al., 1964), also covering many types of cancers such as breast carcinoma (Less et al., 1992; Nathanson and Nelson, 1994), metastatic melanoma (Curti et al., 1993; Boucher et al., 1991), and neck carcinoma (Gutman et al., 1992). In spite of the advances, the mechanism responsible for the increased IFP remained obscure.

A breakthrough in understanding the elevated IFP phenomenon occurred when Jain (1987a, 1987b) identified a key problem in cancer treatment. He claimed that due to the increased IFP, therapeutic agents are not distributed adequately and uniformly within a tumor. Once administered, the drug agents were found to be located around the blood vessels and in some instances in abundance within the outer edge of the tumor. Consequently, no desired therapeutic effects occurred in the center of the tumor. Baxter and Jain (1989) suggested that the elevated IFP, acting as an adverse pressure gradient, limits the transport in tumors. This, in turn, causes a reduction of the driving force for transvascular exchange of both fluid and macromolecules.

To describe the IFP behavior in a solid tumor, Baxter and Jain (1989) developed a mathematical model. Macroscopically, the solid tumor is modeled as spherical in shape,

homogeneous, tissue-isolated, and without a necrotic core. The tumor interstitium is viewed as a rigid porous medium where the fluid flow is regulated by Darcy's law. Assuming that the lymphatic drainage and oncotic pressure are negligible (Jain et al., 2007), the transcapillary exchange of fluid is governed by Starling's law. Using the two laws that govern the transport process in a solid tumor, an explicit formula for the steady state IFP is derived. When expressed in dimensionless form, this formula depends only on the dimensionless tumor radius and a dimensionless parameter

$$\alpha = R\sqrt{\frac{L_p}{K}\frac{S}{V}}, \tag{1.1}$$

where R is the tumor radius (cm), $\frac{S}{V}$ is the vascular surface area per unit volume (cm^{-1}), L_p is the capillary permeability of the microvascular wall (cm second^{-1} mmHg^{-1}), and K is the hydraulic conductivity of the interstitium (cm^2 second^{-1} mmHg^{-1}); all of these parameters are assumed constant.

The model by Baxter and Jain (1989) was extended several years later to include the time-dependent behavior of the IFP in solid tumors (Netti et al., 1995, 1997), by using the Mixture Theory approach (Kenyon, 1976a,b). In these attempts the transient IFP was studied in the following manner: by starting from the elevated steady state IFP value and artificially disturbing this equilibrium by increasing the vascular pressure and then, after the IFP had reached a stable value, a decrease in the vascular pressure caused IFP to return to its initial value. The results of this simulation showed that the IFP near the center of the tumor followed very closely the changes in the microvascular pressure, with a delay of only a few seconds. Intuitively, this behavior is the result of the form of the volumetric flow rate out of the vasculature per unit volume. In the simplest case of negligible lymphatic and oncotic gradients, this flux is given by $\frac{J_v}{V} = \frac{L_p S}{V}(p_v - p)$, where p_v is the blood pressure and p is the IFP, both having the units in mmHg. Since L_p and $\frac{S}{V}$ are taken to be constant, an increase of p_v will increase the flux. Also, since the tumor hydraulic conductivity K is kept constant, the increasing flux will elevate the IFP in order to maintain the equilibrium. Furthermore, the tumor value of the capillary filtration coefficient $L_p\frac{S}{V}$ is very high due to the excess leakiness of the capillary walls; hence, extravasation will be very rapid once the blood pressure is raised.

The conclusions drawn from these mathematical models offered useful insights into the causes of the elevated tumor IFP, but by no means provided a definitive explanation of the

mechanisms responsible for the phenomenon. In particular, the constancy (as well as the actual value) of the tumor hydraulic conductivity K has been questioned. For instance, Khosvarani et al. (2004) found experimentally that the response time of the tumor IFP to a perturbation of the steady state can be substantially different from one tumor to the next, and is strongly influenced by the value of K. A few years later Milosevic et al. (2008) re-analyzed the data using a more refined mathematical model, and estimated the values of K for different tumors.

In Chapter 2, a macroscopic mathematical model is developed to describe the time evolution of a tumor IFP. The attention is placed on the mechanisms which are responsible for the rise of the IFP from its value in healthy interstitium to the measured value in a cancerous state.

As an organ grows, all necessary nutrients are supplied through the creation of new blood vessels (angiogenesis). In healthy tissue angiogenesis is a tightly regulated process, in which the onset and offset mechanisms are controlled by a large number of molecular and mechanical factors (Carmeliet and Jain, 2011; Jain, 2003). The parameter α defined in (1.1) is constant. In contrast, as demonstrated by Gullino (1976), the cells in cancerous tissue acquire the ability to stimulate angiogenesis. Proceeding in an unregulated fashion, angiogenesis gives rise to an abnormal vasculature with blood vessels that are saccular, convoluted, leaky, and have defects in pericyte coverage and function due to the over-expression of the vascular endothelial growth factor (VEGF) signalling protein (Heldin et al., 2004). Thus, as the tumor evolves, the capillary filtration coefficient and the vascular density increase and the parameter α becomes dependent on time.

The Mixture Theory model is further employed to simulate the effect of 'vascular normalization'of the IFP profile. The hypothesis of vascular normalization, proposed by Jain (2001, 2005), postulates that anti-angiogenesis therapy does not just prune vessels, but reverts the abnormal vascular structure and function toward a more normal state, thereby lowering the tumor IFP for a short period of time.

The second application – detailed in Chapter 3 – is more mathematical in nature, and bears relevance to the work in Chapter 2. In the model in Chapter 2, on top of the requirements needed for the Mixture Theory, it is assumed that the pore pressure p and the tissue dilatation e are proportional. As a result, the fundamental partial differential equations of

poroelasticity theory reduce to a standard heat-type equation for the pore pressure in the case of no sources, or to the simplest case of a reaction-diffusion equation when sources are present. This assumption is used in previous models which investigate the behavior of IFP in solid tumors (Netti et al., 1995, 1997), and is clearly of interest to determine how appropriate and accurate it is.

In contrast to the application of poroelasticity theory to solid tumors, this proportionality assumption problem is well known (Bear, 1988), and has been studied in the context of a groundwater flow (Verruijt, 1969). The approximation has been found to be either good or bad, depending on the geometry of the system and the type of boundary conditions prescribed. However, no general test of the approximation has been made. An exception among these studies is De Leeuw (1965), where the necessary and sufficient conditions for the exact proportionality between p and e were identified in the special case of a vertical cylindrical sand drain satisfying the conditions of plane strain and axial symmetry.

Since the paper by De Leeuw (1965) is not readily accessible, Chapter 3 starts with a detailed review of his work. For simplicity, the mathematical model developed there using Mixture Theory assumes no presence of sources and is analyzed, as done by De Leeuw, by using the full system of PDEs under the assumption of spherical symmetry. The results obtained under the assumption of the proportionality of p and e are compared with the results in the case when this assumption is not employed. The difference between the two cases turns out to be substantial. As was mentioned in passing by De Leeuw (1965), it is not clear what the appropriate boundary conditions would be for the non-proportional case.

The third application – reported in Chapter 4 – studies the pathogenesis of normal pressure hydrocephalus. In a normally functioning brain, the cerebral spinal fluid (CSF) is produced in the choroid plexuses—long, convoluted strands of vascular tissue located in the third and lateral ventricles. CSF secretes from the production sites into the third and lateral ventricles and flows through the aqueduct of Sylvius to reach the fourth ventricle. From there, the foramen of Luschka or of Magendie act as pathways through which CSF enters the cranial subarachnoid space. Alternatively, some CSF also penetrates through the lateral ventricle wall and traverses the entire brain parenchyma to arrive at the cranial subarachnoid space. Once in the cranial subarachnoid space, two events can occur—either the CSF circulates within the cranial subarachnoid space to flow into the spinal subarachnoid space and then

back, or CSF reenters the veins through the arachnoid villi which protrude into the venous system (Nolte, 1981; Schurr and Polsky, 1993).

One reason why the brain develops hydrocephalus is due to an obstruction which may block the CSF flow and prevent extrusion of CSF from the lateral ventricles. Consequently, the pressure in the lateral ventricles increases, which forces the ventricular wall to expand and compresses the periventricular brain parenchyma. The mechanism by which the CSF flow impairment occurs is classified into two forms: non-communicating and communicating. In the first form, a blockage either in the aqueduct of Sylvius or the foramina of Luschka prevents CSF from entering the cranial subarachnoid space, and thus, CSF accumulates in the ventricles. A large pressure gradient between the ventricles and the cranial subarachnoid space forms and causes ventricular dilatation. In communicating hydrocephalus, the ventricles and cranial subarachnoid space freely communicate, and hence there is no impediment to the normal CSF flow. However, there is an imbalance between the production and absorption of CSF, but the mechanism that causes the impaired clearance of CSF and the enlargement of ventricles is not fully understood. Paradoxically, as observed mostly in elderly patients, ventricular pressure is frequently measured to be within a normal range. This particular form of communicating hydrocephalus is known as "normal pressure hydrocephalus".

The literature on hydrocephalus is vast, and a review up to the end of the last century is found in Tenti et al. (2000). Recently, Smillie et al. (2005) and Sobey and Wirth (2006) contributed to the research done in this area, including models of normal pressure hydrocephalus, by applying poroelasticity theory and fluid mechanics to a spherical domain and prescribing more sophisticated boundary conditions than used previously. Chapter 4 focuses on the work done by Levine (1999), who has studied extensively the pathogenesis of normal pressure hydrocephalus. Since the brain is very complex in structure, Levine views the brain parenchyma as a radially symmetric spherical shell, as shown in Figure 1.1.

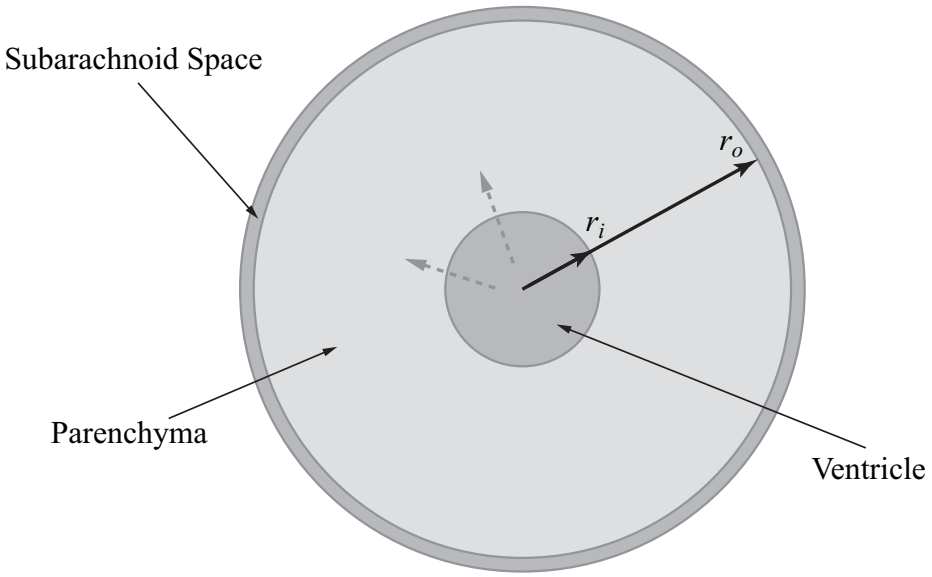

Figure 1.1: Geometry of the brain parenchyma

The central cavity filled with CSF represents the lateral and third ventricles, from which CSF might penetrate through the ventricular wall into the brain parenchyma. The brain subarachnoid space at the outer edge of the parenchyma is considered as a thin CSF-filled shell. Under this description of the parenchyma, Levine investigates three hypotheses: (a) "No Seepage" (NS) hypothesis, which assumes that the ventricular wall is impermeable to CSF; (b) "Seepage, Efficient Parenchymal Absorption" (SEPA) hypothesis, which assumes that CSF seeps from the ventricular space into the brain parenchyma and is efficiently absorbed in the bloodstream; and (c) "Seepage, Inefficient Parenchymal Absorption" (SIPA) hypothesis, which allows for CSF to penetrate the ventricular wall and to enter the brain parenchyma; however, CSF is absorbed inefficiently in the parenchyma, but efficiently in the cranial subarachnoid space.

Levine analyzed the three hypotheses by using the consolidation theory (Biot, 1941), supplemented by a reduced form of Starling's law (Fung, 1990) to account for the absorption of CSF. For each hypothesis, the steady state of the parenchymal interstitial fluid pressure is calculated, as well as the changes in fluid content and the tissue displacement. In the end, the SEPA hypothesis appears to best account for the clinical features found in normal pressure hydrocephalus.

Aspects of Levine's (1999) model do not appear convincing, such as the values and the interpretation of the parameters in his modified version of consolidation theory. Consequently,

in Chapter 4, a Mixture Theory based model is formulated to test the SEPA hypothesis, where the parameter values are consistent with the assumptions of this theory (see Appendix A). The results are substantially different from Levine (1999) and lead to the conclusion that the pathogenesis of normal pressure hydrocephalus is still unknown.

The last chapter is dedicated to an in-depth discussion of the results of all three investigations and stresses the relevance and contribution of this work. Before closing the Thesis, suggestions of possible directions for future work are given.

Appendix A presents the formulation of Mixture Theory, starting from the conservation laws. Appendix B addresses the relation between tissue dilatation and pore pressure. Appendix C provides the analytic solution of the heat type equation under the assumption of proportionality between p and e found in Chapter 3. Lastly, Appendix D shows the detailed calculation of the constants from the general solution in Chapter 3, where the proportionality between p and e is not employed.

Chapter 2

Formulation of the tumor interstitial fluid pressure problem

2.1 Introduction

In this Chapter, a macroscopic mathematical model describing the time evolution of a tumor is formulated. The model is derived by employing a formulation of fluid flow through a porous medium using mixture theory as developed by Kenyon (1976a,b) – to better understand the transient behavior of interstitial fluid pressure (IFP) in solid tumors. The focus of the model is placed on the mechanisms which are responsible for the rise of IFP from a healthy interstitium to a cancerous state. Thus, attention is drawn to a dimensionless parameter α that was first identified by Baxter and Jain (1989), and defined as

$$\alpha = R\sqrt{\frac{L_p}{K}\frac{S}{V}}, \tag{2.1}$$

where R is the solid tumor radius (cm), $\frac{S}{V}$ is the vascular surface area per unit volume (cm^{-1}), L_p is the permeability coefficient of the capillary walls (cm second^{-1} mmHg^{-1}), and K is the hydraulic conductivity of the interstitium (cm^2 second^{-1} mmHg^{-1}). The parameter α involves the values that characterize the fluid movement in a solid tumor, as well as its physical quantities.

In this model, the following interpretation of tumor progression from healthy interstitium to cancerous state is adopted. As an organ grows, the nutrients necessary to keep the organ functioning are normally supplied by newly created blood vessels – a process called angiogenesis. This process is tightly regulated, and the onset and offset mechanisms are controlled by a large number of molecular and mechanical factors (Carmeliet and Jain, 2011; Jain, 2003). For healthy interstitium, the parameter α is kept constant. In contrast, as demonstrated by Gullino (1976), cells in cancerous tissue acquire the ability to initiate angiogenesis. This physiological process is triggered primarily by an over-expression of a signalling protein, called

vascular endothelial growth factor (VEGF), and proceeds in an unregulated fashion, causing an abnormally increased growth of new blood vessels from pre-existing vessels, as well as the deterioration of capillary walls. Angiogenesis eventually leads to a chaotic tumor vasculature – blood vessels that are saccular, convoluted, leaky, and have defects in pericyte coverage and function (Heldin et al., 2004) – within a solid tumor. Furthermore, fluid enters from the deteriorating capillary walls into the tumor interstitium (Carmeliet and Jain, 2011; Goel et al., 2011). Thus, as the tumor evolves, the capillary permeability coefficient L_p and vascular density $\frac{S}{V}$ increase, and the parameter α becomes a function of time.

As outlined in Chapter 1, none of the models that study the evolution of IFP in a solid tumor, including Netti et al. (1995, 1997) through a change in microvascular pressure and Khosvarani et al. (2004) and Milosevic et al. (2008) through a perturbation of the hydraulic conductivity K value, provide an explanation of how the tumor IFP evolves from a value close to that found in a normal interstitium to the abnormally elevated value reached at steady state in a tumor microenvironment. This work presents a mathematical model of tumor IFP evolution where the dimensionless parameter α is a function of time. The time scale begins from the moment angiogenesis is triggered in a cancerous tumor, and ends when the IFP reaches cancerous steady state values.

Later, the mathematical model is used to simulate the effect of 'vascular normalization' on the behavior of tumor IFP. Since 2001, Jain (2001, 2005) sought to establish the hypothesis that anti-angiogenic therapy reverts the chaotic tumor vascular network to a more normal state, thereby lowering tumor IFP. Modeling the administration of anti-angiogenesis therapy allows for a study of its effects on the tumor IFP, under the above understanding of tumor progression.

2.2 Formulation of the mathematical model

In this section, the assumptions and brief overview of mixture theory, on which the mathematical model is based, are discussed. For full details of the theory the reader is referred to either Kenyon (1976b) or to Appendix A of this Thesis.

Mathematical model

A solid tumor is idealized as a mass of soft tissue in the shape of a sphere, which facilitates analytical calculations and allows to focus on the basic underlying mechanisms. Normal tissue parameter values are assumed for a tumor when it is in a precancerous state. After angiogenesis becomes unregulated, the deterioration of the capillary walls and the expansion of the vascular network the parameters reach tumor steady state values. Due to the assumptions needed in order to apply the mixture theory (see Appendix A), the solid tumor is treated as a homogenized medium. At each point the solid and the fluid phases coexist. Individually, the solid phase and the fluid phase are incompressible, and the biphasic material is completely saturated.

Further assumptions are made about the transport process within a solid tumor. The transcapillary exchange of fluid in a homogeneous tissue is assumed to be governed by Starling's law:

$$\Omega(\underline{r},t) = L_p\frac{S}{V}(p_e - p) - L_{pl}\frac{S_l}{V}(p - p_l), \tag{2.2}$$

where L_p and L_{pl} are the hydraulic conductivity of the capillaries and the lymphatics respectively (both with units cm second^{-1} mmHg^{-1}), and $\frac{S}{V}$ and $\frac{S_l}{V}$ are the vascular and the lymphatic surface area per unit tissue volume (both with units cm^{-1}). All pressures are measured in mmHg. The expression $p_e = p_v - \sigma(\pi_c - \pi_i)$ is the effective vascular pressure; p_v and p_l are the vascular and the lymphatic pressures; $p = p(\underline{r},t)$ is the interstitial fluid pressure (IFP)where $\underline{r} = (x,y,z)$ is the location within the tumor (in cm) and t is time (in second). The parameters σ, π_c, and π_i are, respectively, the osmotic reflection coefficient of plasma proteins, the colloid osmotic pressure of plasma and the colloid osmotic pressure of interstitial fluid. It is generally accepted that in a solid tumor, $\pi_c \approx \pi_i$, so that $p_e \approx p_v$ (Jain et al., 2007). Based on the fact that the lymphatic drainage is negligible (Baxter and Jain, 1989) in a solid tumor, equation (2.2) reduces to:

$$\Omega(\underline{r},t) = L_p\frac{S}{V}(p_v - p). \tag{2.3}$$

The motion of the fluid relative to the solid in the interstitium of the tumor is described by a generalized form of Darcy's law (derived in Appendix A, equation (A13)):

$$\phi\left(\underline{v} - \frac{\partial \underline{u}}{\partial t}\right) = -K\nabla p, \tag{2.4}$$

where ϕ is the dimensionless volume fluid fraction being the volume of fluid per unit volume of tissue, $\underline{v}(\underline{r},t)$ is the fluid velocity (with units cm second^{-1}), $\underline{u}(\underline{r},t)$ is the solid displacement vector (in cm), and K is the hydraulic conductivity (with units cm^2 second^{-1} mmHg^{-1}).

Now, the fundamental equations from the classical conservation principles of mechanics are introduced, supplemented by the appropriate constitutive equations. First, the conservation of mass equation for the entire mixture is given by:

$$\frac{\partial e}{\partial t} - K\nabla^2 p = \Omega(\underline{r},t), \tag{2.5}$$

where $e = \nabla \cdot \underline{u}$ is the tissue dilatation defined as the change of volume per unit volume of tissue, and $\Omega(\underline{r},t)$ is the fluid source term given by equation (2.3). (The details of the derivation are found in Appendix A.) Since equation (2.5) is not a closed equation for a single variable, another relation is needed. The next partial differential equation comes from the principle of conservation of linear momentum – i.e., the continuum version of Newton's second law. Since all body forces and inertia forces are neglected, the equation of motion for the entire mixture with the appropriately derived stress tensors for the fluid and the solid components is

$$\mu\nabla^2\underline{u} + (2\mu+\lambda)\nabla(\nabla\cdot\underline{u}) = \nabla p, \tag{2.6}$$

where μ and λ are the Lamé parameters for an elastic solid (with units mmHg). Furthermore, taking the divergence of each term of this equation yields

$$(2\mu+\lambda)\nabla^2 e = \nabla^2 p. \tag{2.7}$$

As a result, equations (2.5) and (2.7) form a closed system in the unknown functions p and e.

One would be tempted, after integrating equation (2.7) to substitute the result into (2.5) without the source term $\Omega(\underline{r},t)$ which leads to

$$\frac{\partial e}{\partial t} - K(2\mu+\lambda)\nabla^2 e = 0. \tag{2.8}$$

The PDE (2.8) represents an equation for the tissue dilatation e. One can impose boundary conditions on e in equation (2.8), but they would not have any physical meaning. Thus, this approach is not useful. However, in Chapter 3, this particular PDE is studied. Given that $e = \nabla\cdot\underline{u}$, equation (2.8) can be written in terms of the solid displacement vector $\underline{u}$ and then, boundary conditions in terms of stress and strain can be imposed. The solution of the PDE

in terms of $\underline{u}$ is employed to find the pressure solutions, and the full details are found in Chapter 3.

One way to obtain a connection between e and p is by rewriting the relation (2.7) as:

$$\nabla^2 \left(p - (2\mu + \lambda)e\right) = 0, \tag{2.9}$$

which is equivalent to

$$\begin{cases} p - (2\mu + \lambda)e = f(x, y, z, t), \\ \nabla^2 f = 0, \end{cases} \tag{2.10}$$

where f is an unknown harmonic function. In the special case when $f(x, y, z, t) \equiv 0$, equation (2.10) gives the relation:

$$(2\mu + \lambda)e = p. \tag{2.11}$$

(The validity of equation (2.11) is discussed in Appendix B.) This approach seems to be the simplest; however, it needs to be justified. In ground water literature, this special case has been studied in depth, and reviewed by Verruijt (1969). In particular, a detailed account of the relation between volume dilatation and pressure is carried out by De Leeuw (1965), using a cylindrical hollow sand drain. Chapter 3 is devoted to testing how good an approximation equation (2.11) is in a spherical geometry, motivated by the work of De Leeuw (1965).

Keeping in mind the special case assumption about the relation between e and p, equation (2.11) is applied to (2.5), and along with (2.3) gives a linear PDE

$$\frac{\partial p}{\partial t} - K(2\mu + \lambda)\nabla^2 p = (2\mu + \lambda)L_p \frac{S}{V}(p_v - p), \tag{2.12}$$

which is a closed equation for the unknown function p. Using spherical coordinates with the origin at the center of the tumor and R being the tumor radius, the assumption of isotropy implies that the IFP is a function of time and radial distance only. The time scale of the model is that obtained by placing the time origin at the moment when the avascular tumor cells start releasing unregulated VEGF, so that the initial condition for the pressure equals the IFP of the surrounding normal tissue value p_i. Thus, in terms of relative IFP,

$$\overline{p} = p - p_i, \tag{2.13}$$

equation (2.12) is given by

$$\frac{\partial \overline{p}}{\partial t} - K(2\mu + \lambda)\left(\frac{2}{r}\frac{\partial \overline{p}}{\partial r} + \frac{\partial^2 \overline{p}}{\partial r^2}\right) = (2\mu + \lambda)L_p \frac{S}{V}(p_v - [\overline{p} + p_i]). \tag{2.14}$$

The boundary conditions for the isolated solid tumor to be imposed on equation (2.14) are similar to Netti et al. (1995, 1997); in particular, zero flux at the tumor center and continuity of the IFP at the periphery:

$$\begin{cases} \frac{\partial \overline{p}(0,t)}{\partial r} = 0, \\ \overline{p}(R,t) = 0, \\ \overline{p}(r,0) = 0. \end{cases} \tag{2.15}$$

A considerable simplification of the problem is produced by a non-dimensionalization procedure. Suitable characteristic length and pressure for the radial distance and the pressure are the radius R and the vascular pressure p_v, but there is no obvious choice for the time scale T (which is determined later). By introducing the new variables for the radius $\hat{r} = \frac{r}{R}$, the time $\hat{t} = \frac{t}{T}$, and the IFP $\hat{p} = \frac{\overline{p}}{p_v}$, into equation (2.14), the choice of T is selected to make the coefficient $K(2\mu + \lambda)$ of the Laplacian equal to 1. Thus, the characteristic time T is calculated to be

$$T = \frac{R^2}{K(2\mu + \lambda)}, \tag{2.16}$$

and the resulting dimensionless PDE for the pressure is

$$\frac{\partial \hat{p}}{\partial \hat{t}} - \frac{2}{\hat{r}}\frac{\partial \hat{p}}{\partial \hat{r}} - \frac{\partial^2 \hat{p}}{\partial \hat{r}^2} + \alpha^2 \hat{p} = \alpha^2(1 - \hat{p}_i). \tag{2.17}$$

The dimensionless parameter,

$$\alpha^2 = R^2 \frac{L_p}{K}\frac{S}{V}, \tag{2.18}$$

plays an important role in this mathematical model.

As outlined in Section 2.1, when angiogenesis becomes unregulated primarily due to the over-expression of the signalling protein VEFG, α^2 becomes dependent on time because either L_p or $\frac{S}{V}$ starts to increase. Two functions are introduced to account for this: first, the time dependence of the permeability of the capillaries is modeled by $L_p(\hat{t})$, while using values for $\frac{S}{V}$ taken from a range reported in the literature (Jain et al., 2007); and second, the time dependence of the surface area per unit volume of the capillary walls is modeled by $\frac{S}{V}(\hat{t})$ with the values of L_p, reflecting the tumor state being either normal or cancerous tissue, taken from literature (Jain et al., 2007). Following the former approach, the formula (2.18) can be written as

$$\alpha^2(\hat{t}) = AL_p(\hat{t}), \tag{2.19}$$

where $A = \frac{R^2}{K}\frac{S}{V}$ is a constant. In the latter case,

$$\alpha^2(\hat{t}) = B\frac{S}{V}(\hat{t}), \tag{2.20}$$

where $B = \frac{R^2 L_p}{K}$ is a constant. Thus, equation (2.17) becomes

$$\frac{\partial \hat{p}}{\partial \hat{t}} - \frac{2}{\hat{r}}\frac{\partial \hat{p}}{\partial \hat{r}} - \frac{\partial^2 \hat{p}}{\partial \hat{r}^2} + \alpha^2(\hat{t})\hat{p} = \alpha^2(\hat{t})(1 - \hat{p}_i), \tag{2.21}$$

where $\alpha^2(\hat{t})$ is given either by equation (2.19) or equation (2.20) with the constraints

$$\begin{cases} \frac{\partial \hat{p}(0,\hat{t})}{\partial \hat{r}} = 0, \\ \hat{p}(1,\hat{t}) = 0, \\ \hat{p}(\hat{r},0) = 0. \end{cases} \tag{2.22}$$

Representation of $\alpha^2(\hat{t})$ by $L_p(\hat{t})$

The origin of the time scale is set at the instant when angiogenesis becomes unregulated in the solid tumor, once the over-expression of VEGF occurs. It is assumed that until then the permeability of the capillary walls is that prevailing in the healthy interstitium; that is, set $L_p(0) \equiv L_p^0 =$ constant. As the time $\hat{t} > 0$ increases, the capillary walls become leakier, leading to an increase in the permeability; however, this process does not go on indefinitely, but reaches a plateau, after which L_p takes on the value typical of a fully developed tumor as measured experimentally, which is denoted as L_p^∞. Thus, a simple model reproducing this behavior is given by

$$\alpha^2(\hat{t}) = \alpha_0^2\left[1 + \hat{C}\left(1 - e^{-\hat{D}\hat{t}}\right)\right], \tag{2.23}$$

where $\alpha_0^2 = R^2\frac{L_p^0}{K}\frac{S}{V}$ is a constant based on the values for the normal tissue and $\hat{C}, \hat{D} > 0$ are constants. Even more compactly,

$$L_p(\hat{t}) = L_p^0\left[1 + \hat{C}\left(1 - e^{-\hat{D}\hat{t}}\right)\right], \tag{2.24}$$

where the parameter $\hat{C}$, since it has no dimension, is given by

$$\hat{C} = \frac{L_p^\infty}{L_p^0} - 1. \tag{2.25}$$

The constant D is non-dimensionalized by the same time scale T (2.16); that is,

$$\hat{D} = DT = D\frac{R^2}{K(2\mu + \lambda)}. \tag{2.26}$$

Representation of $\alpha^2(\hat{t})$ *by* $\frac{S}{V}(\hat{t})$

A suitable representation of $\alpha^2(\hat{t})$ using $\frac{S}{V}(\hat{t})$ is similar in nature to the previous case. Once the unregulated angiogenesis process begins with the over-expression of VEGF released to promote abnormally increased growth of new blood vessels from pre-existing blood vessels, at time $\hat{t} = 0$, $\frac{S}{V}$ gradually increases until it plateaus, and $\alpha^2(\hat{t})$ takes on the exponential form

$$\alpha^2(\hat{t}) = \alpha_0^2 \left[1 + \hat{E}\left(1 - e^{-\hat{F}\hat{t}}\right)\right], \tag{2.27}$$

where $\alpha_0^2 = R^2 \frac{L_p^0}{K} \frac{S}{V}^0$ is a constant related to the normal tissue, $\frac{S}{V}^0$ is the initial surface area per unit volume of capillaries, and $\hat{E}, \hat{F} > 0$ are constants.

Proceeding by analogy with the previous case, it follows that

$$\frac{S}{V}(\hat{t}) = \frac{S}{V}^0 \left[1 + \hat{E}\left(1 - e^{-\hat{F}\hat{t}}\right)\right], \tag{2.28}$$

where the parameter $\hat{E}$ is dimensionless, and given by

$$\hat{E} = \frac{L_p^\infty \frac{S}{V}^\infty}{L_p^0 \frac{S}{V}^0} - 1, \tag{2.29}$$

with $\frac{S}{V}^\infty$ being the higher surface area per unit volume of the capillaries when the tumor is fully developed. The parameter $\hat{F}$ is non-dimensionalized exactly as $\hat{D}$ of the preceding model.

2.3 Solution

The objective of this Section is to show how the steady state and transient solutions are obtained.

2.3.1 Steady state

The steady state equation is obtained by setting $\frac{\partial \hat{p}}{\partial t} = 0$ in equation (2.21) and using the limit as $\hat{t} \to \infty$ such that the capillary wall parameters become $L_p(\hat{t}) \to L_p^\infty$ (or $\frac{S}{V}(\hat{t}) \to \frac{S}{V}^\infty$). Then, the steady state equation for the dimensionless pressure becomes

$$-\frac{2}{\hat{r}}\frac{d\hat{p}}{d\hat{r}} - \frac{d^2\hat{p}}{d\hat{r}^2} + \alpha_\infty^2 \hat{p} = \alpha_\infty^2 (1 - \hat{p}_i), \tag{2.30}$$

where

$$\alpha_\infty^2 = R^2 \frac{L_p^\infty}{K} \frac{S}{V}. \tag{2.31}$$

To eliminate the first term in equation (2.30). Define $w(\hat{r}) = \hat{r}\hat{p}(\hat{r})$ to obtain

$$\frac{d^2 w}{d\hat{r}^2} - \alpha_\infty^2 w = -\hat{r}\alpha_\infty^2 (1 - \hat{p}_i). \tag{2.32}$$

Equation (2.32) is subjected to the boundary conditions

$$\begin{cases} w(0) = 0, \\ \\ w(1) = 0. \end{cases} \tag{2.33}$$

The general solution of equation (2.32) is

$$w(\hat{r}) = c_1 e^{-\alpha_\infty \hat{r}} + c_2 e^{\alpha_\infty \hat{r}} + \hat{r}(1 - \hat{p}_i), \tag{2.34}$$

where the constants c_1 and c_2 are determined from equation (2.33). After simplifying,

$$w(\hat{r}) = (1 - \hat{p}_i) \left(1 - \frac{\sinh(\alpha_\infty \hat{r})}{\sinh(\alpha_\infty)} \right). \tag{2.35}$$

Changing back to $\hat{p}$, the steady state solution is

$$\hat{p}(\hat{r}) = \frac{p - p_i}{p_v - p_i} = (1 - \hat{p}_i) \left(1 - \frac{1}{\hat{r}} \frac{\sinh(\alpha_\infty \hat{r})}{\sinh(\alpha_\infty)} \right), \tag{2.36}$$

which has the same behavior as identified by Baxter and Jain (1989).

2.3.2 Transient state

Here, the derivation of the analytic solution is discussed in detail. As well, an outline of the numeric approach is presented.

Analytic solution

Equation (2.21) is a nonhomogeneous linear partial differential equation which is now investigated with homogenous boundary conditions (2.22). This boundary value problem can be solved by the method of eigenfunction expansion. To further simplify the boundary value problem, define $z(\hat{r}, \hat{t}) = \hat{r}\hat{p}(\hat{r}, \hat{t})$ so that the second term on the left hand side in equation (2.21) is eliminated:

$$\frac{\partial z}{\partial \hat{t}} - \frac{\partial^2 z}{\partial \hat{r}^2} + \alpha^2(\hat{t}) z = \hat{r}\alpha^2(\hat{t})(1 - \hat{p}_i), \tag{2.37}$$

and

$$\begin{cases} z(0,\hat{t}) = 0, \\ z(1,\hat{t}) = 0, \\ z(\hat{r},0) = 0. \end{cases} \tag{2.38}$$

The method of eigenfunction expansion, employed to solve the nonhomogeneous problem of equation (2.37) with the homogeneous boundary conditions (2.38), consists of expanding the unknown solution $z(\hat{r},\hat{t})$ as a series of related eigenfunctions:

$$z(\hat{r},\hat{t}) = \sum_{n=1}^{\infty} b_n(\hat{t})\phi_n(\hat{r}), \tag{2.39}$$

where $b_n(\hat{t})$ is a function of time. Equation (2.39) is obtained using the standard separation of variables technique. The solutions are given by the eigenfunctions $\phi_n(\hat{r}) = \sin(n\pi\hat{r})$ with eigenvalues $\lambda_n = n^2\pi^2$, for $n = 1, 2, 3, ...$ Furthermore, the initial condition on z implies that

$$z(\hat{r},0) = \sum_{n=1}^{\infty} b_n(0)\phi_n(n\pi\hat{r}) = 0, \tag{2.40}$$

for an arbitrary $\hat{r}$; hence, $b_n(0) = 0$.

Proceeding with the term-by-term differentiation of $z(\hat{r},\hat{t})$,

$$\begin{aligned} \frac{\partial z}{\partial \hat{t}} &= \sum_{n=1}^{\infty} \frac{db_n(\hat{t})}{d\hat{t}} \sin(n\pi\hat{r}) \\ \frac{\partial^2 z}{\partial \hat{r}^2} &= \sum_{n=1}^{\infty} -b_n(\hat{t})(n\pi)^2 \sin(n\pi\hat{r}). \end{aligned} \tag{2.41}$$

and substituting the above results into equation (2.39) yields

$$\sum_{n=1}^{\infty} [b_n'(\hat{t}) + b_n(\hat{t})(\alpha^2(\hat{t}) + (n\pi)^2)] \sin(n\pi\hat{r}) = \hat{r}\alpha^2(\hat{t})(1-\hat{p}_i). \tag{2.42}$$

Using the orthogonality of $\phi_n(\hat{r})$, an ordinary differential equation for $b_n(\hat{t})$ is obtained:

$$b_n'(\hat{t}) + b_n(\hat{t})(\alpha^2(\hat{t}) + (n\pi)^2) = \frac{\int_0^1 \hat{r}\alpha^2(\hat{t})(1-\hat{p}_i)\sin(n\pi\hat{r})d\hat{r}}{\int_0^1 \sin^2(n\pi\hat{r})d\hat{r}} \equiv \overline{q}_n(\hat{t}), \tag{2.43}$$

where

$$\overline{q}_n(\hat{t}) = 2\alpha^2(\hat{t})(1-\hat{p}_i)\frac{(-1)^{n+1}}{(n\pi)}. \tag{2.44}$$

The integrating factor

$$I(\hat{t}) = \exp\left(\int_0^{\hat{t}} (\alpha^2(\hat{t}') + (n\pi)^2)d\hat{t}'\right) = \exp\left(\int_0^{\hat{t}} \alpha^2(\hat{t}')d\hat{t}' + (n\pi)^2\hat{t}\right), \tag{2.45}$$

applied to equation (2.43) produces

$$b_n(\hat{t}) = 2(1-\hat{p}_i)\frac{(-1)^{n+1}}{(n\pi)}\ I(\hat{t})^{-1}\int_0^{\hat{t}}\left(I(\hat{t})\ \alpha^2(\hat{t}')\right)d\hat{t}', \tag{2.46}$$

remembering that $b_n(0) = 0$. Thus, the final solution to the nonhomogeneous PDE (2.21) with boundary conditions (2.22), after the variable has been changed back to $\hat{p}$, is

$$\hat{p}(\hat{r},\hat{t}) = 2\frac{(1-\hat{p}_i)}{\hat{r}}\sum_{n=1}^{\infty}\frac{(-1)^{n+1}\sin(n\pi\hat{r})}{n\pi}\ I(\hat{t})^{-1}\int_0^{\hat{t}}\left(I(\hat{t})\ \alpha^2(\hat{t}')\right)d\hat{t}'. \tag{2.47}$$

The last part consists of using a particular form for $\alpha^2(\hat{t})$ given by (2.23):

$$\hat{p}(\hat{r},\hat{t}) = 2\frac{(1-\hat{p}_i)}{\hat{r}}\sum_{n=1}^{\infty}\frac{(-1)^{n+1}\sin(n\pi\hat{r})}{n\pi}\ \hat{\beta}^{-1}(\hat{t})\int_0^{\hat{t}}\left(\hat{\beta}(\hat{t})\ \alpha_0^2\left[1+\hat{C}(1-e^{-\hat{D}\hat{t}'})\right]\right)d\hat{t}', \tag{2.48}$$

where

$$\hat{\beta}(\hat{t}) = \exp\left(\left[\alpha_0^2(1+\hat{C})+(n\pi)^2\right]\hat{t}+\frac{\alpha_0^2\hat{C}}{\hat{D}}(e^{-\hat{D}\hat{t}}-1)\right). \tag{2.49}$$

A major difficulty in proceeding further lies with the the term $\exp\left(\frac{\alpha_0^2\hat{C}}{\hat{D}}(e^{-\hat{D}\hat{t}'}-1)\right)$ in the integrand of equation (2.48), which makes it impossible to find a simple primitive. Using the linear approximation to $e^{-\hat{D}\hat{t}}$ in the integrand only works for small time intervals, over which the solution does not reach its growth plateau. To avoid the difficulty, Simpson's rule for numerical integration is used to solve equation (2.48) algebraically.

A time dependent solution similar to equation (2.48) is obtained in the case where $\alpha^2(\hat{t})$ is modeled by $\frac{S}{V}(\hat{t})$ as defined in equation (2.27).

Numerical solution

The PDE (2.21) with boundary conditions (2.22) is also solved numerically in MATLAB using a finite difference method (in particular the forward in time and centered in space numeric scheme). The numerical solution matched the analytical solution.

2.4 Parameters

In order for the mathematical model of tumor interstitial fluid pressure (IFP) to have predictive capabilities, the parameter values are now discussed and selected. Most of the parameter values used in the mathematical model have been measured directly; however, some were calculated.

Table 2.1 shows the values needed for the representation of $\alpha^2(t)$. Since no major tumor growth is assumed, the radius of the solid tumor is fixed. Also, the hydraulic conductivity K is assumed constant, meaning that the ease with which fluid passes through the tumor interstitium does not change even though more fluid enters the tumor interstitium.

Parameter	Value	Reference
R	0.4 cm	Jain et al. (2007)
K	2.5×10^{-7} cm^2 second^{-1} mmHg^{-1}	Jain et al. (2007)
$\frac{S}{V}$	$50-250$ cm^{-1}	Jain et al. (2007)
L_p^0 (normal tissue) L_p^∞ (tumor)	3.6×10^{-8} cm second^{-1} mmHg^{-1} 1.9×10^{-6} cm second^{-1} mmHg^{-1}	Jain et al. (2007) Jain et al. (2007)
α_0 (normal tissue) α_∞ (tumor)	1.1–2.4 7.7–17.3	Jain et al. (2007) Jain et al. (2007)
p_i	(-3) – (3) mmHg	Lunt et al. (2008)
p_v	$15-25$ mmHg	Lunt et al. (2008)

Table 2.1: Model parameter values

The vascular density $\frac{S}{V}$ in Jain et al. (2007) is given to be $50 - 250$ cm^{-1} for both the normal tissue and the tumor. It is not clear what the vascular density should be for either state, and thus, the choice of $\frac{S}{V}$ is discussed later for each model. However, to calculate the value of α_0 or α_∞ by taking the square root of equation (2.18), all parameter values are fixed, except the value for $\frac{S}{V}$, which varies - i.e. under the normal tissue state using L_p^0, when $\frac{S}{V}$ is 50 cm^{-1}, α_0 is the lower extreme of 1.1, and when $\frac{S}{V}$ is 250 cm^{-1}, α_0 is the higher extreme of 2.4. The same can be seen for α_∞. Furthermore, the surrounding tissue pressure p_i ranges between -3 and 3 mmHg, and the value used in the model is the average, 0 mmHg. Lastly, the value of the vascular pressure p_v is cited to be in the range $15 - 25$ mmHg; in this study, an average of 20 mmHg is used.

It is a very challenging task to select parameter values to capture the essence of the phenomenon under investigation. In Table 2.1, none of the parameter values have an error bar, which means that the uncertainties in the parameter values may be considerable.

Scaling parameter T

When graphing the behavior of $\alpha^2(\hat{t})$, the time interval for dimensionless time $\hat{t}$ needs to be addressed. Normally, $\hat{t}$ runs from 0 to 1. In Section 2.2,

$$T = \frac{R^2}{K(2\mu + \lambda)} \tag{2.50}$$

was defined as the characteristic time scale to make the time t dimensionless. However, the time interval from 0 to 1 is not the one over which $\alpha^2(\hat{t})$ or the IFP reach their steady state plateau. Such a choice is not appropriate for the following reason. The relevant characteristic time scale must cover the time interval between the release of the unregulated VEGF and the establishment of the steady state. Assuming that $R = 0.4$ cm and $K = 2.5 \times 10^{-7}$ cm^2 second^{-1} mmHg^{-1} are kept constant as suggested by Jain at al. (2007), the value of the parameter T depends crucially on the value of the Lamé coefficients μ and λ, as seen in Table 2.2.

Material	λ (mmHg)	μ (mmHg)	T (second)	Reference
Biological tissue	684	15.2	896	Netti et al. (1995, 1997)
Very soft clay	3.0×10^4	7.5×10^3	14.2	Bowles (1988)
Saturated soft clay	1.5×10^5	3.6×10^4	2.9	Bowles (1988)
Rubber	3.0×10^8	2.0×10^8	9.1×10^{-4}	Bowles (1988)

Table 2.2: Parameter T values for various elastic materials

The fourth column of this table shows that if T were the appropriate time scale then the IFP would reach the steady state in no more than 15 minutes. In other words, the effect of the unregulated VEGF would increase the hydraulic permeability of the vascular walls from $L_p^0 = 3.6 \times 10^{-8}$ to $L_p^\infty = 1.86 \times 10^{-6}$ (cm^2 second^{-1} mmHg^{-1}) in less than 15 minutes, which contradicts the experimental findings of it lasting days – rather than minutes or seconds – as obtained by several groups (Bates and Curry, 1996; Chang et al., 2000; Pocock et al., 2003).

Frequency parameter

The model allows one to determine an appropriate time scale in the following way by using the frequency parameter. Consider the case where the time evolution of the IFP is regulated by the time evolution of $\alpha^2(\hat{t})$ defined in terms of $L_p(\hat{t})$. From equation (2.24),

the steady state is reached when $e^{-\hat{D}\hat{t}} << 1$. However, because of equation (2.26), $\hat{D}\hat{t}$ is the same as Dt, which means that the scaling parameter T does not influence the time scale. Thus, for instance, an approximate value of the true time scale t_* accurate to less than 1% can be obtained by taking $Dt_* \approx 5$, where the frequency of D is estimated from experimental measurements. The same conclusion is reached in the case where $\alpha^2(\hat{t})$ is modeled using $\frac{S}{V}$ with the frequency parameter F.

In essence, the frequency parameter governs the time scale for the behavior of $\alpha^2(\hat{t})$ and hence the IFP to reach its steady state. The time needed to reach steady state depends on the rate at which the tumor grows (either being a fast growing tumor or a slow growing tumor), as discussed next. Thus, the model shows that the time scale depends on the type of tumor growth rather than on the changing parameters that comprise α or the scaling parameter T.

Parameter D

The value of the parameter that governs exponential growth varies depending on the rate of solid tumor growth and on the way $\alpha^2(\hat{t})$ is modeled. In the case where $\alpha^2(\hat{t})$ is modeled by $L_p(\hat{t})$, the value for D is chosen from an in-vivo experiment performed on mice where the permeability of capillaries within a solid tumor was measured after exposure to VEGF - an over-expressed protein that triggers angiogenesis. Bates and Curry (1996) show that during the initial exposure to VEGF it only takes approximately 30 seconds for a rapid increase in L_p to occur, and within 24 hours, L_p is fivefold greater than its original value. For a slow growing tumor, a 3 day interval was selected to observe the effect on the model. With these time intervals, a possible value of D is selected (see Table 2.3), which defines the asymptotic time t_* for the steady-state to be achieved.

Tumor rate of growth	Frequency D_i (i = 1,2,3)	Time scale t_*^i (i = 1,2,3)
Fast	$D_1 = \frac{1}{30}$ second^{-1}	$t_*^1 \approx 150$ second
Intermediate	$D_2 = 1$ day^{-1}	$t_*^2 \approx 5$ days
Slow	$D_3 = \frac{1}{3}$ day^{-1}	$t_*^3 \approx 15$ days

Table 2.3: Parameter values for frequency D and time scale t_*

Parameter F

In the case of modeling $\alpha^2(\hat{t})$ by $\frac{S}{V}(\hat{t})$, the possible values of F are selected from the work by Algire and Chalkley (1945). Algire and Chalkley were interested in examining the spatial and temporal distributions of vascular morphology of tumors and used mice with a transplanted human tumor as their experimental model. In their work, it has been observed that a fast growing tumor, such as a sarcoma, begins to sprout new capillaries from the pre-existing blood vessels within $2-3$ days and the vascular space increases $40-50$ percent within $5-8$ days. However, a slow growing tumor such as a melanoma took at least 8 days before any sprouting occurred and the vascular space never exceeded 25 percent during the entire observation period. A sample of values of F is provided in Table 2.4 to calculate the time scale t_{**} for the steady state to be reached.

Rate of tumor growth		Frequency F_i $(i=1,2,3,4)$	Time scale t^i_{**}
Rapid growing tumor			
Sprouting	2-3 days	$F_1 = \frac{1}{3}$ day^{-1}	$t^1_{**} \approx 14$ days
Increased $\frac{S}{V}$	5-8 days	$F_2 = \frac{1}{7}$ day^{-1}	$t^2_{**} \approx 33$ days
Slow growing tumor			
Sprouting	8 days	$F_3 = \frac{1}{8}$ day^{-1}	$t^3_{**} \approx 38$ days
Increased $\frac{S}{V}$	16 days*	$F_4 = \frac{1}{16}$ day^{-1}	$t^4_{**} \approx 77$ days

Table 2.4: Parameter values for frequency F and time scale t_{**}

In Table 2.4, for a slow growing solid tumor, the frequency $F_4 = \frac{1}{16}$ day^{-1} was estimated in the case of the increased vascular density. The estimate was based on the fact that for a rapidly growing solid tumor it takes approximately double the amount of time for the initial formation of new blood vessels. This was merely done to give a qualitative sample for the value of t_{**} needed so that $\alpha^2(t)$ reaches its steady state.

2.5 Results

From the proceeding sections, it is evident that the formulation of the mathematical model through mixture theory allows the study of the effect of $\alpha^2(t)$ or $\alpha(t)$, as well the resulting interstitial fluid pressure (IFP) distribution, both as functions of time, with time measured in seconds or days.

2.5.1 Steady state

The dimensionful form of equation (2.36), by substituting for the dimensionless variables $\hat{p} = \frac{\overline{p}}{p_v}$ and $\hat{r} = \frac{r}{R}$ and then the relative pressure $\overline{p} = p - p_i$, is given by

$$p(r) = p_v \left(1 - \frac{R}{r}\frac{\sinh(\alpha_\infty \frac{r}{R})}{\sinh(\alpha_\infty)}\right) + p_i. \tag{2.51}$$

This equation is used to study the steady-state IFP profile.

According to steady state IFP equation (2.51), the IFP profile is governed by the the dimensionless parameter α_∞. Figure 2.1 shows a sample of the behavior of IFP depending on α_∞, which is consistent with the literature (Baxter and Jain, 1989). However, the interpretation of the parameter α_∞ is different. In the model this parameter is fixed by the asymptotic value $L_p^\infty \frac{S}{V}$ of the capillary's filtration coefficient, where $\frac{S}{V}$ varies from $50 - 250$ cm^{-1} to give different α_∞ values; on the other hand, Baxter and Jain (1989) consider α_∞ as a variable parameter.

As the value of α_∞ increases, IFP increases throughout the tumor and rapidly drops near the periphery. When the value of α_∞ decreases beyond the values shown in Figure 2.1, the IFP gets closer to zero more quickly.

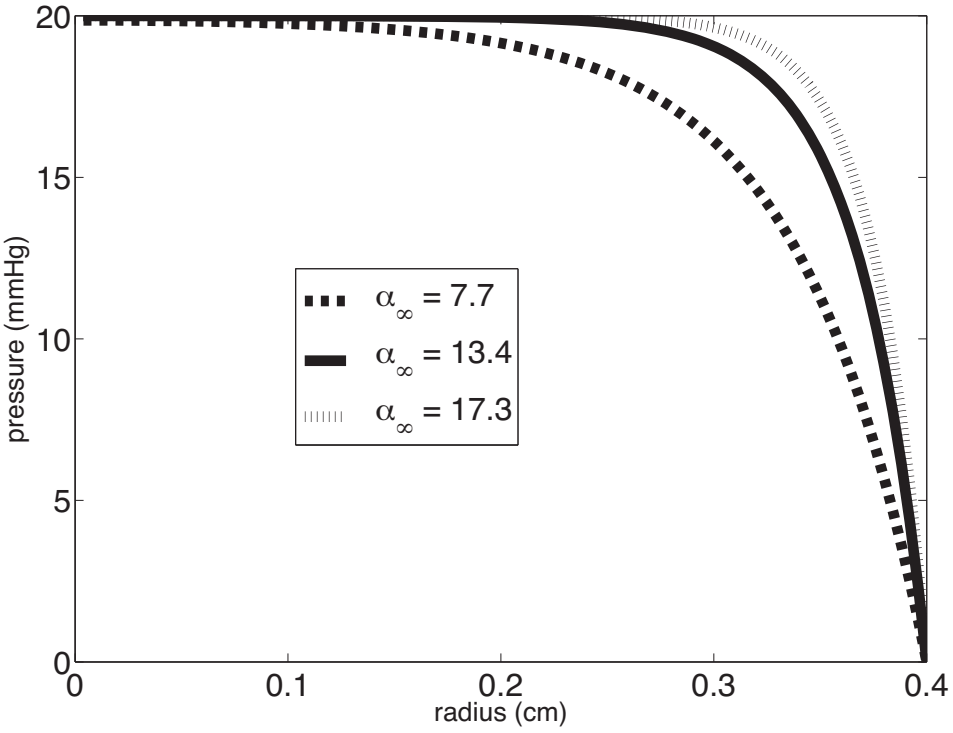

Figure 2.1: IFP steady state profile

2.5.2 Transient state

The main result of the mathematical model comes from the transient solution. The transient results show how the IFP within a solid tumor increases in time as the capillary walls become 'leakier' (modeled by $L_p(t)$) or as the surface area per unit volume of the vasculature increases (modeled by $\frac{S}{V}(t)$).

In analyzing the evolution of IFP with $L_p(t)$ and with $\frac{S}{V}(t)$, the full dimensional form of the solution is considered. One location within a solid tumor is selected: $r = 0.2$ cm, about halfway between the center and the periphery of a solid tumor. This particular location is chosen because, as Figure 2.1 shows, near the center and the edge of a solid tumor, the IFP is strongly influenced by the boundary conditions. It would be of interest to observe the IFP changes occurring in the middle of a solid tumor, in order to gauge the effectiveness of therapeutic agents, since it is known that the uptake is more efficient in lower IFP regions near the edge and stands no chance of reaching the center (Goel et al., 2011).

Time-scale considerations are crucial to the analysis of the transient state. Both the analytical and fully numerical solutions of the boundary value problem (2.21) with boundary conditions (2.22) modeled by either $L_p(t)$ or $\frac{S}{V}(t)$ require the use of the dimensionless time $\hat{t} = \frac{t}{T}$, where T is given by equation (2.16). Thus, the elastic constants λ and μ must be selected consistent with the assumptions stated in Section 2.4. This implies that the viscoelasticity of the solid matrix should be negligible, which cannot happen if the elastic parameters come from the biological tissue as in Netti et al. (1995, 1997). Thus, the values measured in saturated soft clay listed in Table 2.2 are employed as a realistic representation of the actual system. The results of the simulations for the various frequency parameters are presented for the behavior of $\alpha(t)$ and IFP with the time scales plotted in real time. Thus, the model predicts that the rise of the tumor IFP to an equilibrium value very close to the vascular pressure is the same for different types of tumors, but occurs on different time scales.

Evolution of $\alpha(t)$ modeled by $L_p(t)$

The transient behavior of $\alpha(t)$ modeled by $L_p(t)$ is simulated using equation (2.23) in full dimensional form,

$$\alpha(t) = \alpha_0 \sqrt{1 + C\,(1 - e^{-Dt})}, \tag{2.52}$$

where t is in either seconds or days. The parameters that are fixed are: the tumor radius $R = 0.4$ cm, the vascular network density $\frac{S}{V} = 150$ cm^{-1}, being a nominal value of the range provided in Table 2.1, and the hydraulic conductivity $K = 2.5 \times 10^{-7}$ cm^2 second^{-1} mmHg^{-1}. However, the capillary permeability coefficient L_p increases from the normal tissue value $L_p^0 = 3.6 \times 10^{-8}$ cm^2 second^{-1} mmHg^{-1} to the tumor value $L_p^\infty = 1.9 \times 10^{-6}$ cm^2 second^{-1} mmHg^{-1}. Thus, the value for C is calculated by equation (2.25) to be 50.7.

Figure 2.2, Figure 2.3 and Figure 2.4 show the effect of the frequency D from Table 2.3 on $\alpha(t)$. In all cases, $\alpha(t)$ start with the normal tissue value of $\alpha_0 = 1.1$ and gradually reaches the tumor value of $\alpha_\infty = 7.7$. The only difference between the three graphs is the time needed to reach steady state. Figure 2.2, with $D_1 = \frac{1}{30}$ second^{-1}, shows that α reaches the carrying capacity within seconds; however, Figure 2.3 and Figure 2.4, with $D_2 = 1$ day^{-1} and $D_1 = \frac{1}{3}$ day^{-1} respectively, show that steady state occurs within several days.

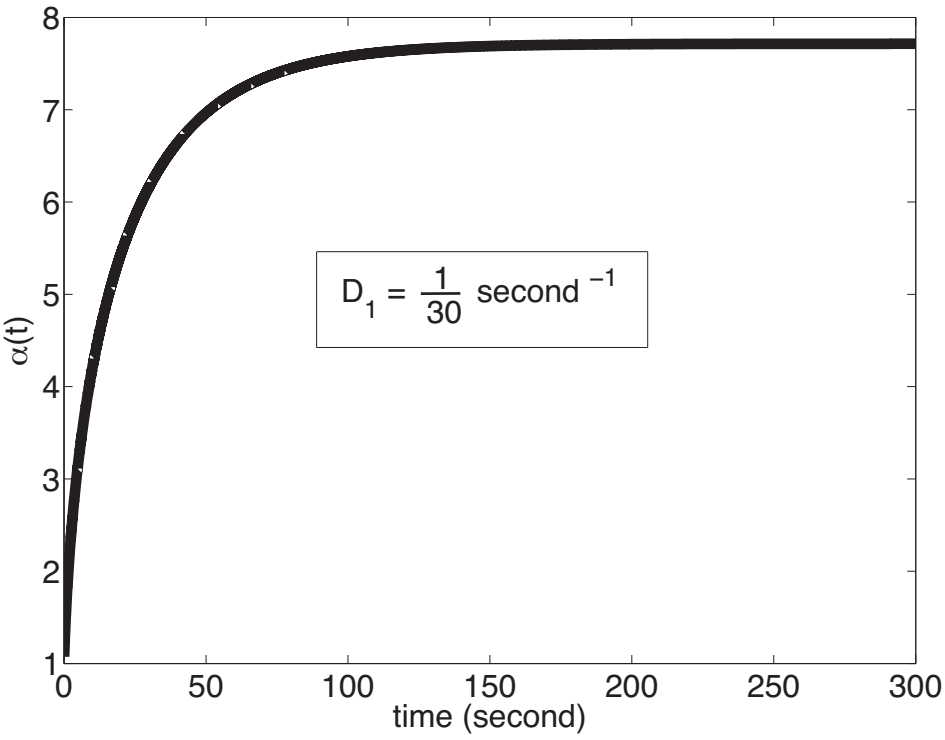

Figure 2.2: Behavior of $\alpha(t)$ modeled by $L_p(t)$ with $D_1 = \frac{1}{30}$ second^{-1}

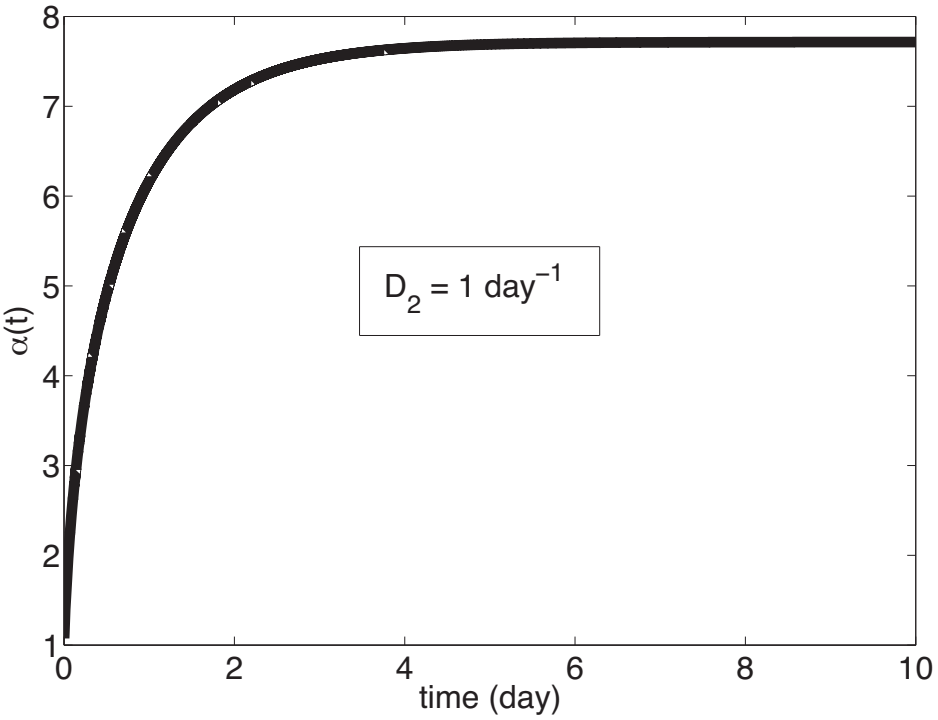

Figure 2.3: Behavior of $\alpha(t)$ modeled by $L_p(t)$ with $D_2 = 1$ day^{-1}

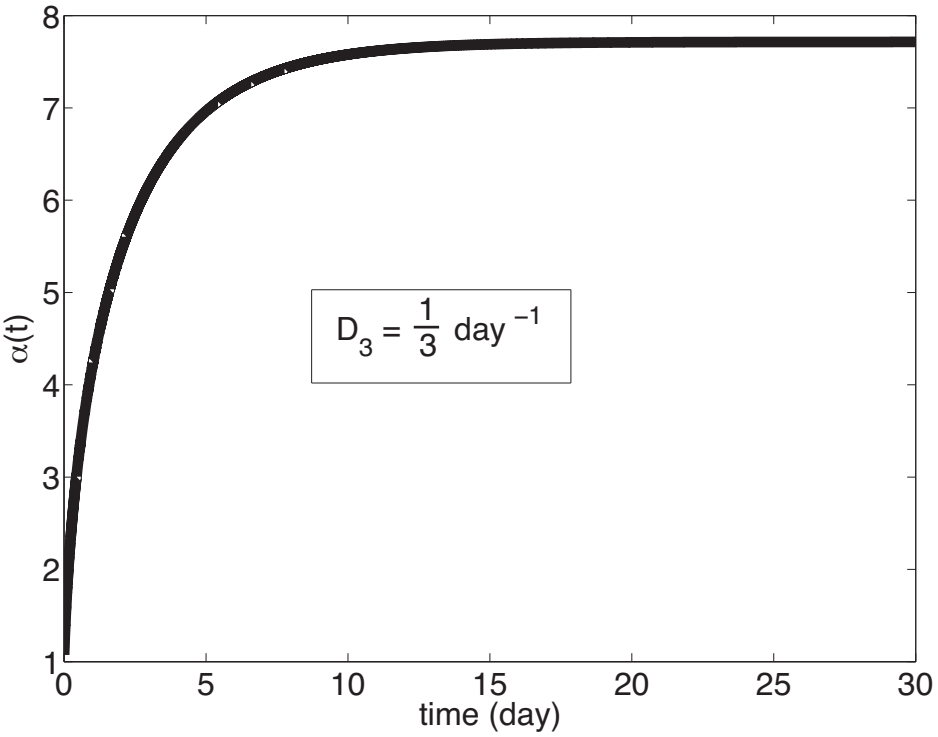

Figure 2.4: Behavior of $\alpha(t)$ modeled by $L_p(t)$ with $D_3 = \frac{1}{3}$ day^{-1}

Evolution of IFP modeled by $L_p(t)$

The analytic IFP transient solution in full dimensional form is

$$p(r,t) = \frac{2\,p_v\,r}{R} \sum_{n=1}^{\infty} \frac{(-1)^{n+1}\sin(n\pi\frac{r}{R})}{n\pi}\,\beta(t)^{-1}\int_0^{\frac{t}{T}} \Big(\beta(t)\,\alpha^2(t')\Big)\,dt' + p_i, \tag{2.53}$$

where

$$\beta(t) = \exp\left(\Big[\alpha_0^2(1+C) + (n\pi)^2\Big]\,\frac{t}{T} + \frac{\alpha_0^2 C}{DT}(e^{-Dt}-1)\right). \tag{2.54}$$

The behavior of $\alpha(t)$ impacts the evolution of IFP within a solid tumor in this model as seen in Figure 2.5, Figure 2.6 and Figure 2.7. As time elapses, the IFP increases, which is regulated by $\alpha(t)$ – in particular, by the frequency D – and reaches the tumor steady state IFP value.

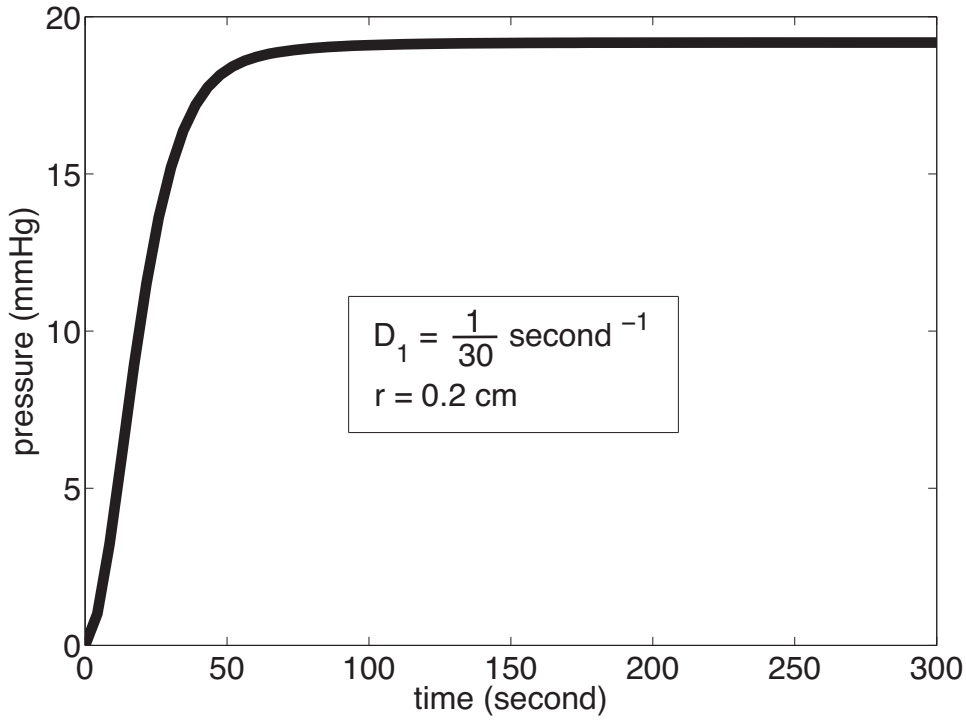

Figure 2.5: Transient IFP profile modeled by $L_p(t)$ with $D_1 = \frac{1}{30}$ second^{-1}

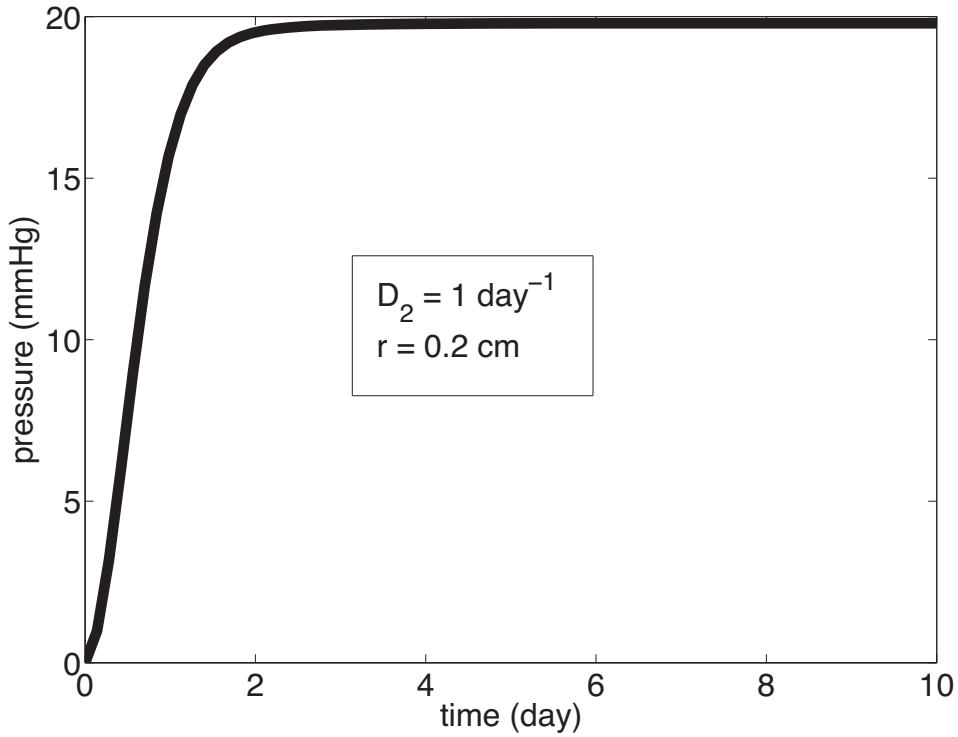

Figure 2.6: Transient IFP profile modeled by $L_p(t)$ with $D_2 = 1$ day^{-1}

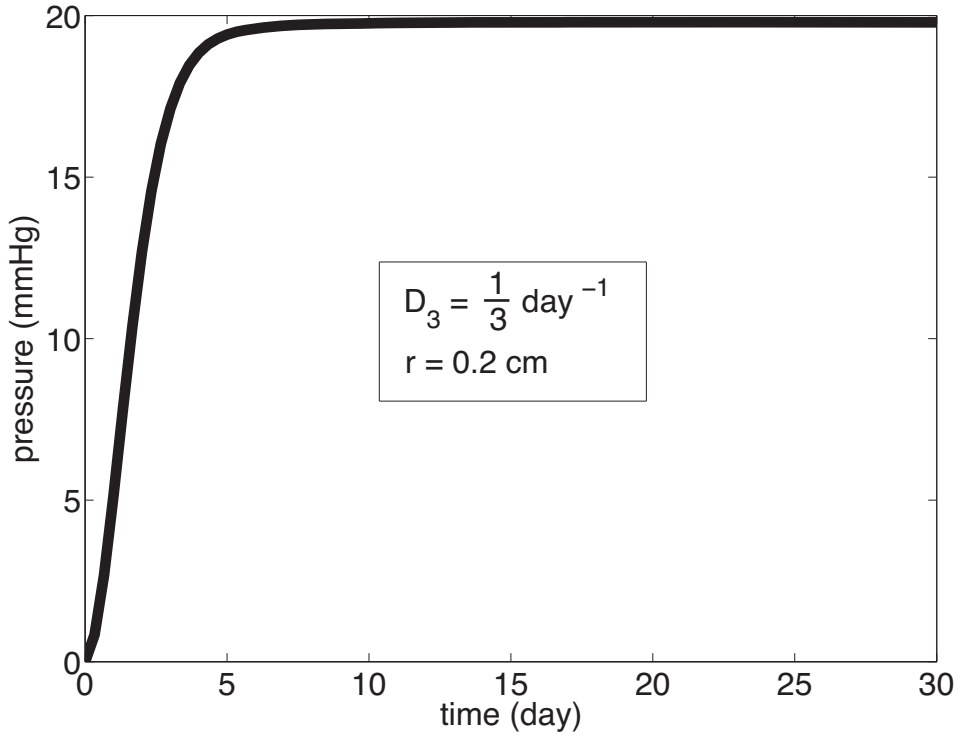

Figure 2.7: Transient IFP profile modeled by $L_p(t)$ with $D_3 = \frac{1}{3}$ day^{-1}

Evolution of $\alpha(t)$ modeled by $\frac{S}{V}(t)$

The transient behavior of $\alpha(t)$ modeled by $\frac{S}{V}(t)$ is simulated using equation (2.27),

$$\alpha(t) = \alpha_0\sqrt{1 + E\,(1 - e^{-Ft})}, \tag{2.55}$$

where t is in days. As in the previous case with $L_p(t)$, the hydraulic conductivity $K = 2.5 \times 10^{-7}$ cm^2 second^{-1} mmHg^{-1} is kept constant. The capillary permeability coefficient L_p increases from the normal tissue value $L_p^0 = 3.6 \times 10^{-8}$ cm second^{-1} mmHg^{-1} to the tumor value $L_p^\infty = 1.9 \times 10^{-6}$ cm second^{-1} mmHg^{-1}. However, since the vascular density is of interest, two cases are considered. Given that the range of $\frac{S}{V}$, is the same for both normal tissue and a solid tumor, $50 - 250$ cm^{-1}, the normal tissue value $\frac{S}{V}^0$ is fixed at 50 cm^{-1}, the lower extreme. For the tumor value, two $\frac{S}{V}$ possibilities are considered: when $\frac{S}{V}^\infty$ assumes 150 cm^{-1}, the average of the range, or 250 cm^{-1}, which is the higher extreme. Thus, the parameter E is calculated from equation (2.29) to be either 154.0 or 257.3, depending on the tumor value for $\frac{S}{V}$, as shown in Table 2.5. Lastly, the frequency F represents the increase in the vascular network. The two values examined are for $\frac{S}{V}$ increased when the tumor growth is rapid, $F_2 = \frac{1}{7}$ day^{-1}, and when the tumor growth is slow, $F_4 = \frac{1}{16}$ day^{-1}, as per Table 2.4.

Case	Normal tissue	Tumor	E equation (2.89)
1	$\frac{S}{V}^0 = 50$ cm^{-1}	$\frac{S}{V}^\infty = 150$ cm^{-1}	154.0
2	$\frac{S}{V}^0 = 50$ cm^{-1}	$\frac{S}{V}^\infty = 250$ cm^{-1}	257.3

Table 2.5: Values for vascular density $\frac{S}{V}$ and parameter E

Figure 2.8 and Figure 2.9 illustrate the behavior of $\alpha(t)$ modeled by $\frac{S}{V}(t)$ using equation (2.55). Both figures begin with $\alpha_0 = 1.1$ when $\frac{S}{V}^0 = 50$ cm^{-1} and rise to $\alpha_\infty = 13.4$ when $\frac{S}{V}^\infty = 150$ cm^{-1}, or $\alpha_\infty = 17.3$ when $\frac{S}{V}^\infty = 250$ cm^{-1}. As in the $L_p(t)$ model, the only difference again is the length of time needed for the steady state to occur. The steady state is achieved in approximately 10 days with the frequency F_2, and 40 days with the frequency F_4.

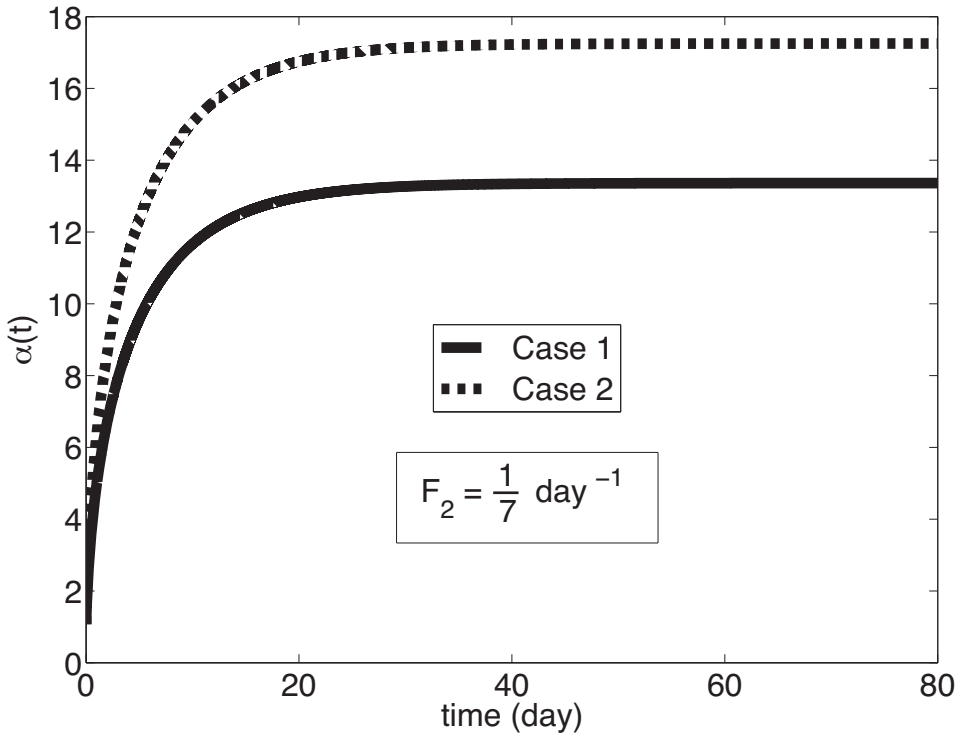

Figure 2.8: Behavior of $\alpha(t)$ modeled by $\frac{S}{V}(t)$ with $F_2 = \frac{1}{7}$ day^{-1}

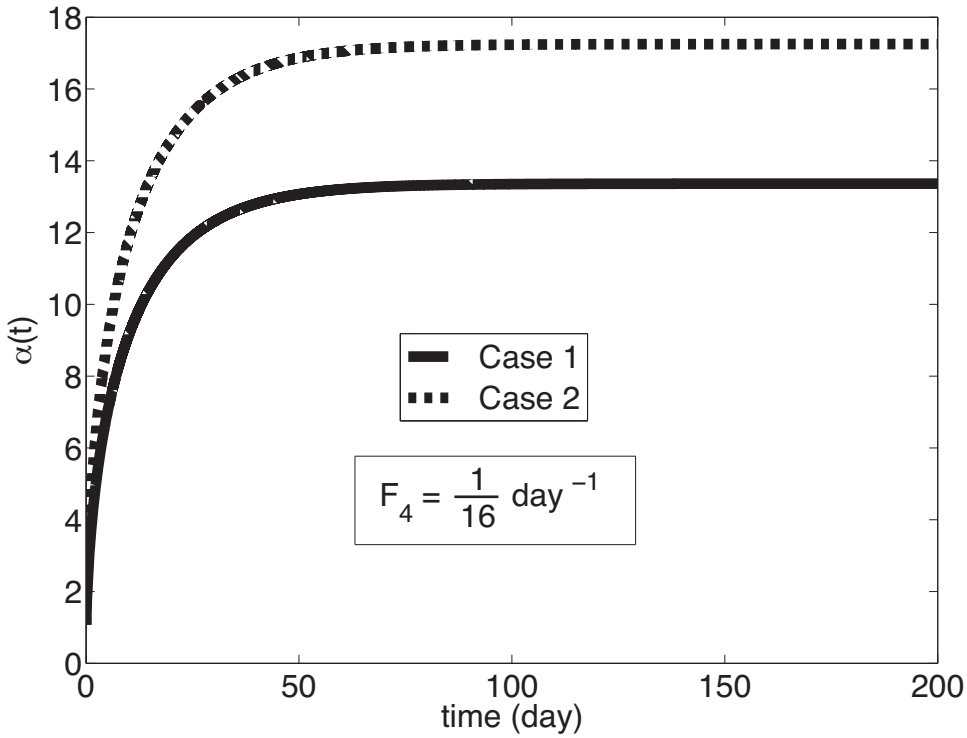

Figure 2.9: Behavior of $\alpha(t)$ modeled by $\frac{S}{V}(t)$ with $F_4 = \frac{1}{16}$ day^{-1}

Evolution of IFP modeled by $\frac{S}{V}(t)$

The analytic IFP transient state solution in full dimensional form is

$$p(r,t) = \frac{2\,p_v\,r}{R}\sum_{n=1}^{\infty}\frac{(-1)^{n+1}\sin(n\pi\frac{r}{R})}{n\pi}\,\psi(t)^{-1}\int_0^{\frac{t}{T}}\left(\psi(t)\,\alpha^2(t')\right)dt' + p_i, \tag{2.56}$$

where

$$\psi(t) = \exp\left(\left[\alpha_0^2(1+E) + (n\pi)^2\right]\frac{t}{T} + \frac{\alpha_0^2 E}{FT}(e^{-Ft} - 1)\right). \tag{2.57}$$

Similar to the case of IFP modeled by $L_p(t)$, $\alpha(t)$ affects the increase in IFP within a solid tumor as seen in Figure 2.10 and Figure 2.11. The figure shows how the IFP gradually increase to its steady state. Again, the rate at which steady state occurs depends on the frequency F. The smaller the value of the frequency F, the longer the IFP takes to attain its steady state.

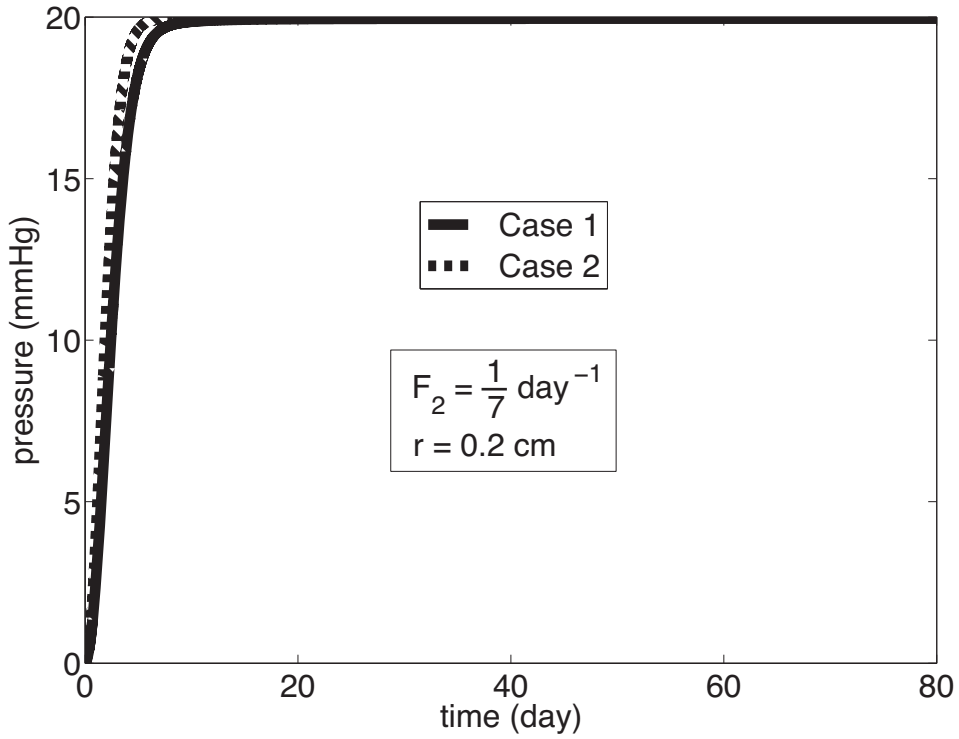

Figure 2.10: Evolution of IFP modeled by $\frac{S}{V}(t)$ **with** $F_2 = \frac{1}{7}$ **day**$^{-1}$

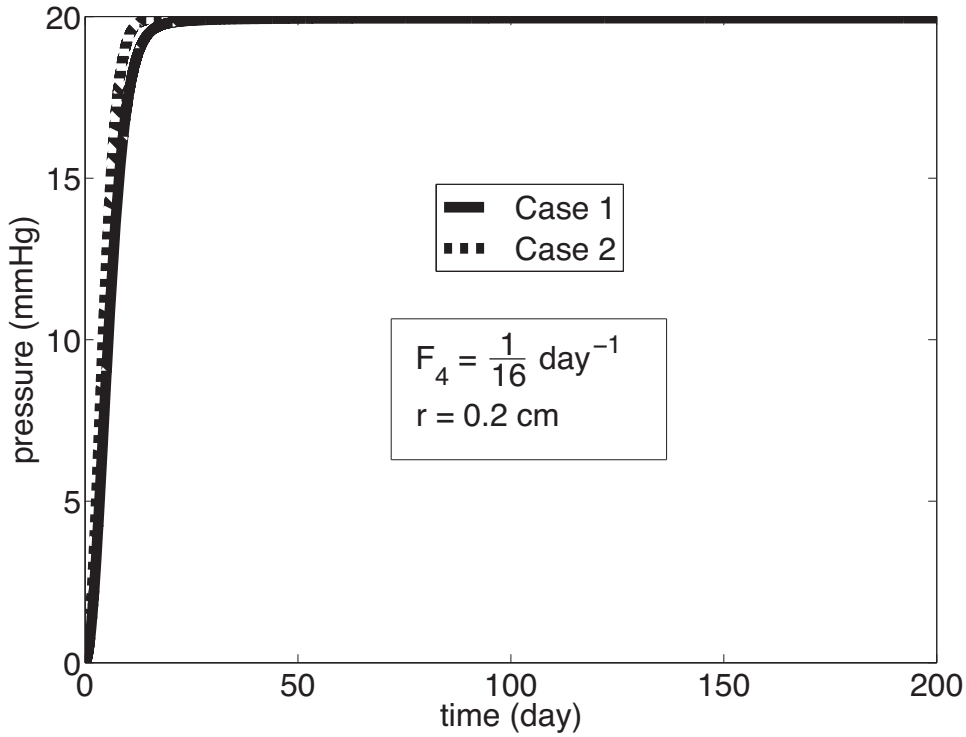

Figure 2.11: Evolution of IFP modeled by $\frac{S}{V}(t)$ with $F_4 = \frac{1}{16}$ day^{-1}

2.6 Application to anti-angiogenesis therapy

Angiogenesis is one of the hallmarks of cancer. It is a physiological process believed to be triggered by an imbalance of pro- and anti- angiogenic signals within solid tumors that creates an abnormal vasculature network characterized by dilated, tortuous and hyper-permeable capillaries. The consequences of the vascular abnormalities include temporal and spatial heterogeneity of blood flow and oxygen distribution, decreased levels of oxygen (known as hypoxia), and increased vascular density, capillary permeability, and increased tumor IFP within a solid tumor (Goel et al., 2011). This in turn leads to a hostile and chaotic tumor microenvironment and a significant reduction in the efficacy of cancer therapies, including radiotherapy and chemotherapy.

Since the discovery of an over-expression of vascular endothelial growth factor (VEGF) as a contributor to the angiogenic process, clinical efforts have found therapeutic ways to block the activity of VEGF. The control of VEGF, referred to as anti-VEGF therapy or anti-angiogenesis therapy, consists of altering the tumor vasculature to resemble the 'normal' vasculature of normal tissue. This 'vascular normalization' is characterized by a decrease in

the capillary permeability, in vascular density, and in tumor IFP. Vascular normalization also improves the oxygenation within a solid tumor (Carmeliet and Jain, 2011). The concentration of oxygen is not incorporated into the models studied in this work and could be of interest for future research.

The findings of the proposed mathematical model can be extended to possibly assist experimentalists in their efforts in identifying the optimal time interval to administer anti-angiogenesis therapy, along with other cancer treatments. This optimal time interval is defined as the period from the commencement of anti-angiogenesis therapy to the moment when the normalization effects wear off, following the cessation of the administration of anti-angiogenesis therapy. This is precisely the window of time during which therapeutic agents, such as radiation therapy and chemotherapy, can be effectively delivered to possibly prevent further solid tumor development and metastasis.

Mathematical model for anti-angiogenesis therapy

The anti-angiogenesis therapy mathematical model is similar to the previous models where the evolution of IFP from a healthy interstitium to a cancerous state was examined. The PDE (2.21) subject to the boundary conditions (2.22), and under the same assumptions is employed; however, it is extended to predict the IFP distribution within a solid tumor due to the effects of anti-angiogenesis therapy. The main feature of the anti-angiogenesis therapy models is that IFP decreases from the tumor steady-state to the normalized state and increases from the normalized state to the tumor steady-state either by a change in the hydraulic permeability of the vascular walls modeled by $L_p(t)$, or in the vascular density modeled by $\frac{S}{V}(t)$.

When analyzing the IFP distribution due to the effects of anti-angiogenesis therapy, three time intervals are considered, as seen in Table 2.6. Within the three intervals, the continuous function $\alpha^2(t)$ is modeled by either $L_p(t)$ or $\frac{S}{V}(t)$ to predict the IFP change due to the various stages in anti-angiogenesis therapy.

Therapy timeline	Time interval	Description
Pre-therapy	$0 \leq t \leq t_1$	IFP evolves from a normal tissue state at time $t = 0$ to a tumor state at time t_1
During therapy	$t_1 \leq t \leq t_2$	therapy is administered at time t_1 and the IFP decreases until time t_2 when the effects of the therapy wear off
Post-therapy	$t_2 \leq t \leq t_3$	from time t_2 the IFP rebounds back to the tumor state values at some time t_3

Table 2.6: Anti-angiogenesis therapy timeline

Within every time interval the representation of $\alpha^2(t)$ changes its form. In the time intervals between 0 and t_1 and between t_2 and t_3, $\alpha^2(t)$ assumes the exponential form as modeled by $L_p(t)$ (2.23) or by $\frac{S}{V}(t)$ (2.27) in full dimensional form as previously elaborated on. The effects of anti-angiogenesis therapy modeled by either $L_p(t)$ or $\frac{S}{V}(t)$ next.

Model of IFP evolution by $L_p(t)$ with anti-angiogenesis therapy

To simulate the effect of anti-angiogenesis, an exponentially decreasing function of time is considered

$$\alpha^2(t) = P + Qe^{-Mt}, \quad t_1 \leq t \leq t_2, \tag{2.58}$$

where P, Q and M are constants. The parameters P and Q can be determined the following way. As anti-angiogenic therapy is applied after the IFP has reached the tumor steady state, the first condition applied is

$$\alpha^2(t_1) = \alpha^2_\infty = \frac{R^2}{K} L_p^\infty \frac{S}{V}, \tag{2.59}$$

and when $\alpha^2(t)$ decreases to its minimum at t_2, the second condition applied is

$$\alpha^2(t_2) = \alpha^2_N = \frac{R^2}{K} L_p^N \frac{S}{V}, \tag{2.60}$$

where α_N is the normalized value of the dimensionless parameter. Thus, the function (2.58) is calculated to be

$$\alpha^2(t) = \alpha^2_\infty \left[1 + J\left(e^{-Mt} - e^{-Mt_1}\right)\right], \quad t_1 \leq t \leq t_2, \tag{2.61}$$

where the constant J is

$$J = \left(\frac{L_p^N}{L_p^\infty} - 1\right)\left(e^{-Mt_2} - e^{-Mt_1}\right)^{-1}. \tag{2.62}$$

Value for the frequency parameter M

Since there are three time intervals in the anti-angiogenesis therapy, three different frequencies are needed. In the time interval from 0 to t_1, the parameter D (2.29) assumes 1 day^{-1} for an intermediate growing tumor (Table 2.3). The same frequency value, denoted as D^*, is used in the interval from t_2 to t_3. This assumption is based on the fact that it takes approximately the same amount of time for the IFP to rebound back to its tumor value as it takes initially starting with a healthy interstitium, since an increase in L_p is a fast process within a solid tumor (Bates and Curry, 1996).

All that remains now is to determine the parameter M and the endpoints t_1 and t_2 of the time interval over which anti-angiogenic therapy is effective. The IFP grows until it reaches the tumor steady state value and is capped off at time t_1 which marks the commencement of the anti-angiogenesis therapy. From t_1 to t_2, the parameter M assumes the frequency value of $\frac{1}{3}$ day^{-1}. It has been observed in human transplanted carcinomas growing in mice that with a single injection of anti-VEGF treatment DC101 the vascular permeability drops to approximately 50 percent of its initial value within 3 days (Tong et al., 2004). Furthermore, the normalization window is short lived – about 6 days (Jain, 2005, 2008). For the purposes of our model, the transient normalization window runs for approximately 15 days in order to simulate the effects of anti-VEGF treatment, since Tong et al. (2004) reported that the anti-VEGF treatment DC101 significantly reduces the tumor IFP even after 15 days. Around day 15, denoted as time t_2, the anti-angiogenesis therapy begins to wear off and the IFP begins to rise up to time t_3.

Results of transient IFP modeled by $L_p(t)$ with anti-angiogenesis therapy

The PDE (2.21) with the same boundary conditions (2.22) is integrated with the appropriate initial condition in each time interval, and with the appropriate form of the function $\alpha^2(t)$ given by

$$\alpha^2(t) = \frac{R^2}{K} L_p(t) \frac{S}{V}, \tag{2.63}$$

where $\frac{S}{V}$ is regarded as a parameter in order to gain an insight into how the pressure profile changes with the vascular surface density. The results are shown in Figure 2.12, where the IFP profile of the tumor is simulated for three different values of $\frac{S}{V}$ – namely the lower extreme, the average value, and higher extreme, as seen in Table 2.1. The parameters R, K, L_p^∞ are taken from Table 2.1. The value of normalized hydraulic permeability parameter L_p^N, 3.7×10^{-7} cm second^{-1} mmHg^{-1}, has been taken from Jain et al. (2007). From Figure 2.12, it is clear that the "window" of reduced IFP in the middle of the tumor (located 0.2 cm from the center) is noticeable only for the lower extreme of the vascular density. The IFP barely decreases for the average value and higher extreme value of $\frac{S}{V}$.

As a sensitivity analysis, Figure 2.13 shows that values of $\frac{S}{V}$ lower than 50 cm^{-1} further decrease the IFP in the time interval $t_1 \leq t \leq t_2$. However, when $\frac{S}{V}$ is 20 cm^{-1}, 30 cm^{-1} or 40 cm^{-1}, the corresponding tumor values of α_∞ are 4.9, 6.0 and 7.0 at times t_1 and t_3 which are barely high enough to increase the IFP to a cancerous state according to Jain et al. (2007). Lastly, Figure 2.14, using $\frac{S}{V} = 50$ cm^{-1}, shows that increasing the frequency value M only forces the IFP to decrease faster to its steady state within the 15 day normalization window.

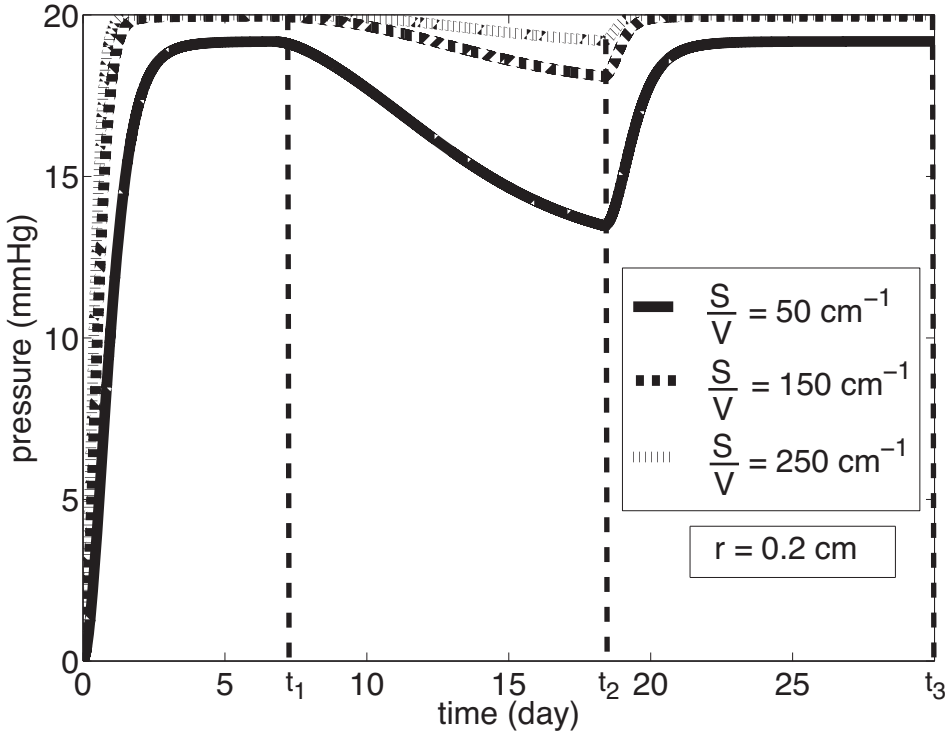

Figure 2.12: Evolution of IFP modeled by $L_p(t)$ with $M = \frac{1}{3}$ day^{-1}

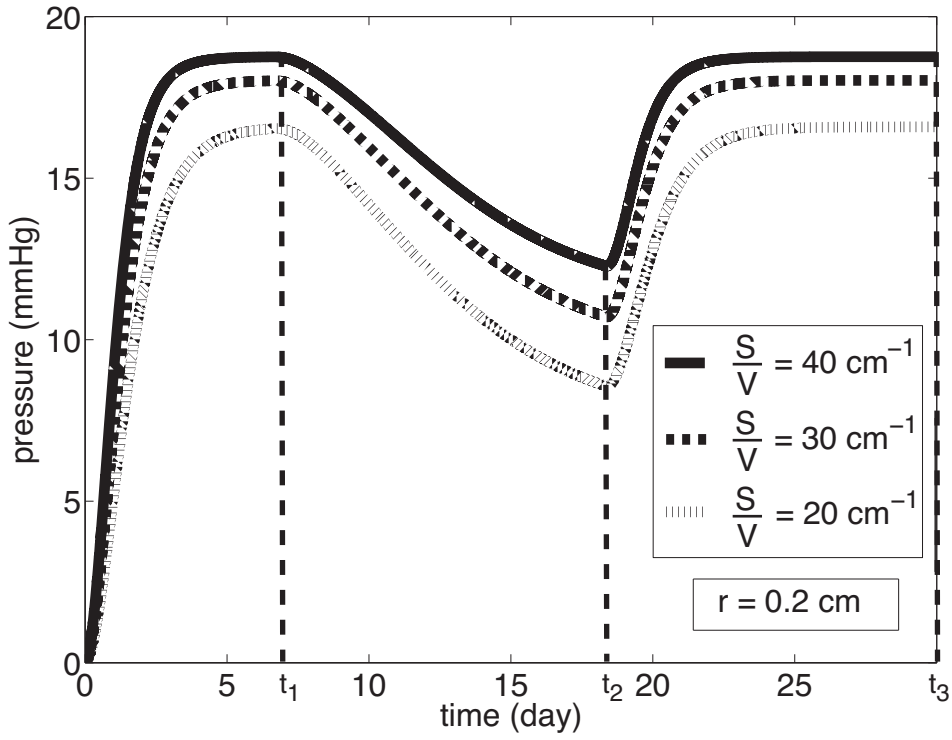

Figure 2.13: Evolution of IFP modeled by $L_p(t)$ with $\frac{S}{V}$ = 20, 30 and 40 cm^{-1}

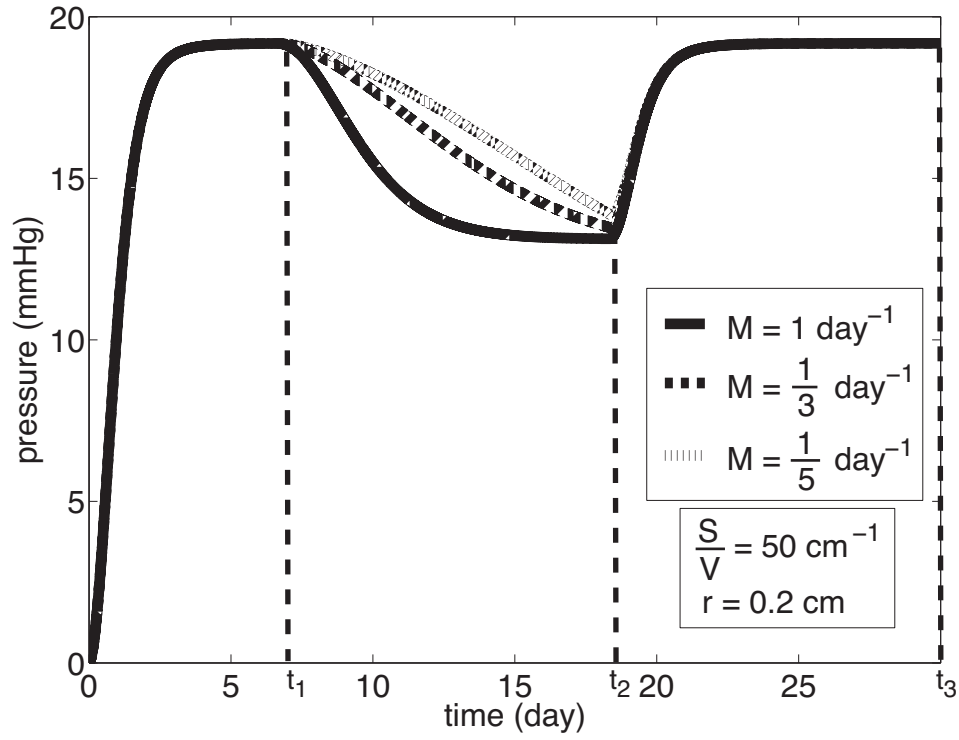

Figure 2.14: Evolution of IFP modeled by $L_p(t)$ with M = 1, $\frac{1}{3}$ and $\frac{1}{5}$ day^{-1}

Model of IFP evolution by $\frac{S}{V}(t)$ with anti-angiogenesis therapy

The effect of anti-angiogenesis modeled by $\frac{S}{V}(t)$ is formulated again by an exponentially decreasing function of time

$$\alpha^2(t) = U + Ve^{-St}, \quad t_1 \le t \le t_2, \tag{2.64}$$

where U, V and S are constants. The parameters U and V are calculated as follows. As anti-angiogenic therapy is applied after the IFP has reached the tumor steady state, the first condition applied is

$$\alpha^2(t_1) = \alpha^2_\infty = \frac{R^2}{K} L_p^\infty \frac{S}{V}^\infty, \tag{2.65}$$

and when $\alpha^2(t)$ decreases to its minimum at t_2, the second condition applied is

$$\alpha^2(t_2) = \alpha^2_N = \frac{R^2}{K} L_p^N \frac{S}{V}^N, \tag{2.66}$$

where $\frac{S}{V}^N$ is the normalized value of the vascular density. Thus, the function (2.64) is calculated to be

$$\alpha^2(t) = \alpha^2_\infty \Big[1 + X\Big(e^{-St} - e^{-St_1}\Big)\Big], \quad t_1 \le t \le t_2, \tag{2.67}$$

where the constant X is

$$X = \left(\frac{L_p^N \frac{S}{V}^N}{L_p^\infty \frac{S}{V}^\infty} - 1\right)\Big(e^{-St_2} - e^{-St_1}\Big)^{-1}. \tag{2.68}$$

Value for the frequency parameter S

In the time interval from 0 to t_1, the parameter F (2.29) assumes $F_2 = \frac{1}{7}$ day^{-1} for a fast growing tumor with increased $\frac{S}{V}$ from Table 2.4. The same frequency values, denoted as F_2^*, are used in the interval from t_2 to t_3. This is based on the assumption that the vascular density would increase after anti-angiogenesis therapy at the same frequency as it did in the case of an increase from a healthy interstitium to a cancerous state.

The frequency parameter S and the endpoints t_1 and t_2 of the time interval over which anti-angiogenic therapy is effective are determined in the following way. Once the IFP reaches its tumor steady state, it is capped off at t_1, marking the commencement of the anti-angiogenesis therapy. From t_1 to t_2, the parameter S assumes the frequency value of $\frac{1}{5}$ day^{-1}. Tong et al. (2004) reported that, in human transplanted carcinomas growing in

mice, within $2-3$ days after a single injection of DC101 many of the vessels become less tortuous besides being smaller in diameter, and by day 5, in some regions of the tumor, some of the vessels regressed completely. The effects on the IFP due to a 'normalized' vasculature are again simulated for approximately 15 days. Around day 15, denoted as time t_2, the IFP decrease is stopped, which represents the loss of the effects of DC101. From then on, the IFP rebounds to a tumor state value at time t_3.

Results of transient IFP modeled by $\frac{S}{V}(t)$ with anti-angiogenesis therapy

The evolution of IFP due to anti-angiogenesis therapy modeled by $\frac{S}{V}(t)$ is approached differently compared to the previous case. Clinical studies have shown that anti-angiogenesis therapy prunes the newly formed blood vessels and shrinks and decreases the permeability of the pre-existing capillaries (Carmeliet and Jain, 2011). Thus, the parameter $\frac{S}{V}$ is not kept constant, but rather changes. Again, the PDE (2.21) with the same boundary conditions (2.22) is integrated with the appropriate initial condition in each time interval and with the appropriate form of the function $\alpha^2(t)$.

Under the normal tissue state and the vascular normalization process, $\frac{S}{V}$ assumes the lower extreme value of 50 cm^{-1}. The vascular normalization is characterized by the range $50-250$ cm^{-1} for the values of $\frac{S}{V}$, according to Jain et al. (2007); however, any value greater than 50 cm^{-1} results in a value of α_N close to tumor α_∞ value which does not effectively decrease the IFP. Furthermore, in modeling by $\frac{S}{V}(t)$, when a tumor attains tumor values at time t_1 and t_3, $\frac{S}{V}$ is either 150 cm^{-1}, which is the average value, or 250 cm^{-1}, which is the higher extreme. The changes in vascular density $\frac{S}{V}$ within the anti-angiogenesis therapy timeline are summarized in two cases in Table 2.7.

Time interval	Case A	Case B
$0 \le t \le t_1$	normal tissue $\rightarrow$ tumor $\frac{S}{V}^0 = 50\ \text{cm}^{-1} \rightarrow \frac{S}{V}^\infty = 150\ \text{cm}^{-1}$	normal tissue $\rightarrow$ tumor $\frac{S}{V}^0 = 50\ \text{cm}^{-1} \rightarrow \frac{S}{V}^\infty = 250\ \text{cm}^{-1}$
$t_1 \le t \le t_2$	tumor $\rightarrow$ normalized $\frac{S}{V}^\infty = 150\ \text{cm}^{-1} \rightarrow \frac{S}{V}^N = 50\ \text{cm}^{-1}$	tumor $\rightarrow$ normalized $\frac{S}{V}^\infty = 250\ \text{cm}^{-1} \rightarrow \frac{S}{V}^N = 50\ \text{cm}^{-1}$
$t_2 \le t \le t_3$	normalized $\rightarrow$ tumor $\frac{S}{V}^N = 50\ \text{cm}^{-1} \rightarrow \frac{S}{V}^\infty = 150\ \text{cm}^{-1}$	normalized $\rightarrow$ tumor $\frac{S}{V}^N = 50\ \text{cm}^{-1} \rightarrow \frac{S}{V}^\infty = 250\ \text{cm}^{-1}$

Table 2.7: Values for vascular density $\frac{S}{V}$ in anti-angiogenesis therapy timeline

In conjunction with $\frac{S}{V}$ changing, the value for L_p needs to represent the state of the tumor in the model as well. Thus, the values of L_p^0 and L_p^∞ are taken from Table 2.1, and the normalized L_p^N is 3.7×10^{-7} cm second^{-1} mmHg^{-1} (Jain et al., 2007). Lastly, R and K are kept constant, and their respective values can be found in Table 2.1.

In the middle of the tumor (located 0.2 cm from the center), Figure 2.15 shows a 25% drop in IFP in the time interval $t_1 \leq t \leq t_2$ for both Case A and Case B from Table 2.7. In Figure 2.16, if the normalized $\frac{S}{V}^N$ is less than 50 cm^{-1} at time t_2, while the tumor $\frac{S}{V}^\infty$ assumes the average value of 150 cm^{-1} at times t_1 and t_3, the IFP drops approximately 35% – nowhere near the IFP for a healthy interstitium. Again, considering Case A for the change in $\frac{S}{V}$ in Table 2.7, a decrease in the frequency S in the time interval $t_1 \leq t \leq t_2$ only delays the IFP in reaching its steady state, as seen in Figure 2.17.

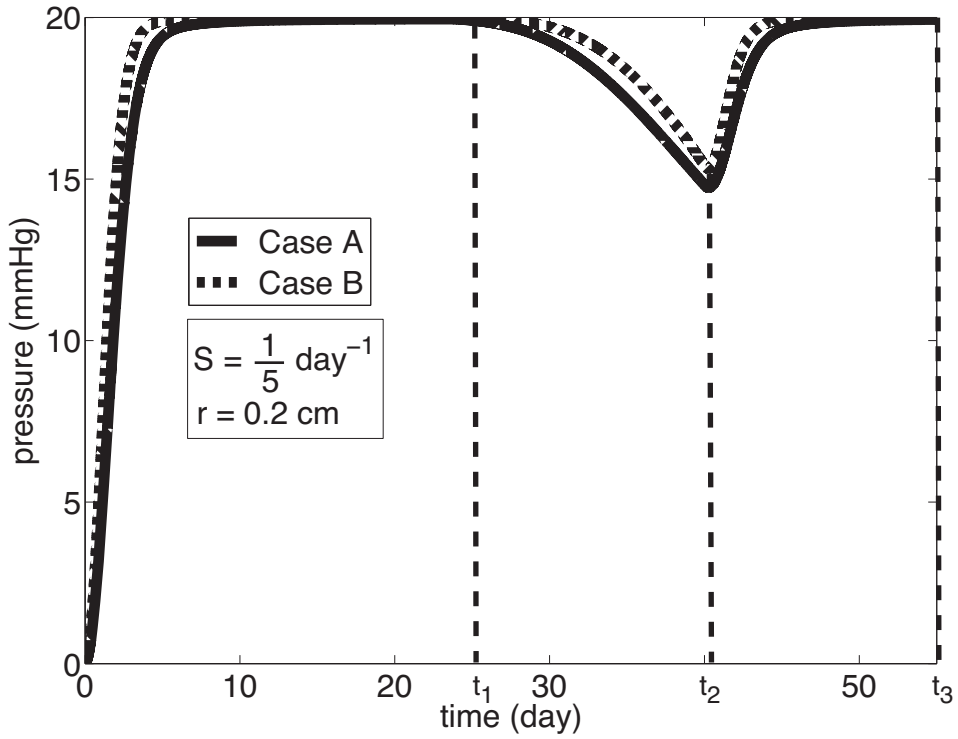

Figure 2.15: Evolution of IFP modeled by $\frac{S}{V}(t)$ with $S = \frac{1}{5}$ day^{-1}

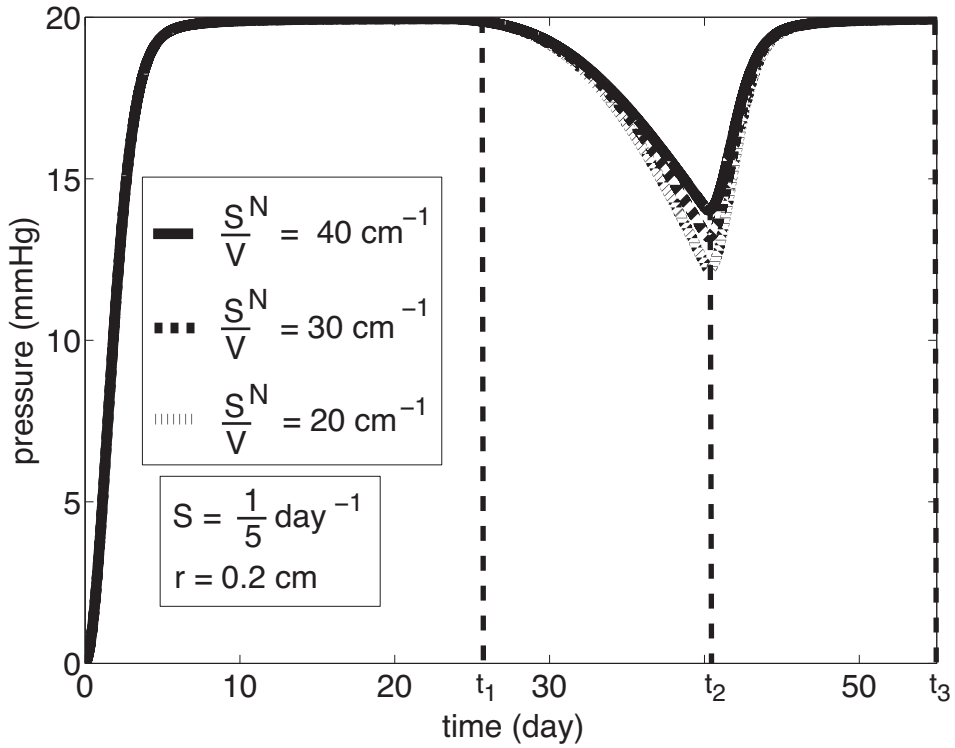

Figure 2.16: Evolution of IFP modeled by $\frac{S}{V}(t)$ with $\frac{S}{V}^N$ = 20, 30 and 40 cm^{-1}

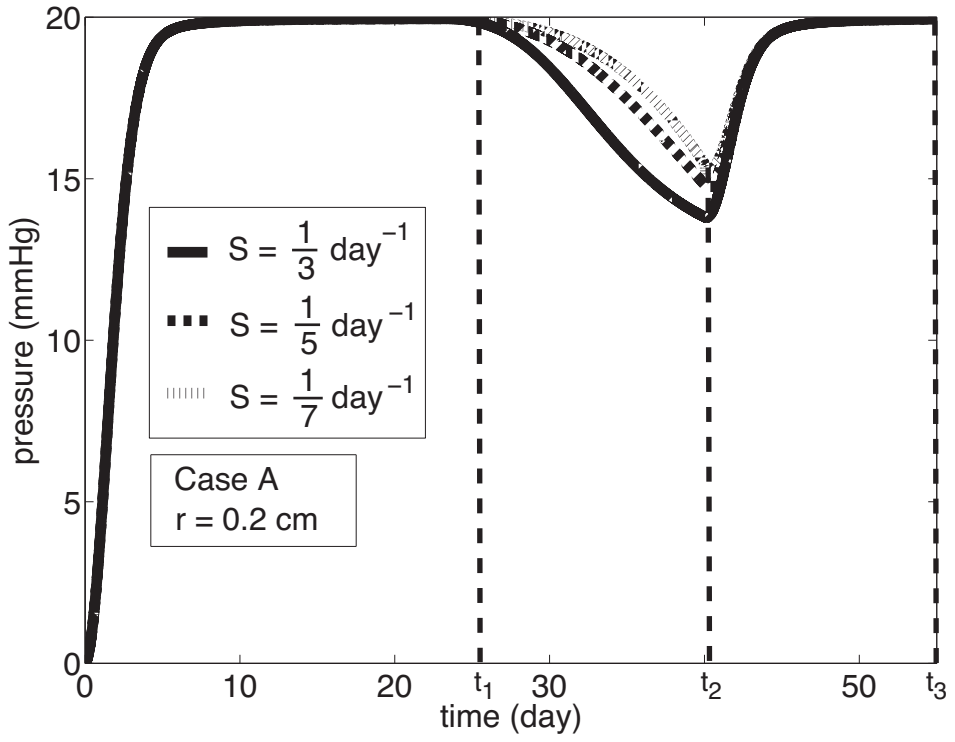

Figure 2.17: Evolution of IFP modeled by $\frac{S}{V}(t)$ with $S = \frac{1}{3}$, $\frac{1}{5}$ and $\frac{1}{7}$ day^{-1}

From both models which describe the rise of IFP from normal tissue values to tumor tissues values and the application to anti-angiogenesis therapy, it is clear that the capillary permeability L_p has a greater effect on the tumor IFP than the vascular density $\frac{S}{V}$. In the case of the evolution of IFP modeled by $L_p(t)$ from normal tissue values to tumor values, L_p depends on the tumor growth rate and drastically influences the IFP, as seen in Figures 2.5-2.7. Modeling by $\frac{S}{V}(t)$, the IFP reaches tumor steady state roughly at the same time independent of the type of tumor growth which shows that vascular density may not be an important contributor to the IFP evolution. Similar behavior of L_p and $\frac{S}{V}$ are also seen in the model which incorporates the effects of anti-angiogenesis therapy. The model of IFP evolution by $L_p(t)$ shows that the decrease in IFP was influenced highly by the tumor growth rate, as seen in Figure 2.14. Whereby having different values of $\frac{S}{V}$, which were kept constants, also influenced the amount of IFP decrease within a solid tumor, as seen in Figure 2.12. However, modeling S/V as a time dependent function appears to have the same impact on the decrease in IFP independent of the actual change in S/V, as seen in Figure 2.15, and of the tumour growth rate as in Figure 2.17. Thus, from a clinical perspective, according to these models which incorporate anti-angiogenesis therapy, the primary parameter to focus on is the capillary permeability L_p, which highly influences the IFP change within a tumor. The models also predict that the optimal time for anti-angiogenesis therapy in conjunction with other cancer treatments such as radiotherapy and chemotherapy would be after time t_1 and before t_2. Note that these models are very crude and only focus on the changes in capillary permeability and vascular density. Within a solid tumor, there are other changes in the microenviroment that occur such as hypoxia and acidosis which are not accounted for and may be of importance to consider.

Chapter 3

Testing the approximation $(2\mu + \lambda)e(r,t) = p(r,t)$ in a hollow spherically symmetric domain

3.1 Introduction

As seen in Chapter 2, the mathematical model adopted in this Thesis is built on two partial differential equations. The first equation is the continuity equation with field variables which depend on both space $\underline{r} = (x, y, z)$ in centimeters and time t in seconds:

$$\frac{\partial e}{\partial t} - K\nabla^2 p = \frac{L_p S}{V}(p_v - p), \tag{3.1}$$

where $e(\underline{r}, t)$ is the tissue dilatation being the change of volume per unit volume of both the fluid and the solid phase together, K is the hydraulic conductivity coefficient (with units cm^2 second^{-1} mmHg^{-1}), L_p is the permeability of the capillary walls with (units in cm second^{-1} mmHg^{-1}), and $\frac{S}{V}$ is the surface area per unit volume of blood vessels (with units cm^{-1}). All pressure quantities are measured in mmHg. The variable $p(\underline{r}, t)$ is the interstitial fluid pressure (IFP) and p_v is the microvascular pressure. The second equation contains the relation between e and p which is derived in Appendix A, equation (A28), namely

$$(2\mu + \lambda)\nabla^2 e = \nabla^2 p, \tag{3.2}$$

where μ and λ are the Lamé parameters for elasticity of a solid material (with units mmHg). It is evident that equation (3.1) alone is not closed, and thus, equation (3.2) is needed. As mentioned in Chapter 2 and Appendix A, there is a special case in which equation (3.2) implies a linear relation between e and p, namely

$$(2\mu + \lambda)e = p. \tag{3.3}$$

To summarize the argument, equation (3.2) may be rewritten as

$$\nabla^2(p - (2\mu + \lambda)e) = 0, \tag{3.4}$$

which is equivalent to

$$\begin{cases} p - (2\mu + \lambda)e = f(\underline{r}, t), \\ \nabla^2 f = 0, \end{cases} \tag{3.5}$$

where $f(\underline{r}, t)$ is an unknown harmonic function. Only in the case when f is identically zero, the combination of equations (3.1) and (3.5) gives

$$\frac{1}{2\mu + \lambda} \frac{\partial p}{\partial t} - K\nabla^2 p = \frac{L_p S}{V}(p_v - p), \tag{3.6}$$

which is the PDE for the IFP used in Chapter 2.

Taking $f \equiv 0$ in equation (3.5) is a special case which appears in many places in the ground water flow literature (Bear, 1988). It holds in the one-dimensional case when the fluid flow as well as deformations occur in one direction only, as discussed in Verruijt (1969). Also, $f \equiv 0$ is valid in the three-dimensional case, assuming that the radial displacements vanish identically. However, in the present context, it is difficult to justify physically such an assumption. Furthermore, after investigating the relation between e and p in more detail in spherical coordinates under the assumption of radial symmetry, it appears that taking f to be identically zero is questionable; for, as shown in Appendix B, even in the simplest case of spherical symmetry, the function $f(\underline{r}, t)$ does not vanish, but remains as an arbitrary function of time,

$$f = b(t). \tag{3.7}$$

This form of f still leaves two unknown variables in equation (3.1),

$$\frac{1}{2\mu + \lambda}\left(\frac{\partial p}{\partial t} - \frac{\partial b(t)}{\partial t}\right) - K\nabla^2 p = \frac{L_p S}{V}(p_v - p), \tag{3.8}$$

and so even in the simplest case of spherical symmetry the condition $\frac{\partial b}{\partial t} = 0$ needs to be satisfied for the pressure to obey equation (3.6). De Leeuw (1965) first found the necessary and sufficient conditions on f by considering a hollow cylindrical sand drain under the assumptions of axial symmetry and plane strain. Using Biot's equations of the linear theory of poroelasticity (1941) and assuming that the fluid is incompressible, De Leeuw described the three-dimensional system by two equations, both depending on space r and time t, which in his notation and coordinate-independent form are as follows:

$$\frac{k}{\gamma_w}\nabla^2 u = \frac{\partial e}{\partial t}, \tag{3.9}$$

where k is the permeability, γ_w is the unit weight of water, u is water pressure, and e is the volume dilatation; the second equation reads

$$(K + \frac{4}{3}G)\nabla^2 e = \nabla^2 u, \tag{3.10}$$

where K is the compressibility modulus and G is the shear modulus of the solid constituent.

By expressing equation (3.10) in cylindrical coordinates r, θ, and z, and integrating, it follows that

$$(K + \frac{4}{3}G)e = u + g(r, \theta, z, t), \tag{3.11}$$

where g must satisfy $\nabla^2 g = 0$. Under the assumption of axial symmetry and plane strain, that is, $\frac{\partial}{\partial \theta} = 0$ and $\frac{\partial}{\partial z} = 0$, except for $\frac{\partial u_z}{\partial z} = \text{constant}$, one finds

$$(K + \frac{4}{3}G)e = u + g(t), \tag{3.12}$$

where now g depends solely on time. Taking the derivative of equation (3.12) with respect to t and substituting into equation (3.9) yields

$$\frac{k}{\gamma_w}\nabla^2 u = \frac{1}{K + \frac{4}{3}G}\left(\frac{\partial u}{\partial t} + \frac{\partial g}{\partial t}\right), \tag{3.13}$$

which gives a "heat-type" equation when $\frac{\partial g}{\partial t} = 0$. De Leeuw then goes on to show that for the sand drain problem appropriate boundary conditions need to be considered in order to make $\frac{\partial g}{\partial t}$ precisely zero; consequently, the hydraulic pressure and the dilatation are exactly proportional in that case.

3.1.1 Some details of De Leeuw (1965) argument

De Leeuw is careful to point out that this result is not generally valid, and it certainly does not hold in spherical coordinates. However, in most of the porous media literature, as well as in Chapter 2, the assumption that e and p are proportional has been used; hence, given that the condition $g = 0$ is only an approximation, the question that needs to be answered is: how good an approximation is it?

In order to test this assumption, and therefore answer the question, a review of the De Leeuw (1965) paper in more detail is needed so as to see how the geometry - and hence the boundary conditions - affect the problem. De Leeuw solved the system of PDEs (3.9) and

(3.10) for a vertical sand drain consisting of a hollow cylindrical body as sketched in the figure below,

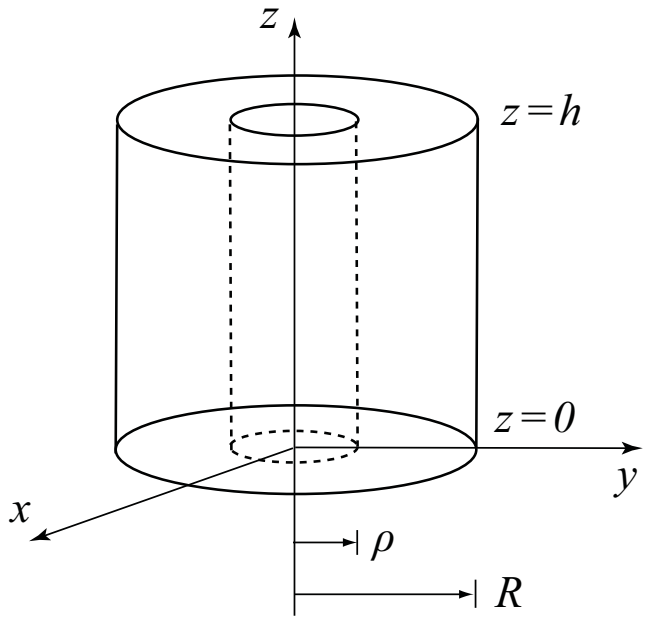

Figure 3.1: Hollow cylindrical domain

with the following boundary conditions

$$0 < z < h,\ r = R,\ u_r = f_1(t), \tag{3.14}$$

$$0 < z < h,\ r = \rho,\ u_r = f_2(t), \tag{3.15}$$

$$z = h,\ \rho < r < R,\ p_v = f_3(t), \tag{3.16}$$

$$0 < z < h,\ r = \rho,\ u = f_4(t), \tag{3.17}$$

$$0 < z < h,\ r = R,\ \frac{\partial u}{\partial r} = 0, \tag{3.18}$$

$$z = 0 \text{ and } z = h,\ 0 < r < R,\ \frac{\partial u}{\partial z} = 0, \tag{3.19}$$

where h is the height of the cylinder, ρ and R are the inner and outer radii of the cylinder, and p_v is the applied load. The coordinate system is cylindrical, and plane strain and axial symmetry are assumed. The functions of time $f_i(t)$, where $i = 1, 2, 3, 4$, are arbitrary. Note that the notation of De Leeuw is a bit confusing since u_r is radial displacement while u is the hydraulic pressure.

Using the Laplace transform, De Leeuw found the general solution of the two coupled PDEs, that is, he found the transformed quantities $\overline{e}(\underline{r}, s)$ and $\overline{u}(\underline{r}, s)$. Finally, taking advantage of the equation of motion, applying the transformed boundary conditions, and inverting

the Laplace transform, De Leeuw was able to show that the function g in equation (3.12) must satisfy the following condition:

$$\frac{\partial g}{\partial t} = -\frac{\partial}{\partial t}\left[\frac{4GR\rho}{R^2-\rho^2}\left(\frac{f_1}{\rho}-\frac{f_2}{R}\right)+f_3+2f_4\right]. \tag{3.20}$$

It is clear that in cylindrical geometry, with plane strain and axial symmetry, and with the special boundary conditions

$$f_1 = f_2 = f_4 = 0, \qquad f_3 = p_v = \text{constant}, \tag{3.21}$$

the harmonic function g is a constant, which can be taken to be zero. This makes the volume dilatation e proportional to the hydrostatic pressure u. Also, it is obvious from equation (3.20) that this proportionality does not exist if even one of the functions f_i depends on time.

3.1.2 The case of a spherically symmetric sand drain

In order to simplify the mathematical analysis, De Leeuw (1965) considered the case of consolidation in the absence of sources. Therefore, for the same reason, the right-hand side of equation (3.1) is set to zero and equation (3.2) is kept unchanged. For the reader's convenience, these equations are repeated below:

$$\frac{\partial e}{\partial t} = \frac{\kappa}{\eta}\nabla^2 p, \tag{3.22}$$

where the hydraulic conductivity has been expressed in terms of the permeability κ and the viscosity η, and

$$(2\mu+\lambda)\nabla^2 e = \nabla^2 p, \tag{3.23}$$

which is equivalent to

$$\begin{cases} p-(2\mu+\lambda)e = f(\underline{r},t), \\ \\ \nabla^2 f = 0. \end{cases} \tag{3.24}$$

Now, if $f(\underline{r},t)\equiv 0$, then equation (3.22) becomes

$$\frac{\partial p}{\partial t} = \gamma\nabla^2 p, \tag{3.25}$$

where $\gamma = \frac{\kappa}{\eta}(2\mu+\lambda)$, and the problem is reduced to a "heat-type" equation for the hydraulic pressure.

The enormous mathematical simplification resulting from this kind of argument represents explains the popularity of the assumption of proportionality of hydraulic pressure and

dilatation. The analysis is far more complicated in the general case, for as pointed out already by Verrujit (1969), the solution of the basic PDEs (3.22) and (3.23) is not enough, since the boundary conditions for the elastic material are given in terms of stresses or displacements – not in terms of dilatation. Therefore, after obtaining the general solution for $e(\underline{r}, t) = \nabla \cdot \underline{u}$ and $p(\underline{r}, t)$ from equations (3.22) and (3.23), the equation of motion is employed in order to solve for $\underline{u}(\underline{r}, t)$, namely

$$\mu \nabla^2 \underline{u} + (\mu + \lambda) \nabla e = \nabla p, \tag{3.26}$$

where the boundary conditions can be enforced. This problem is far more difficult than solving the "heat-type" equation (3.25) with a constant initial condition and constant boundary conditions.

Going back to the question raised earlier - namely, how good an approximation $f(\underline{r}, t) \equiv 0$ is in the case of a homogeneous, spherically symmetric domain - a test can be constructed as follows:

1. Solve equation (3.25) with appropriate initial and boundary conditions;
2. Find the general solution of the system of PDEs (3.22) and (3.23) to get the general form of $e(\underline{r}, t)$ and $p(\underline{r}, t)$;
3. Substitute these into equation (3.26) and solve for $\underline{u}(\underline{r}, t)$ with the same boundary conditions as in Step 1, and thus, calculate the stress tensor, and hence, the pressure.
4. Compare the hydraulic pressure values obtained in Step 1 and Step 3.

3.2 Step 1: Approximated case

Equation (3.25) from Section 3.1 which is analogous to the heat equation is solved analytically with appropriate initial and boundary conditions.

Since the interest is to study the pressure behavior within a sphere with a hollow spherical center as shown in Figure 3.2, the PDE (3.25) is rewritten in spherical coordinates, assuming radial symmetry:

$$\frac{\partial p(r,t)}{\partial t} = \gamma \left(\frac{2}{r} \frac{\partial p(r,t)}{\partial r} + \frac{\partial^2 p(r,t)}{\partial r^2} \right). \tag{3.27}$$

The boundary conditions imposed on equation (3.27) are analogous to those in De Leeuw (1965) paper for a cylindrical body with a cylindrical hollow center for the sand drain problem, namely

$$\begin{cases} p(r_i, t) = f_1(t), \\ p(r_o, t) = f_2(t), \\ p(r, 0) = 0, \end{cases} \tag{3.28}$$

where r_i and r_o are the inner and outer radii of the sphere, and $f_1(t)$ and $f_2(t)$ are arbitrary functions of time. Note that in this case no boundary conditions need to be prescribed for the stresses; hence, there is no need to bring in explicitly the equation of motion (3.26).

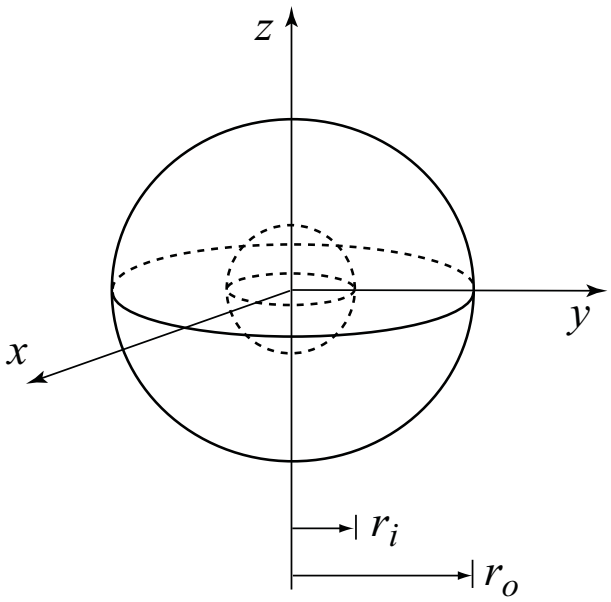

Figure 3.2: Hollow spherical domain

This boundary value problem is solved by applying the Laplace transform:

$$P(r, s) = \int_0^\infty p(r, t) \exp(-st) dt. \tag{3.29}$$

The PDE (3.27) and the boundary conditions are transformed as:

$$\frac{d^2P}{dr^2} + \frac{2}{r}\frac{dP}{dr} - \frac{s}{\gamma}P = 0 \tag{3.30}$$

with

$$\begin{cases} P(r_i, s) = F_1(s), \\ \\ P(r_o, s) = F_2(s). \end{cases} \tag{3.31}$$

The initial condition $P(r, 0) = 0$ was used in deriving equation (3.30).

To proceed in solving the differential equation (3.30), a change of variable is applied. Let $P = \frac{y(r,s)}{r}$. Then, $\frac{dP}{dr} = \frac{y'r-y}{r^2}$ and $\frac{d^2P}{dr^2} = \frac{y''}{r} - 2\frac{y'}{r^2} + \frac{2y}{r^3}$, and equation (3.30) reads

$$\left(\frac{y''}{r} - 2\frac{y'}{r^2} + \frac{2y}{r^3}\right) + \frac{2}{r}\left(\frac{y'r-y}{r^2}\right) - \frac{s}{\gamma}\frac{y}{r} = 0, \tag{3.32}$$

which reduces to

$$y'' - \frac{s}{\gamma}y = 0. \tag{3.33}$$

The characteristic equation, $q^2 - \frac{s}{\gamma} = 0$, gives $q = \pm\sqrt{\frac{s}{\gamma}}$. Thus, the general solution is

$$y = c_1(s)e^{\sqrt{\frac{s}{\gamma}}r} + c_2(s)e^{-\sqrt{\frac{s}{\gamma}}r}, \tag{3.34}$$

where $c_1(s)$ and $c_2(s)$ are so far arbitrary functions of s. The solution (3.34) can be written in the form

$$y = M(s)\sinh(\sqrt{\frac{s}{\gamma}}r) + N(s)\cosh(\sqrt{\frac{s}{\gamma}}r), \tag{3.35}$$

where $M(s)$ and $N(s)$ are arbitrary functions of s. This form is extremely valuable in applying the inverse Laplace transform later in the calculations. Thus,

$$P(r,s) = \frac{M(s)}{r}\sinh(\sqrt{\frac{s}{\gamma}}r) + \frac{N(s)}{r}\cosh(\sqrt{\frac{s}{\gamma}}r). \tag{3.36}$$

Now, the Laplace transformed boundary conditions (3.31) are used to find $M(s)$ and $N(s)$. Equations (3.31) and (3.36) yield

$$F_1(s) = \frac{M(s)}{r_i}\sinh(\sqrt{\frac{s}{\gamma}}r_i) + \frac{N(s)}{r_i}\cosh(\sqrt{\frac{s}{\gamma}}r_i) \tag{3.37}$$

and

$$F_2(s) = \frac{M(s)}{r_o}\sinh(\sqrt{\frac{s}{\gamma}}r_o) + \frac{N(s)}{r_o}\cosh(\sqrt{\frac{s}{\gamma}}r_o). \tag{3.38}$$

Solving this linear system for $M(s)$ and $N(s)$, one obtains

$$M(s) = \frac{r_iF_1(s)\cosh(\sqrt{\frac{s}{\gamma}}r_o) - r_oF_2(s)\cosh(\sqrt{\frac{s}{\gamma}}r_i)}{\sinh(\sqrt{\frac{s}{\gamma}}(r_o - r_i))}. \tag{3.39}$$

and

$$N(s) = \frac{r_iF_1(s)\sinh(\sqrt{\frac{s}{\gamma}}r_o) - r_oF_2(s)\sinh(\sqrt{\frac{s}{\gamma}}r_i)}{\sinh(\sqrt{\frac{s}{\gamma}}(r_o - r_i))}. \tag{3.40}$$

The hyperbolic identity $\sinh(x-y) = \sinh(x)\cosh(y) - \cosh(x)\sinh(y)$ has been used several times to simplify $M(s)$ and $N(s)$, as well as the final result. Substituting equations (3.39) and (3.40) into (3.36) yields

$$P(r,s) = \frac{r_i F_1(s)\sinh(\sqrt{\frac{s}{\gamma}}(r_o - r)) + r_o F_2(s)\sinh(\sqrt{\frac{s}{\gamma}}(r - r_i))}{r\sinh(\sqrt{\frac{s}{\gamma}}(r_o - r_i))}. \tag{3.41}$$

Before the inverse Laplace transform can be applied to equation (3.41), $F_1(s)$ and $F_2(s)$ cannot be left as arbitrary functions of s. Thus, in light of De Leeuw (1965) sand drain problem, the boundary conditions $f_1(t)$ and $f_2(t)$ are assumed to be constants:

$$\begin{cases} f_1(t) = \alpha, \\ f_2(t) = \beta, \end{cases} \tag{3.42}$$

where $\alpha < \beta$. Their Laplace transforms are

$$\begin{cases} F_1(s) = \frac{\alpha}{s}, \\ F_2(s) = \frac{\beta}{s}. \end{cases} \tag{3.43}$$

Thus, the solution of the approximated case (3.41) reads

$$P(r,s) = \frac{r_i \alpha\sinh(\sqrt{\frac{s}{\gamma}}(r_o - r)) + r_o \beta\sinh(\sqrt{\frac{s}{\gamma}}(r - r_i))}{rs\sinh(\sqrt{\frac{s}{\gamma}}(r_o - r_i))}. \tag{3.44}$$

The inversion of the Laplace-transformed solution (3.44) is straightforward, and is reported, for completeness, in Appendix C. However, it is unlikely that such an inversion can be made in the test case problem formulated at the end of Section 3.1, namely the calculation of the pressure p when it is <u>not</u> assumed to be proportional to the dilatation e. Consequently, it is the above solution for $P(r,s)$ that is compared with its analogous expression in the second problem. This is clearly legitimate since - as it is well known - for continuous functions of at most exponential order the original function $p(r,t)$ is mapped *uniquely* into the transformed function $P(r,s)$ (D.V. Widder, Advanced Calculus, Chapter 13, Dover 1989). In short, the goodness of the approximation in question can be assessed in terms of the frequency domain as well as in the terms of the time domain.

3.3 Steps 2 and 3: Test case

In this Section, the general solution of the system of PDEs (3.22) and (3.23) from Section 3.1 is computed in order to get the general form of $e(\underline{r}, t)$ and $p(\underline{r}, t)$. Then, these quantities are

substituted into equation (3.26) which is solved for $\underline{u}(\underline{r},t)$ with the same boundary conditions as in Section 3.2. Note that the calculations and the final solution will be in modified spherical Bessel function form. This is primarily done for convenience, otherwise the expressions would be very long. However, one can take the modified spherical Bessel function form of the final solution and convert it into hyperbolic functions sinh and cosh, as done in Appendix D equation (D30).

To test the approximation made in Section 3.2, the same system of PDEs is considered:

$$\frac{\partial e(\underline{r},t)}{\partial t} = \frac{\kappa}{\eta}\nabla^2 p(\underline{r},t), \tag{3.45}$$

and

$$(2\mu+\lambda)\nabla^2 e(\underline{r},t) = \nabla^2 p(\underline{r},t). \tag{3.46}$$

The first equation is known as the storage equation in groundwater flow literature. The second equation is obtained by taking the divergence of the equation of motion

$$\mu\nabla^2\underline{u}(\underline{r},t) + (\mu+\lambda)\nabla e(\underline{r},t) = \nabla p(\underline{r},t), \tag{3.47}$$

and by using the relation $e = \nabla\cdot\underline{u}$.

The general solution to the above system is found in the following manner. Equation (3.46) is substituted into equation (3.45):

$$\frac{\partial e}{\partial t} = \gamma\nabla^2 e, \tag{3.48}$$

where $\gamma = \frac{\kappa}{\eta}(2\mu+\lambda)$. Since the domain of the problem is a homogeneous, radially symmetric hollow sphere, equation (3.48) is converted into spherical coordinates:

$$\frac{\partial e}{\partial t} = \gamma\left[\frac{1}{r^2}\frac{\partial}{\partial r}\left(r^2\frac{\partial e}{\partial r}\right)\right]. \tag{3.49}$$

Using the Laplace transform,

$$E(r,s) = \int_0^\infty e(r,t)\exp(-st)dt, \tag{3.50}$$

the PDE (3.49) is rewritten as:

$$sE(r,s) = \gamma\left[\frac{1}{r^2}\frac{d}{dr}\left(r^2\frac{dE(r,s)}{dr}\right)\right], \tag{3.51}$$

under the assumption that $e(r,0)=0$. Now, viewing s as a constant, the differential equation (3.51) is rearranged as

$$\frac{d^2E}{dr^2}+\frac{2}{r}\frac{dE}{dr}-\frac{s}{\gamma}E=0. \tag{3.52}$$

Recognizing that equation (3.52) is the same as to equation (3.30) in Section 3.2, the method used in solving equation (3.30) can be employed on equation (3.52) to arrive at the same general solution (3.39) in terms of hyperbolic functions sinh and cosh. However, unlike in Section 3.2, where the quantity being solved for was pressure $p(r,t)$, it is not possible to impose boundary conditions on the volume dilatation $e=\frac{\Delta V}{V}$, which is neither a force nor a stress quantity. This particular issue has been brought up in Chapter 2 and has been well known in groundwater flow studies as reviewed in Verruijt (1969). Thus, e is expressed in terms of the solid displacement vector $\underline{u}$, since the two are directly related via $e=\nabla\cdot\underline{u}$. Once this is accomplished, boundary conditions can be imposed on the system in terms of stress and strain which can be defined in terms of displacement u_r.

To avoid cumbersome calculations, it is convenient to apply the change of variable,

$$q=\sqrt{\frac{s}{\gamma}}r, \tag{3.53}$$

to equation (3.52) which results in the equation

$$\left(\frac{s}{\gamma}\right)\frac{d^2E}{dq^2}+\frac{2}{q}\sqrt{\frac{s}{\gamma}}\sqrt{\frac{s}{\gamma}}\frac{dE}{dq}-\frac{s}{\gamma}E=0, \tag{3.54}$$

or more simply

$$\frac{d^2E}{dq^2}+\frac{2}{q}\frac{dE}{dq}-E=0. \tag{3.55}$$

Equation (3.55) is identified as the modified spherical Bessel equation of order zero. The general solution is (Abramowitz and Stegun (1964), Chapter 10)

$$E(q,s)=\sqrt{\frac{\pi}{2q}}\left[A(s)I_{\frac{1}{2}}(q)+B(s)I_{-\frac{1}{2}}(q)\right], \tag{3.56}$$

where $A(s)$ and $B(s)$ are arbitrary constants of integration, and $\sqrt{\frac{\pi}{2q}}I_{\frac{1}{2}}(q)=\frac{\sinh(q)}{q}$ and $\sqrt{\frac{\pi}{2q}}I_{-\frac{1}{2}}(q)=\frac{\cosh(q)}{q}$ are the spherical Bessel functions.

Having a general solution for $E(q,s)$, the next step is to obtain a general solution for $P(q,s)$, which is the Laplace transformed pressure $p(r,t)$ together with the variable change

(3.53). As discussed in Appendix B, equation (3.46) is equivalent to

$$p(r,t) - (2\mu + \lambda)e(r,t) = g(t), \tag{3.57}$$

with $\nabla^2 g(t) = 0$. The Laplace transforms

$$P(r,s) = \int_0^\infty p(r,t)\exp(-st)dt \tag{3.58}$$

and

$$G(s) = \int_0^\infty g(t)\exp(-st)dt, \tag{3.59}$$

and the variable change (3.53) give

$$P(q,s) - (2\mu + \lambda)E(q,s) = G(s), \tag{3.60}$$

where $\nabla^2 G(s) = 0$. From equations (3.56) and (3.60), it follows that

$$P(q,s) = (2\mu + \lambda)\sqrt{\frac{\pi}{2q}}\left[A(s)I_{\frac{1}{2}}(q) + B(s)I_{-\frac{1}{2}}(q)\right] + G(s). \tag{3.61}$$

Equation (3.61) is used later in this calculation.

From the equation of motion (3.47), the Terzaghi stress tensor is obtained (see Appendix A). In the geometry of this model, it has only one non-zero component:

$$\tau_{rr}(r,t) = \lambda e + 2\mu e_{rr} = \lambda e + 2\mu\frac{\partial u_r}{\partial r}, \tag{3.62}$$

where e_{rr} is the strain component and $\underline{u} = (u_r, 0, 0)$ is the displacement in the r direction (due to the assumption of radial symmetry, the second and third components are set to zero). By means of the Laplace transform and the change of variable (3.53), equation (3.62) is written as

$$\tau_{rr}(q,s) = \lambda E(q,s) + 2\mu\frac{dU_r(q,s)}{dq}\sqrt{\frac{s}{\gamma}}. \tag{3.63}$$

This shows that the term $\frac{dU_r}{dq}$ needs to be found. Now, note that the volume dilatation e is defined as

$$e = e_{rr} + e_{\theta\theta} + e_{\phi\phi}, \tag{3.64}$$

where $e_{rr} = \frac{\partial u_r}{\partial r}$, $e_{\theta\theta} = \frac{u_r}{r}$, and $e_{\phi\phi} = \frac{u_r}{r}$ are displacement-strain components in the r, θ and ϕ directions for a sphere under the assumption of radial symmetry. The Laplace transformed equation (3.64) yields

$$E(r,s) = \frac{dU_r}{dr} + \frac{U_r}{r} + \frac{U_r}{r} = \frac{1}{r^2}\frac{d}{dr}(r^2 U_r), \tag{3.65}$$

and then under the variable change (3.53)

$$E(q,s) = \sqrt{\frac{s}{\gamma}} \frac{1}{q^2} \frac{d}{dq}(q^2 U_r). \tag{3.66}$$

Combining with equation (3.56), it follows that

$$\sqrt{\frac{s}{\gamma}} \frac{1}{q^2} \frac{d}{dq}(q^2 U_r) = \sqrt{\frac{\pi}{2q}} \left[A(s) I_{\frac{1}{2}}(q) + B(s) I_{-\frac{1}{2}}(q) \right]. \tag{3.67}$$

By integrating,

$$q^2 U_r = \sqrt{\frac{\gamma}{s}} \left[A(s) \underbrace{\int q^2 \sqrt{\frac{\pi}{2q}} I_{\frac{1}{2}}(q) dq}_{J_1} + B(s) \underbrace{\int q^2 \sqrt{\frac{\pi}{2q}} I_{-\frac{1}{2}}(q) dq}_{J_2} \right] + C(s), \tag{3.68}$$

where $C(s)$ is an arbitrary constant of integration. As is well known, the differentiation formulas for the spherical Bessel functions give:

$$\frac{d}{dq} \left[q^2 \sqrt{\frac{\pi}{2q}} I_{-\frac{3}{2}} \right] = q^2 \sqrt{\frac{\pi}{2q}} I_{-\frac{1}{2}}(q), \tag{3.69}$$

and

$$\frac{1}{q} \frac{d}{dq} \left[q^2 \sqrt{\frac{\pi}{2q}} I_{\frac{3}{2}} \right] = q \sqrt{\frac{\pi}{2q}} I_{\frac{1}{2}}(q), \tag{3.70}$$

(see Abramowitz and Stegun (1964), Formulas 10.2.22 and 10.2.23). These relations are useful in evaluating the integrals that appear in equation (3.68):

$$J_1 = \int q q \sqrt{\frac{\pi}{2q}} I_{\frac{1}{2}}(q) dq = \int q \frac{1}{q} \frac{d}{dq} \left[q^2 \sqrt{\frac{\pi}{2q}} I_{\frac{3}{2}} \right] dq = q^2 \sqrt{\frac{\pi}{2q}} I_{\frac{3}{2}}(q), \tag{3.71}$$

and

$$J_2 = \int q^2 \sqrt{\frac{\pi}{2q}} I_{-\frac{1}{2}}(q) dq = \int \frac{d}{dq} \left[q^2 \sqrt{\frac{\pi}{2q}} I_{-\frac{3}{2}} \right] dq = q^2 \sqrt{\frac{\pi}{2q}} I_{-\frac{3}{2}}(q). \tag{3.72}$$

Substituting equations (3.71) and (3.72) into (3.68) leads to

$$q^2 U_r = \sqrt{\frac{\gamma}{s}} \left[A(s) q^2 \sqrt{\frac{\pi}{2q}} I_{\frac{3}{2}}(q) + B(s) q^2 \sqrt{\frac{\pi}{2q}} I_{-\frac{3}{2}}(q) \right] + C(s), \tag{3.73}$$

which simplifies to

$$U_r = \sqrt{\frac{\gamma}{s}} \left[A(s) \sqrt{\frac{\pi}{2q}} I_{\frac{3}{2}}(q) + B(s) \sqrt{\frac{\pi}{2q}} I_{-\frac{3}{2}}(q) \right] + \frac{C(s)}{q^2}. \tag{3.74}$$

Given that U_r is found, $\frac{dU_r}{dq}$ is calculated to be

$$\begin{aligned}\frac{dU_r}{dq} &= \sqrt{\frac{\gamma}{s}}\left[A(s)\frac{d}{dq}\left(\sqrt{\frac{\pi}{2q}}I_{\frac{3}{2}}(q)\right) + B(s)\frac{d}{dq}\left(\sqrt{\frac{\pi}{2q}}I_{-\frac{3}{2}}(q)\right)\right] - 2\frac{C(s)}{q^3} \\ &= \sqrt{\frac{\gamma}{s}}\left[A(s)\sqrt{\frac{\pi}{2q}}\left(I_{\frac{1}{2}}(q) - \frac{2}{q}I_{\frac{3}{2}}(q)\right) + B(s)\sqrt{\frac{\pi}{2q}}\left(I_{-\frac{5}{2}}(q) + \frac{1}{q}I_{-\frac{3}{2}}(q)\right)\right] - 2\frac{C(s)}{q^3}.\end{aligned} \tag{3.75}$$

Furthermore, it is easy to show that

$$\frac{d}{dq}\left(\sqrt{\frac{\pi}{2q}}I_{\frac{3}{2}}(q)\right) = \sqrt{\frac{\pi}{2q}}I_{\frac{1}{2}}(q) - \frac{2}{q}\sqrt{\frac{\pi}{2q}}I_{\frac{3}{2}}(q), \tag{3.76}$$

and,

$$\frac{d}{dq}\left(\sqrt{\frac{\pi}{2q}}I_{-\frac{3}{2}}(q)\right) = \sqrt{\frac{\pi}{2q}}I_{-\frac{5}{2}}(q) + \frac{1}{q}\sqrt{\frac{\pi}{2q}}I_{-\frac{3}{2}}(q). \tag{3.77}$$

Consequently, equation (3.63) with the assistance of (3.56) takes on the form

$$\begin{aligned}\tau_{rr}(q,s) &= \lambda\sqrt{\frac{\pi}{2q}}\left[A(s)I_{\frac{1}{2}}(q) + B(s)I_{-\frac{1}{2}}(q)\right] \\ &\quad + 2\mu\sqrt{\frac{s}{\gamma}}\left(\sqrt{\frac{\gamma}{s}}\sqrt{\frac{\pi}{2q}}\left[A(s)\left(I_{\frac{1}{2}}(q) - \frac{2}{q}I_{\frac{3}{2}}(q)\right) + B(s)\left(I_{-\frac{5}{2}}(q) + \frac{1}{q}I_{-\frac{3}{2}}(q)\right)\right] - 2\frac{C(s)}{q^3}\right),\end{aligned} \tag{3.78}$$

or in simplified form

$$\begin{aligned}\tau_{rr}(q,s) &= \lambda\sqrt{\frac{\pi}{2q}}\left[A(s)I_{\frac{1}{2}}(q) + B(s)I_{-\frac{1}{2}}(q)\right] \\ &\quad + 2\mu\sqrt{\frac{\pi}{2q}}\left[A(s)\left(I_{\frac{1}{2}}(q) - \frac{2}{q}I_{\frac{3}{2}}(q)\right) + B(s)\left(I_{-\frac{5}{2}}(q) + \frac{1}{q}I_{-\frac{3}{2}}(q)\right)\right] - 4\mu\sqrt{\frac{s}{\gamma}}\frac{C(s)}{q^3}.\end{aligned} \tag{3.79}$$

For the comparison to the solution (3.44) of the approximated case in Section 3.2, the pressure needs to be computed. It is given by equation (3.61); however, the values of the arbitrary constants of integration $A(s)$, $B(s)$ and $G(s)$ need to be found, which requires the application of boundary conditions. For obvious reasons these boundary conditions need to be the same as in Section 3.2. Thus,

$$\begin{cases} p(r_i,t) = \alpha, \\ \\ p(r_o,t) = \beta, \end{cases} \tag{3.80}$$

where α and β, with $\alpha < \beta$, correspond to the pressure at the inner radius r_i and the outer radius r_o. Transforming equation (3.80) using the Laplace transform and applying the variable change (3.53), it follows that

$$\begin{cases} P(q_i, s) = \frac{\alpha}{s}, \\ \\ P(q_o, s) = \frac{\beta}{s}, \end{cases} \tag{3.81}$$

where $q_i = \sqrt{\frac{s}{\gamma}} r_i$ and $q_o = \sqrt{\frac{s}{\gamma}} r_o$. However, these two conditions allow for computing only two of the three constants. The next set of boundary conditions are imposed on the Terzaghi stress tensor τ_{ij}:

$$T_{ij} = -p\delta_{ij} + \tau_{ij}, \tag{3.82}$$

where T_{ij} is the total stress tensor and δ_{ij} is the Kronecker delta function. By means of the Laplace transform and variable change (3.55) and the assumption of radial symmetry, conditions read

$$\begin{cases} \tau_{rr}(q_i, t) = 0, \\ \\ \tau_{rr}(q_o, t) = 0. \end{cases} \tag{3.83}$$

Now, using the boundary conditions (3.81) and (3.83) in equations (3.61) and (3.79), four equations with four unknowns, $A(s)$, $B(s)$, $G(s)$, and $C(s)$ are obtained:

$$\frac{\alpha}{s} = (2\mu + \lambda)\sqrt{\frac{\pi}{2q_i}} \left[A(s) I_{\frac{1}{2}}(q_i) + B(s) I_{-\frac{1}{2}}(q_i) \right] + G(s); \tag{3.84}$$

$$\frac{\beta}{s} = (2\mu + \lambda)\sqrt{\frac{\pi}{2q_o}} \left[A(s) I_{\frac{1}{2}}(q_o) + B(s) I_{-\frac{1}{2}}(q_o) \right] + G(s); \tag{3.85}$$

$$\begin{aligned} 0 = {} & \lambda\sqrt{\frac{\pi}{2q_i}} \left[A(s) I_{\frac{1}{2}}(q_i) + B(s) I_{-\frac{1}{2}}(q_i) \right] \\ & + 2\mu\sqrt{\frac{\pi}{2q_i}} \left[A(s) \left(I_{\frac{1}{2}}(q_i) - \frac{2}{q_i} I_{\frac{3}{2}}(q_i) \right) + B(s) \left(I_{-\frac{5}{2}}(q_i) + \frac{1}{q_i} I_{-\frac{3}{2}}(q_i) \right) \right] \\ & - 4\mu\sqrt{\frac{s}{\gamma}} \frac{C(s)}{{q_i}^3}; \end{aligned} \tag{3.86}$$

$$
\begin{aligned}
0 &= \lambda\sqrt{\frac{\pi}{2q_o}}\left[A(s)I_{\frac{1}{2}}(q_o) + B(s)I_{-\frac{1}{2}}(q_o)\right] \\
&+ 2\mu\sqrt{\frac{\pi}{2q_o}}\left[A(s)\left(I_{\frac{1}{2}}(q_o) - \frac{2}{q_o}I_{\frac{3}{2}}(q_o)\right) + B(s)\left(I_{-\frac{5}{2}}(q_o) + \frac{1}{q_o}I_{-\frac{3}{2}}(q_o)\right)\right] \\
&- 4\mu\sqrt{\frac{s}{\gamma}}\frac{C(s)}{{q_o}^3}.
\end{aligned}
\tag{3.87}
$$

In Appendix D, the values for $A(s)$, $B(s)$ and $G(s)$ are found ($C(s)$ is not needed).

Once the smoke clears in Appendix D, equation (3.61) becomes

$$
P(q,s) = (2\mu+\lambda)\sqrt{\frac{\pi}{2q}}\left[\frac{\overline{A}(s)}{s}I_{\frac{1}{2}}(q) + \frac{\overline{B}(s)}{s}I_{-\frac{1}{2}}(q)\right] + \frac{\overline{G}(s)}{s}, \tag{3.88}
$$

where the over-barred quantities are defined in Appendix D (Equations D21-D23). Returning back to r via relation (3.53), the solution for the test case is

$$
P(r,s) = (2\mu+\lambda)\sqrt{\frac{\pi}{2r}\sqrt{\frac{\gamma}{s}}}\left[\frac{\overline{A}(s)}{s}I_{\frac{1}{2}}(r\sqrt{\frac{s}{\gamma}}) + \frac{\overline{B}(s)}{s}I_{-\frac{1}{2}}(r\sqrt{\frac{s}{\gamma}})\right] + \frac{\overline{G}(s)}{s}. \tag{3.89}
$$

As anticipated at the end of Section 3.2, the inversion of the Laplace transformed pressure (3.89) is far from trivial; however, it is not necessary, as explained earlier. It is possible to work directly with the pressure expressed in the frequency domain.

3.4 Step 4: Comparison

In this Section, the Laplace transformed expressions are compared for both the approximated case and the test case.

3.4.1 Parameters

Three different hollow spheres which are considered are shown in Table 3.1.

Sphere	Inner radius r_i (cm)	Outer radius r_o (cm)	Location r (cm)
1	0.2	0.5	0.35
2	0.5	1	0.75
3	5	10	7.5

Table 3.1: Hollow sphere radii values

Hollow spheres 1 and 2 are close to the size of a tumor, as reported in literature (Jain and Baxter, 1988; Jain et al., 2007; Lunt et al., 2008). Hollow sphere 3 is more relevant for the study of ground water flow, where the size of an aquifer can range from centimeters to meters (Verruijt, 1970; Bear and Verruijt, 1987). To study the pressure behavior for each hollow sphere, a location r is selected halfway between the inner radius r_i and the outer radius r_o. At locations near the inner and the outer radii, the pressure is dominated by the boundary conditions, and is therefore not considered.

The value of the parameter $\gamma = \frac{\kappa}{\eta}(2\mu + \lambda)$ is based on the following values. Since $\frac{\kappa}{\eta}$ is the hydraulic conductivity K, it is assigned the value of 2.5×10^{-7} cm^2 second^{-1} mmHg^{-1} (Jain et al., 2007) as in Chapter 2, for consistency. The Lamé elastic parameters μ and λ take on the values for soft saturated clay from Chapter 2, that is, 3.6×10^4 mmHg and 1.5×10^5 mmHg (Bowles, 1988), respectively. Thus, the value of γ is approximately 0.06 mmHg.

The boundary conditions are selected to be $\alpha = 5$ mmHg for the inner radius and $\beta = 30$ mmHg for the outer radius. These values are reasonable for biological tissue and are selected to test the approximated case against the test case.

3.4.2 Results

Here, the Laplace transformed solutions for the approximated case,

$$P(r,s) = \frac{r_i \alpha \sinh(\sqrt{\frac{s}{\gamma}}(r_o - r)) + r_o \beta \sinh(\sqrt{\frac{s}{\gamma}}(r - r_i))}{rs \sinh(\sqrt{\frac{s}{\gamma}}(r_o - r_i))}, \tag{3.90}$$

and for the test case,

$$P(r,s) = (2\mu+\lambda)\sqrt{\frac{\pi}{2r}\sqrt{\frac{\gamma}{s}}}\left[\frac{\overline{A}(s)}{s}I_{\frac{1}{2}}(r\sqrt{\frac{s}{\gamma}}) + \frac{\overline{B}(s)}{s}I_{-\frac{1}{2}}(r\sqrt{\frac{s}{\gamma}})\right] + \frac{\overline{G}(s)}{s}, \qquad (3.91)$$

are simulated. Note that equation (3.91) is written in modified spherical Bessel form for convenience and can be converted into hyperbolic functions sinh and cosh as in Appendix D, equation (D30).

Figure 3.3, Figure 3.4 and Figure 3.5 clearly show that there is a significant enough difference between the two solutions. In fact, as the inner and the outer radii increase, the pressure difference between the approximated case and the test case grows larger. This pressure difference cannot be ascribed to the boundary conditions, as their effects become less prominent at the location halfway between the two radii.

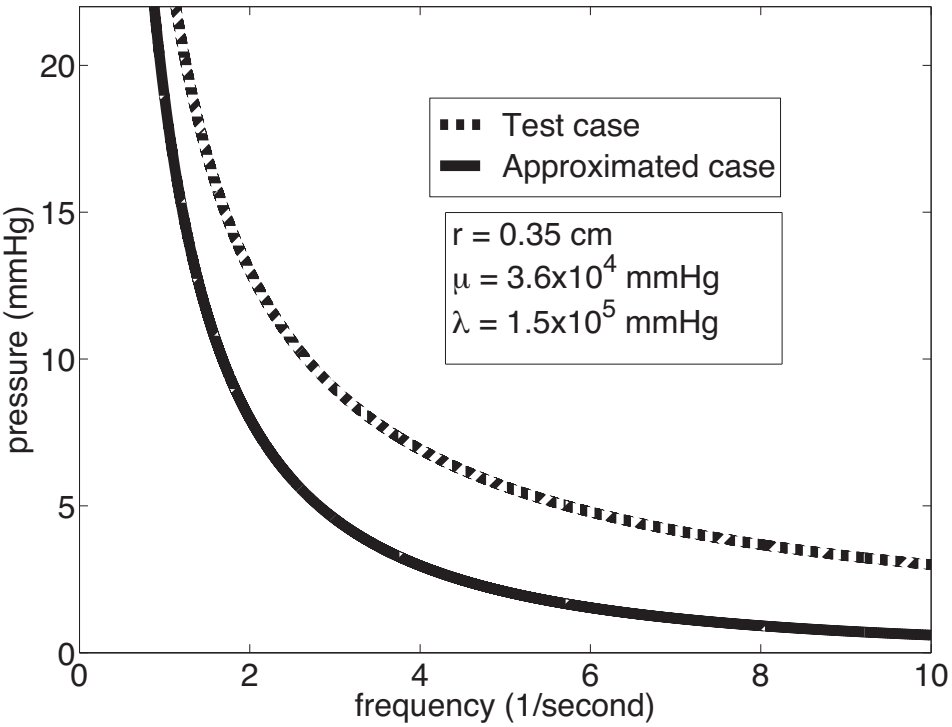

Figure 3.3: Pressure profile for soft saturated clay with the inner and outer radii of 0.2 cm and 0.5 cm

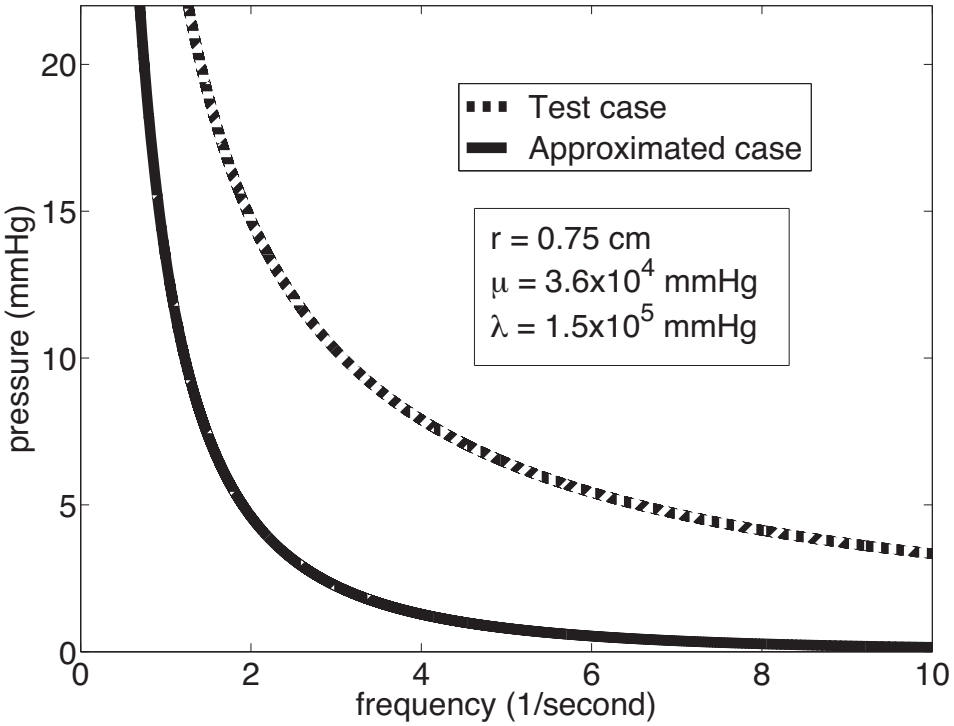

Figure 3.4: Pressure profile for soft saturated clay with the inner and outer radii of 0.5 cm and 1 cm

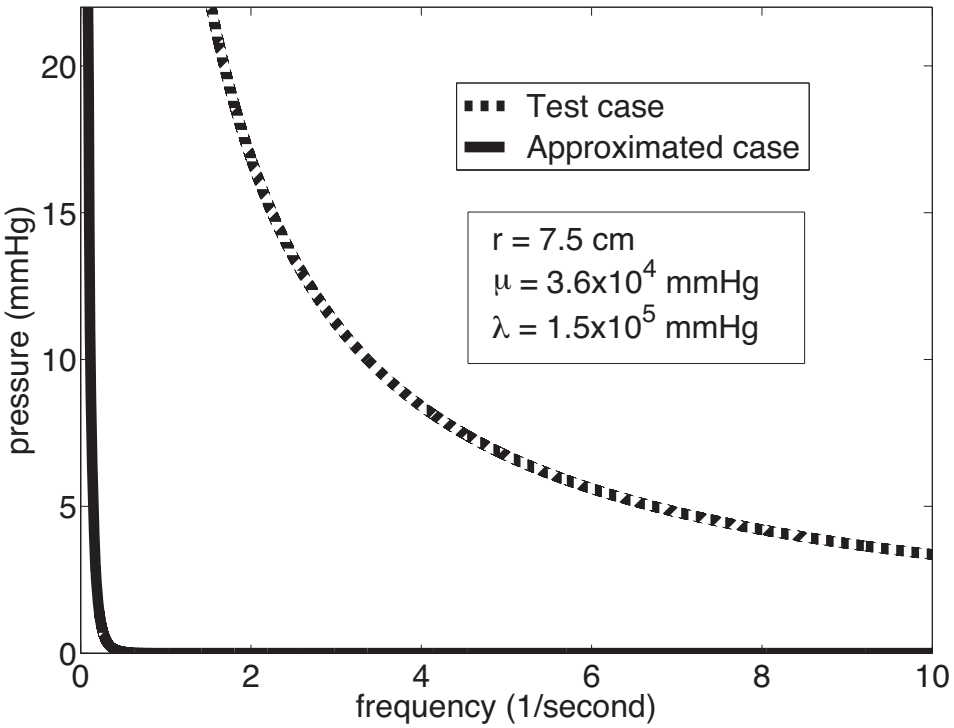

Figure 3.5: Pressure profile for soft saturated clay with the inner and outer radii of 5 cm and 10 cm

Varying the Lamé elastic parameters μ and λ, using the three hollow sphere sizes specified in Table 3.1, also shows a significant enough pressure difference between the approximated case and the test case solutions. Figure 3.6, Figure 3.7 and Figure 3.8 show the behavior of the pressure with very soft saturated clay having the Lamé parameter values of $\mu = 7.5 \times 10^3$ mmHg and $\lambda = 3.0 \times 10^4$ mmHg (Bowles, 1988). Figure 3.9, Figure 3.10 and Figure 3.11 illustrate the effects of the elastic parameter values for medium saturated clay, in which case $\mu = 6.8 \times 10^4$ mmHg and $\lambda = 2.7 \times 10^5$ mmHg (Bowles, 1988). As the values of μ and λ increase, the pressure difference becomes far smaller between the approximated case and the test case.

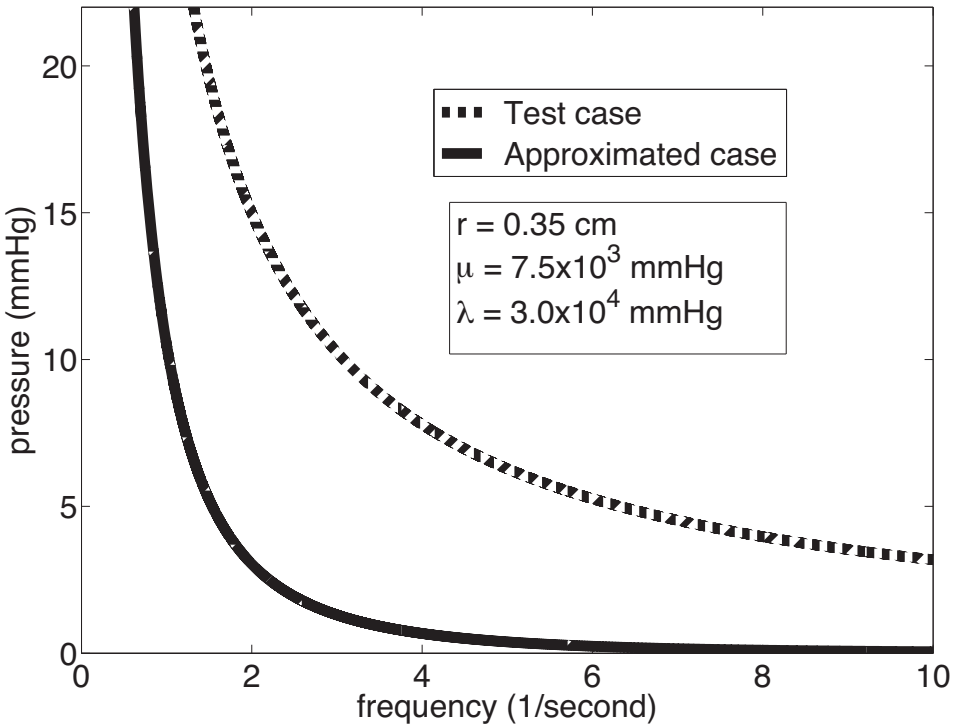

Figure 3.6: Pressure profile for very soft saturated clay with the inner and outer radii of 0.2 cm and 0.5 cm

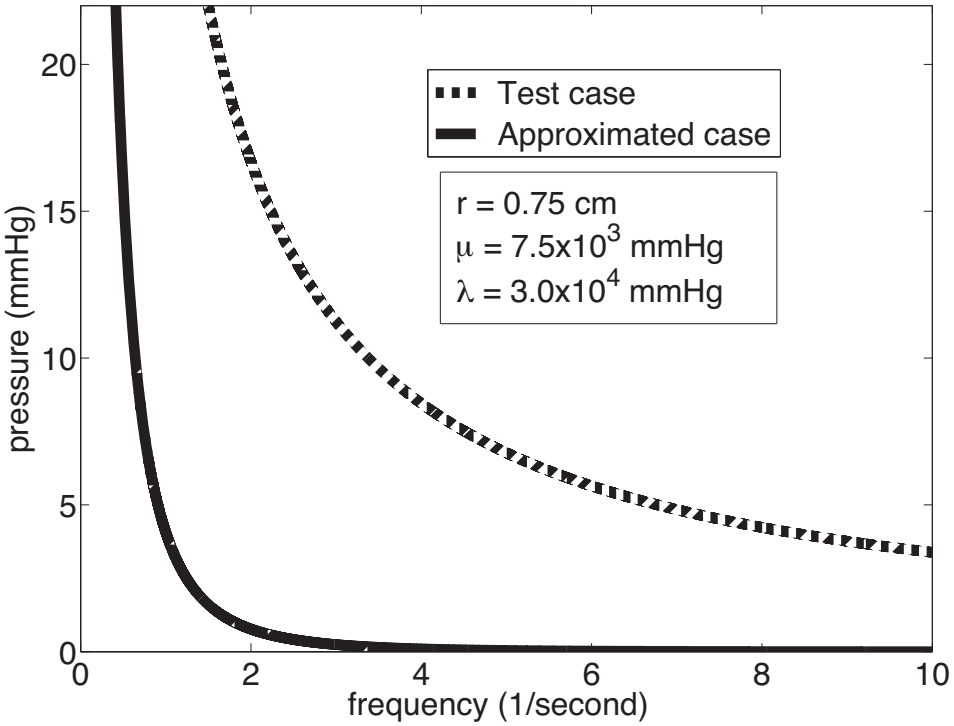

Figure 3.7: Pressure profile for very soft saturated clay with the inner and outer radii of 0.5 cm and 1 cm

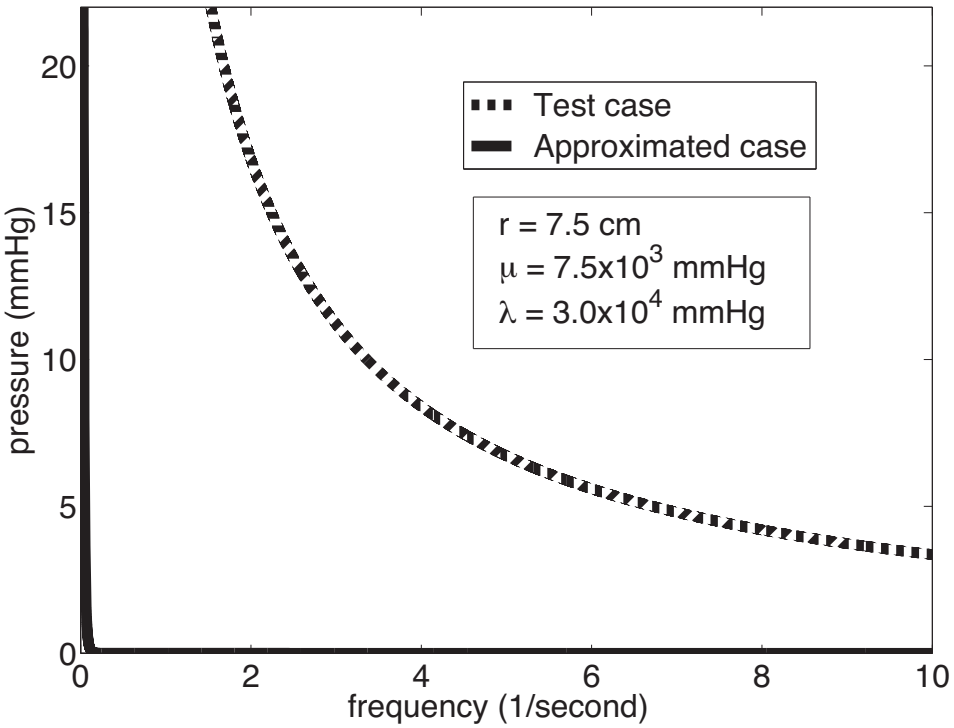

Figure 3.8: Pressure profile for very soft saturated clay with the inner and outer radii of 5 cm and 10 cm

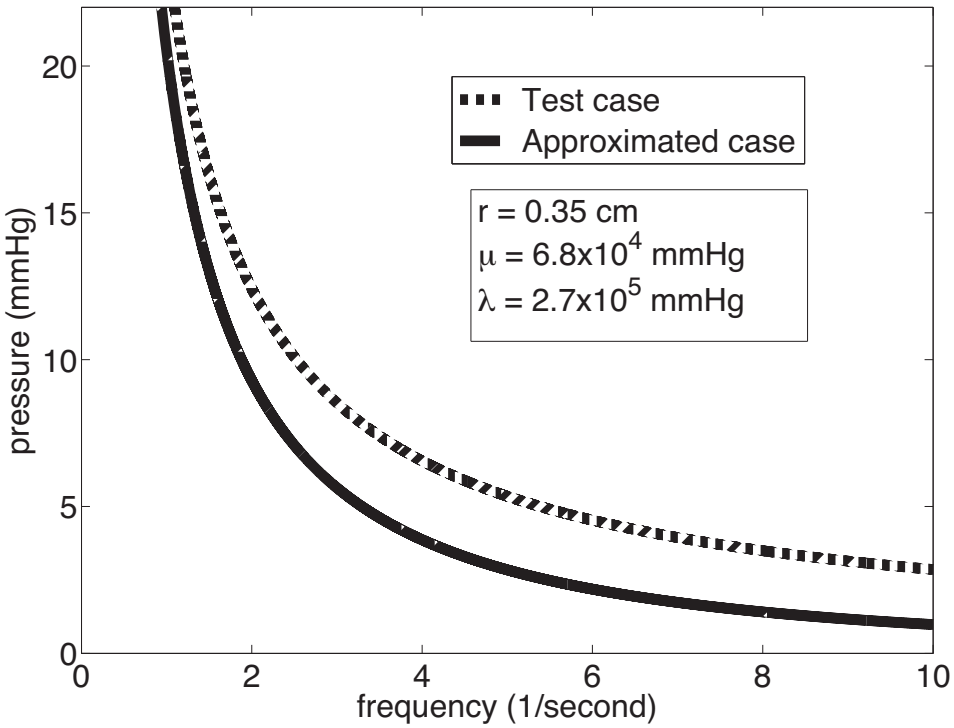

Figure 3.9: Transient state profile for medium saturated clay with the inner and outer radii of 0.2 cm and 0.5 cm

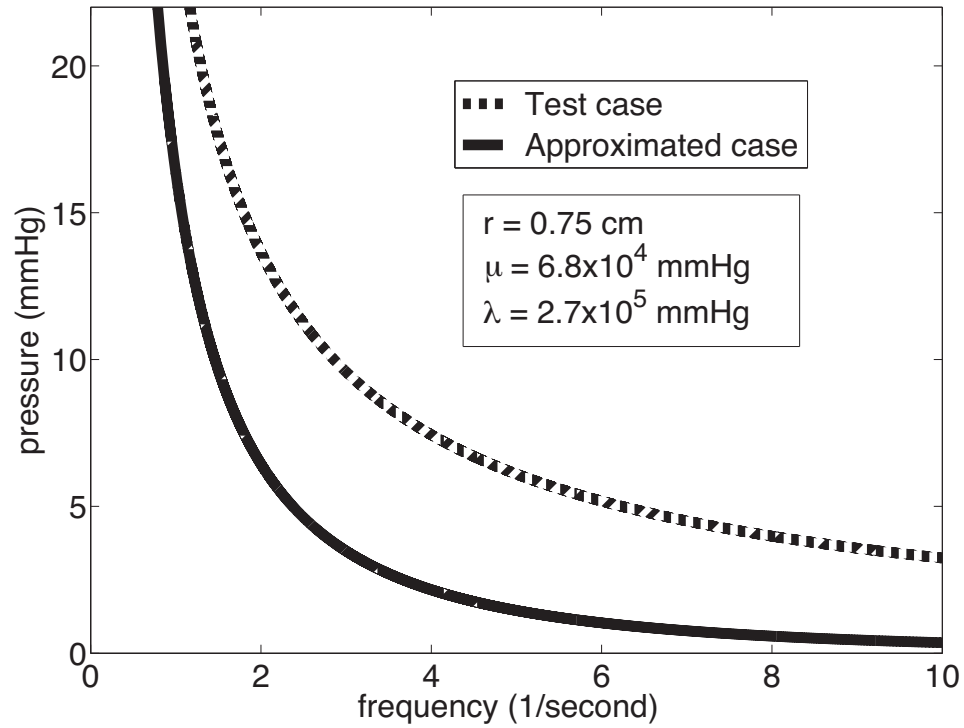

Figure 3.10: Transient state profile for medium saturated clay with the inner and outer radii of 0.5 cm and 1 cm

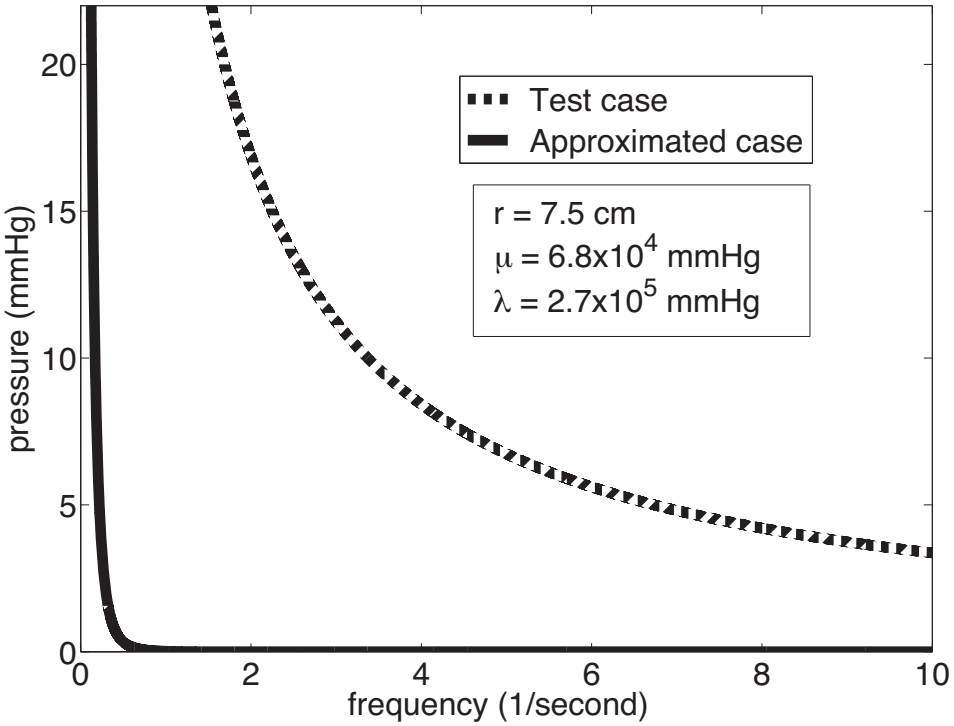

Figure 3.11: Transient state profile for medium saturated clay with the inner and outer radii of 5 cm and 10 cm

Since the model discussed in Chapter 3 is a heat-type equation solved for both the approximated case and the test case – in particular, analyzing the proportionality of the tissue dilatation e and the IFP p – a possible theme for future investigation would be to incorporate the effect of a source or a sink term in the PDE (3.22) coupled with (3.23). The inclusion of a source or a sink might decrease the pressure difference between the approximated case and the test case, and the results can be compared with the work done in Chapter 2, where the fundamental PDE has a fluid source term. However, as seen in the calculations for the test case in Section 3.3, the addition of a source or a sink term might significantly increase the complexity of the calculations.

Lastly, the Lamé parameter values are crucial for this model in order to study the tumor IFP phenomena. For example, using the medium saturated clay is not realistic for tumors, since the texture of clay is too hard in comparison to tumor tissue; however, it may be more beneficial in the study of ground water flow. Thus, in order for this model to be relevant for tumors, appropriate Lamé parameter values for the solid constituent of tumor tissue are needed.

Chapter 4

Examining the behavior of normal pressure hydrocephalus

4.1 Review of the work done by Levine (1999)

As explained in Chapter 1, this Chapter is concerned with another application of mixture theory, namely the pathogenesis of normal pressure hydrocephalus. Before doing so, and for completeness, the theoretical analysis of D. N. Levine (1999) is reviewed in some detail using his own notation.

Levine (1999) focuses on explaining the pathogenesis of normal pressure hydrocephalus through exploring the role of the brain parenchyma in absorbing cerebrospinal fluid (CSF). The governing equations are the same as those of consolidation theory (Biot, 1941), with the addition of Starling's law to account for the absorption of CSF. From these equations, the radial expressions for the steady state pressure and displacement distribution are derived explicitly along with other mechanical parameters such as stress and strain.

Geometrically, the brain parenchyma is represented as a radially symmetric spherical shell with a concentrically CSF-filled spherical cavity representing the lateral and third ventricles. The subarachnoid space at the outer edge of the parenchyma is treated as a thin CSF-filled shell. Levine assumes that the parenchyma consists of a solid matrix permeated by two networks of fluid-filled channels: the first consists of the parenchymal interstitial fluid; the second consists of the blood in the cerebral vessels, most of which is in the capillaries and the veins (Levine, 1999, pages 880-881). Both the solid matrix and the fluids are intrinsically incompressible. At the macroscopic level, the tissue is assumed to be homogeneous and isotropic. All pressures are measured relative to the cerebral venous pressure.

4.1.1 Radial steady state pressure distribution of parenchymal tissue

Within the brain parenchyma, two laws govern the transport process:

(1) Darcy's law represents the fluid flow through the parenchyma in proportion to, and in the opposite direction to the pressure gradient; thus

$$V_r(r) = -k' \frac{\partial P}{\partial r}, \tag{4.1}$$

where r is the radial distance, $V_r(r)$ is the radial change in the volume flow across a unit area per unit time, k' is the coefficient of parenchymal hydraulic conductivity, and P is the incremental interstitial fluid pressure, also referred to as the pore pressure.

(2) Starling's law describes the transcapillary exchange of interstitial fluid and blood plasma:

$$V_{ab} = \hat{k} P, \tag{4.2}$$

where V_{ab} represents the amount of fluid absorbed into the blood per unit volume of parenchyma per unit time, and $\hat{k}$ is the coefficient of parenchymal absorption.

To determine the steady state radial distribution of the incremental interstitial fluid pressure, the conservation of mass equation is formulated as:

$$\frac{\partial \xi}{\partial t} = k' \left(\frac{\partial^2 P}{\partial r^2} + \frac{2}{r} \frac{\partial P}{\partial r} \right) - \hat{k} P, \tag{4.3}$$

where ξ is the change of fluid content per unit volume of tissue and t is time. Equation (4.3) represents the total flow of interstitial fluid from a given volume of brain parenchyma. The inflow is the negative of the divergence of the flow vector centered at a point at radius r:

$$- \left(\frac{\partial V_r(r)}{\partial r} + \frac{2 V_r(r)}{r} \right). \tag{4.4}$$

Equation (4.4) is thought of as the amount of interstitial fluid entering across the boundary walls of a small volume of tissue. Substituting Darcy's law (4.1) into (4.4) yields the first term on the right hand side of (4.3). The outflow is obtained by using Starling's law (4.2).

At steady state, the left hand side of equation (4.3) is set to zero, which makes the change in fluid content time independent, and therefore, the pressure is given by the modified Bessel's equation

$$\frac{d^2 P}{dr^2} + \frac{2}{r} \frac{dP}{dr} = \frac{P}{k}, \tag{4.5}$$

where $k = \frac{k'}{\hat{k}}$. The general solution of the differential equation (4.5) is

$$P(r) = \frac{A_1}{r} \sinh\left(\frac{r}{\sqrt{k}}\right) + \frac{A_2}{r} \cosh\left(\frac{r}{\sqrt{k}}\right), \tag{4.6}$$

where A_1 and A_2 are constants determined by boundary conditions.

Two different sets of boundary conditions are used to obtain the steady state fluid pressure. The first set of boundary conditions is

$$\begin{cases} P = P_v, \text{ at } r = r_i, \\ \\ P = 0, \text{ at } r = r_o, \end{cases} \tag{4.7}$$

where P_v is the small increment of ventricular CSF pressure, r_i and r_o are the radii of the boundaries separating the ventricles and the parenchyma, and the parenchyma and the subarachnoid space, respectively. Applying boundary conditions (4.7) to (4.6) yields the first pressure solution

$$P(r) = \frac{P_v r_i \sinh\left(\frac{r_o - r}{\sqrt{k}}\right)}{r \sinh\left(\frac{r_o - r_i}{\sqrt{k}}\right)}. \tag{4.8}$$

The second set of boundary conditions prescribes the rate of entry of CSF into the brain parenchyma, denoted as ψ. This determines a radial velocity of CSF flow at the ventricular wall which is equal to $\frac{\psi}{4\pi r_i^2}$. By means of Darcy's law (4.1), the boundary condition at the ventricle wall is

$$\frac{dP}{dr} = -\frac{\psi}{4\pi r_i^2 k'}, \quad \text{at } r = r_i, \tag{4.9}$$

and at the outer edge of the parenchyma,

$$P = 0, \quad \text{at } r = r_o. \tag{4.10}$$

Substituting the boundary conditions (4.9) and (4.10) into equation (4.6), this second pressure solution reads

$$P(r) = \frac{\psi\sqrt{k} \sinh\left(\frac{r_o - r}{\sqrt{k}}\right)}{4\pi r k' \left[r_i \cosh\left(\frac{r_o - r_i}{\sqrt{k}}\right) + \sqrt{k} \sinh\left(\frac{r_o - r_i}{\sqrt{k}}\right)\right]}. \tag{4.11}$$

Evaluating equation (4.11) at $r = r_i$ gives the value of P_v that is needed for CSF to enter the parenchyma and to be absorbed at the rate ψ.

Finally, under the 'Seepage, Efficient Parenchymal Absorption' (SEPA) hypothesis, the parameter k is assumed to be small relative to $(r_o - r)^2$. Using the approximations

$\cosh\left(\frac{x}{\sqrt{k}}\right) \approx \frac{1}{2}e^{\frac{x}{\sqrt{k}}} \approx \sinh\left(\frac{x}{\sqrt{k}}\right) \approx \frac{1}{2}e^{\frac{x}{\sqrt{k}}}$, which hold for $\frac{x}{\sqrt{k}}$ large, the sinh and cosh terms are replaced by the exponential functions. (Here, it is assumed that the points r are not too close to the outer edge r_o of the brain parenchyma.) With this approximation, the first pressure solution (4.8) reduces to:

$$P(r) = \frac{P_v r_i}{r} e^{-\frac{r-r_i}{\sqrt{k}}}. \tag{4.12}$$

Now, the size of P_v needs to be calculated. Using equation (4.11) with the approximation for small k, the second pressure solution (4.11) reduces to

$$P_v = \frac{\psi\sqrt{k}}{4\pi r_i^2 k'}, \tag{4.13}$$

which represents the value of P_v for parenchymal absorption at the rate ψ.

4.1.2 Radial steady state displacement distribution of parenchymal tissue

To determine the radial displacement of the parenchymal tissue caused by an increment of P_v, Levine formulated the equations for the volume of parenchyma in the following manner. As a result of displacement, each volume element of the parenchyma undergoes strain which is a fractional change of length. Under radial symmetry, only the radial components $e_r(r)$ and tangential components $e_\theta(r)$ are needed; they are defined as:

$$e_r(r) = \frac{\partial u_r(r)}{\partial r}, \tag{4.14}$$

$$e_\theta(r) = \frac{u_r(r)}{r}. \tag{4.15}$$

Using the radial strain defined above, the fractional change in volume, also referred to as the volume strain, of the parenchyma $e(r)$ is derived as:

$$e = e_r + 2e_\theta = \frac{\partial u_r}{\partial r} + 2\frac{u_r}{r}. \tag{4.16}$$

Next, the expanded Hooke's law (Biot, 1941) is employed. This law states that the components of strain, e_r and e_θ, and the change in fluid content per unit volume of parenchyma ξ are linearly related to the components of stress and to the change in fluid pressure P:

$$e_r = \frac{\sigma_r}{E} - \frac{\nu}{E}(\sigma_\theta + \sigma_\phi) + \frac{P}{3H}, \tag{4.17}$$

$$e_\theta = \frac{\sigma_\theta}{E} - \frac{\nu}{E}(\sigma_r + \sigma_\phi) + \frac{P}{3H}, \tag{4.18}$$

$$\xi = \frac{\sigma_r + \sigma_\theta + \sigma_\phi}{E} + \frac{P}{R}, \tag{4.19}$$

where E is Young's modulus, H is the energy of strain, ν is the Poisson ratio, and R is the ratio of change in pore pressure to change in fluid content in the absence of stresses. At each point of the parenchyma, determined using the stress radial component $\sigma_r(r)$, tangential component $\sigma_\theta(r)$, and axial component $\sigma_\phi(r)$. Now, solving the equations (4.17), (4.18) and (4.19) of the expanded Hooke's law for incremental stresses and change in interstitial fluid content in terms of strains and change in pore pressure yields:

$$\sigma_r = 2Ge_r + \frac{2G\nu}{1-2\nu}e - \alpha P, \tag{4.20}$$

$$\sigma_\theta = -Ge_r + \frac{G}{1-2\nu}e - \alpha P, \tag{4.21}$$

$$\xi = \alpha e + \frac{P}{M}, \tag{4.22}$$

where G is the shear modulus, and α represents the ratio of change in fluid content to change in parenchymal volume when pore pressure in equation (4.22) does not change ($P = 0$). The expression $\frac{1}{M}$ is derived to be a type of capacitance, that is, the amount of interstitial fluid that can be forced into an unchanging volume of parenchyma ($e = 0$) per unit increase in pore pressure. It should be stressed here that although these are the equations derived by Biot (1941), the assumption made there was that the system was unsaturated. This important point is discussed in Chapter 5.

Now, if the acceleration of the tissue and the body forces such as gravitation are neglected, then the equation of equilibrium says that as the sum of the forces acting on the boundaries of the volume is zero:

$$\frac{\partial \sigma_r}{\partial r} + \frac{2}{r}(\sigma_r - \sigma_\theta) = 0. \tag{4.23}$$

Then, the equation for the radial tissue displacements caused by P_v is determined by substituting equations (4.20) and (4.21) into (4.23) using the relation (4.16):

$$\frac{\partial^2 u_r}{\partial r^2} + \frac{2}{r}\frac{\partial u_r}{\partial r} - \frac{2u_r}{r^2} = \frac{(1-2\nu)\alpha}{2G(1-\nu)}\frac{\partial P}{\partial r}. \tag{4.24}$$

The term $\frac{\partial P}{\partial r}$, obtained by differentiating equation (4.8), is employed to solve the differential equation (4.24). The general solution of the differential equation (4.24) is

$$u_r(r) = -\frac{(1-2\nu)\alpha P_v r_i k}{2G(1-\nu)\sinh\left(\frac{r_o-r_i}{\sqrt{k}}\right)}\left[\frac{\sqrt{k}\cosh\left(\frac{r_o-r}{\sqrt{k}}\right)}{r} + \frac{k\sinh\left(\frac{r_o-r}{\sqrt{k}}\right)}{r^2}\right] + \frac{C_1}{r^2} + C_2 r \tag{4.25}$$

The constants C_1 and C_2 are determined from the boundary conditions.

At the inner edge of the brain parenchyma, the compressive radial stress P_v acts on the ventricular wall. Using equation (4.20) with (4.14) and (4.15), the boundary condition imposed is

$$-P_v = 2G\frac{\partial u_r}{\partial r} + \frac{2G\nu}{1-2\nu}\left(\frac{\partial u_r}{\partial r} + 2\frac{u_r}{r}\right), \quad \text{at } r = r_i. \tag{4.26}$$

At the outer surface, the brain parenchyma is prevented from any significant radial expansion by a rigid skull, and thus,

$$u_r(r) = 0, \quad \text{at } r = r_o. \tag{4.27}$$

Substituting the boundary conditions (4.26) and (4.27) into the general solution (4.27), C_1 and C_2 are computed:

$$C_1 = \frac{P_v r_o^3}{2G\left[\Gamma^3 + \frac{1+\nu}{2(1-2\nu)}\right]}\left(\frac{1}{2} + \frac{(1-2\nu)\alpha\sqrt{k}}{1-\nu}\left[\frac{\cosh\left(\frac{r_o-r_i}{\sqrt{k}}\right) + \frac{1+\nu}{2(1-2\nu)\Gamma^2}}{r_i\sinh\left(\frac{r_o-r_i}{\sqrt{k}}\right)} + \frac{\sqrt{k}}{r_i^2}\right]\right), \tag{4.28}$$

and

$$C_2 = -\frac{P_v r_o^3}{2G\left[\Gamma^3 + \frac{1+\nu}{2(1-2\nu)}\right]}\left(\frac{1}{2} + \frac{(1-2\nu)\alpha\sqrt{k}}{1-\nu}\left[\frac{\cosh\left(\frac{r_o-r_i}{\sqrt{k}}\right) - \Gamma}{r_i\sinh\left(\frac{r_o-r_i}{\sqrt{k}}\right)} + \frac{\sqrt{k}}{r_i^2}\right]\right), \tag{4.29}$$

where $\Gamma = \frac{r_o}{r_i}$. Substituting C_1 from (4.28) and C_2 from (4.29) into the general solution (4.25) yields the radial displacement of the parenchyma tissue at steady state.

Under the SEPA hypothesis, the displacement of the ventricular wall can be found by substituting $r = r_i$ into the general solution for the displacement distribution (4.25), along with (4.28) and (4.29), and by simplifying the expression using the approximations of the hyperbolic terms for small k, with the following result:

$$u_r(r_i) = \frac{P_v r_i}{2G}\left(\frac{(1-2\nu)(\Gamma^3-1) - \frac{3(1-2\nu)\alpha\sqrt{k}}{ri}}{2(1-2\nu)\Gamma^3 + 1 + \nu}\right). \tag{4.30}$$

4.2 Radial steady state pressure and displacement distribution in normal pressure hydrocephalus according to mixture theory

The geometry is kept the same as in Levine (1999), and in light of the assumptions necessary in mixture theory (see Appendix A for the formulation of mixture theory), the brain parenchyma is treated as a homogenized medium, such that at every point the solid and the fluid phases coexist simultaneously. Both the solid and the fluid phases are incompressible, and the biphasic material is completely saturated.

Further assumptions are made on the transport process within the brain. The transcapillary exchange of the fluid in the homogeneous tissue is given by Starling's law:

$$\Omega(r,t) = -\frac{L_p S}{V}(p(r,t) - p_v), \tag{4.38}$$

where spatial and temporal coordinates are denoted as r (in cm) and t (in second) respectively, and $\Omega(r,t)$ is the net fluid movement. L_p is the permeability of the capillary wall (with units cm second^{-1} mmHg^{-1}), $\frac{S}{V}$ is the vascular surface area per unit tissue volume (with units cm^{-1}), p is the interstitial fluid pressure (IFP) (with units mmHg), and p_v is the venous pressure (with units mmHg). As in Chapter 2, the osmotic pressure term in Starling's law has been dropped as done by Levine (1999). Now, since the CSF absorption occurs through the bloodstream, the surrounding pressure is assumed to be greater than the venous pressure.

Lastly, the motion of fluid relative to the solid in the interstitium of the brain is described by a generalized form of Darcy's law:

$$\phi\left(\underline{v}(r,t) - \frac{\partial \underline{u}(r,t)}{\partial t}\right) = -K\nabla p(r,t), \tag{4.39}$$

where ϕ is the dimensionless volumetric fraction of the fluid defined as the change in fluid volume per unit volume of the tissue, $\underline{v}$ is the fluid velocity (with units cm second^{-1}), and $\underline{u}$ is the solid displacement vector represented (in cm).

4.2.1 Radial steady state pressure

Using the appropriate field equations for the conservation of mass and the conservation of linear momentum for each phase under the above governing assumptions, the fundamental partial differential equation of the entire mixture obtained is

$$\frac{\partial e(r,t)}{\partial t} - K\nabla^2 p(r,t) = \Omega(r,t), \tag{4.40}$$

where $e = \nabla \cdot \underline{u}$ is the tissue dilatation being the change of volume per unit volume of tissue and K is the hydraulic conductivity (with units cm^2 second^{-1} mmHg^{-1}). Since the steady state IFP is needed, the PDE (4.40) becomes:

$$-K\nabla^2 p(r) = -L_p \frac{S}{V}(p(r) - p_v). \tag{4.41}$$

In spherical coordinates, equation (4.41) becomes

$$\frac{d^2p(r)}{dr^2} + \frac{2}{r}\frac{dp(r)}{dr} - A^2 p(r) = -A^2 p_v, \tag{4.42}$$

where $A^2 = \frac{L_p}{K}\frac{S}{V}$.

The boundary conditions imposed on equation (4.42) are similar to Levine (1999):

$$\begin{cases} p = p_i, \text{ at } r = r_i, \\ \\ p = p_o, \text{ at } r = r_o, \end{cases} \tag{4.43}$$

where p_i is the pressure acting on the ventricular wall in mmHg at $r = r_i$ and p_o is the atmospheric pressure in mmHg at the outer boundary of the parenchyma at $r = r_o$. In contrast to Levine's approach, all pressures are measured relative to the atmospheric pressure. Thus,

$$\overline{p}(r) = p(r) - p_o, \tag{4.44}$$

and using relation (4.44), the differential equation (4.42) and the boundary conditions (4.43) read

$$\frac{d^2\overline{p}(r)}{dr^2} + \frac{2}{r}\frac{d\overline{p}(r)}{dr} - A^2\overline{p}(r) = -A^2\overline{p}_v, \tag{4.45}$$

with

$$\begin{cases} \overline{p} = p_i - p_o = \overline{p}_i, \text{ at } r = r_i, \\ \\ \overline{p} = 0, \text{ at } r = r_o. \end{cases} \tag{4.46}$$

The variable change

$$P(r) = r\overline{p}(r) \tag{4.47}$$

is applied to simplify the differential equation (4.45) and the boundary conditions (4.46). It follows that

$$\frac{d^2P(r)}{dr^2} - \frac{A^2}{r}P(r) = -A^2\overline{p}_v, \tag{4.48}$$

subject to

$$\begin{cases} P = r_i \overline{p}_i, \text{ at } r = r_i \\ \\ P = 0, \text{ at } r = r_o. \end{cases} \tag{4.49}$$

The general solution of the differential equation (4.48) is

$$P(r) = C_1 e^{-Ar} + C_2 e^{Ar} + r\overline{p}_v. \tag{4.50}$$

The constants C_1 and C_2 are determined by applying the boundary conditions (4.49):

$$C_1 = \frac{r_o \overline{p}_v e^{Ar_i} + r_i(\overline{p}_i - \overline{p}_v)e^{Ar_o}}{2\sinh(A(r_o - r_i))} \tag{4.51}$$

and

$$C_2 = \frac{-r_o \overline{p}_v e^{-Ar_i} - r_i(\overline{p}_i - \overline{p}_v)e^{-Ar_o}}{2\sinh(A(r_o - r_i))}. \tag{4.52}$$

Then, the final solution is

$$P(r) = \frac{r_o \overline{p}_v e^{Ar_i} + r_i(\overline{p}_i - \overline{p}_v)e^{Ar_o}}{2\sinh(A(r_o - r_i))} e^{-Ar} - \frac{r_o \overline{p}_v e^{-Ar_i} + r_i(\overline{p}_i - \overline{p}_v)e^{-Ar_o}}{2\sinh(A(r_o - r_i))} e^{Ar} + r\overline{p}_v. \tag{4.53}$$

Finally, using the variable change (4.47), the steady state pressure distribution is

$$\overline{p}(r) = \frac{-r_o \overline{p}_v}{r} \frac{\sinh(A(r - r_i))}{\sinh(A(r_o - r_i))} + \frac{r_i(\overline{p}_i - \overline{p}_v)}{r} \frac{\sinh(A(r_o - r))}{\sinh(A(r_o - r_i))} + \overline{p}_v, \tag{4.54}$$

which reduces to Levine's result if $\overline{p}_v = \overline{p}_o = 0$. The first and second derivative of $\overline{p}(r)$, which is needed later in the radial displacement calculation, are

$$\begin{aligned} \frac{d\overline{p}(r)}{dr} = {} & \frac{r_o \overline{p}_v}{\sinh(A(r_o - r_i))} \left[-\frac{A\cosh(A(r - r_i))}{r} + \frac{\sinh(A(r - r_i))}{r^2} \right] + \\ & \frac{r_i(\overline{p}_i - \overline{p}_v)}{\sinh(A(r_o - r_i))} \left[-\frac{A\cosh(A(r_o - r))}{r} - \frac{\sinh(A(r_o - r))}{r^2} \right], \end{aligned} \tag{4.55}$$

and

$$\begin{aligned} \frac{d^2\overline{p}(r)}{dr^2} = {} & -\frac{r_i(\overline{p}_i - \overline{p}_v)}{\sinh(A(r_o - r_i))} \left[\frac{2\sinh(A(r_o - r))}{r^3} + \frac{A\cosh(A(r_o - r))}{r^2} \right] \\ & + \frac{Ar_i(\overline{p}_i - \overline{p}_v)}{\sinh(A(r_o - r_i))} \left[\frac{\cosh(A(r_o - r))}{r^2} + \frac{A\sinh(A(r_o - r))}{r} \right] \\ & + \frac{r_o \overline{p}_v}{\sinh(A(r_o - r_i))} \left[-\frac{2\sinh(A(r - r_i))}{r^3} + \frac{A\cosh(A(r - r_i))}{r^2} \right] \\ & - \frac{Ar_o \overline{p}_v}{\sinh(A(r_o - r_i))} \left[-\frac{\cosh(A(r - r_i))}{r^2} + \frac{A\sinh(A(r - r_i))}{r} \right]. \end{aligned} \tag{4.56}$$

4.2.2 Radial steady state displacement

Neglecting the external body forces, the equation of motion for the entire mixture reduces to the equilibrium equation

$$\frac{\partial}{\partial x_j} T_{ij} = 0, \tag{4.57}$$

where the summation convention over repeated indices is used and

$$T_{ij} = -p\delta_{ij} + \tau_{ij}, \tag{4.58}$$

where δ_{ij} is the Kronecker delta function, is the stress tensor of the entire mixture expressed in Cartesian coordinates. The tensor τ_{ij} is Terzaghi's effective stress which is related to the strain by

$$\tau_{ij} = \lambda e_{kk}\delta_{ij} + 2\mu e_{ij}. \tag{4.59}$$

The tissue dilatation is referred to as $e_{kk} = e$. The strain tensor e_{ij} is defined in terms of the components u_i of the displacement vector as

$$e_{ij} = \frac{1}{2}\left(\frac{\partial u_i}{\partial x_j} + \frac{\partial u_j}{\partial x_i}\right). \tag{4.60}$$

The parameters λ and μ are Lamé's constants of elasticity (with units mmHg). Then, equation (4.57) reduces to

$$\mu\nabla^2\underline{u} + (\lambda + \mu)\nabla(\nabla \cdot \underline{u}) = \nabla p, \tag{4.61}$$

which is written in coordinate independent form for simplicity. With some algebra using spherical coordinates, considering the radial component only, and employing the relative pressure $\overline{p}(r)$ as defined in equation (4.44), the differential equation (4.61) reads

$$(2\mu + \lambda)\left(\frac{d^2u_r(r)}{dr^2} + \frac{2}{r}\frac{du_r(r)}{dr} - \frac{2}{r^2}u_r(r)\right) = \frac{d\overline{p}(r)}{dr}, \tag{4.62}$$

where $\frac{d\overline{p}}{dr}$ was calculated in the previous section, equation (4.55). Applying the variable change

$$w(r) = ru_r(r) \tag{4.63}$$

yields

$$\frac{d^2w(r)}{dr^2} - \frac{2}{r^2}w(r) = \frac{r}{(2\mu + \lambda)}\frac{d\overline{p}(r)}{dr}. \tag{4.64}$$

The general solution of the differential equation (4.64) is

$$w(r) = r^2 C_3 + \frac{C_4}{r} + \frac{r}{A^2(2\mu+\lambda)}\frac{d\overline{p}(r)}{dr}, \tag{4.65}$$

and with the variable change (4.63),

$$u_r(r) = rC_3 + \frac{C_4}{r^2} + \frac{1}{A^2(2\mu+\lambda)}\frac{d\overline{p}(r)}{dr}, \tag{4.66}$$

where C_3 and C_4 are determined by the boundary conditions. The gradient of $u_r(r)$ is

$$\frac{du_r(r)}{dr} = C_3 - \frac{2C_4}{r^3} + \frac{1}{A^2(2\mu+\lambda)}\frac{d^2\overline{p}(r)}{dr^2}. \tag{4.67}$$

Now, the boundary conditions are thought of in the following way. To find the displacement of the ventricular wall, the effective stress is employed. In radial spherical geometry, the Terzaghi stress tensor is

$$\tau_{rr}(r) = \lambda e + 2\mu e_{rr} = \lambda e + 2\mu\frac{du_r}{dr}. \tag{4.68}$$

The tissue dilatation e is defined as

$$e = e_{rr} + e_{\theta\theta} + e_{\phi\phi}, \tag{4.69}$$

where $e_{rr} = \frac{du_r}{dr}$ and $e_{\theta\theta} = e_{\phi\phi} = \frac{u_r}{r}$. Then, the Terzaghi stress reads

$$\tau_{rr}(r) = \lambda\left(\frac{du_r(r)}{dr} + \frac{2}{r}u_r(r)\right) + 2\mu\frac{du_r(r)}{dr}. \tag{4.70}$$

With $u_r(r)$ given by (4.66) and $\frac{du_r}{dr}$ given by (4.67),

$$\tau_{rr}(r) = \frac{1}{A^2}\frac{d^2\overline{p}(r)}{dr^2} + \frac{2}{rA^2(2\mu+\lambda)}\frac{d\overline{p}(r)}{dr} + C_3(2\mu+\lambda+2) + C_4(1-2\mu+2\lambda). \tag{4.71}$$

Assuming that the ventricular pressure $\overline{p}_i$ acts on the ventricular wall at $r = r_i$ and that no displacement occurs at the outer boundary of the parenchyma, since the brain is rigid at $r = r_o$ due to the skull, the following boundary conditions are imposed on the total stress:

$$\begin{cases} -\overline{p}_i = (2\mu+\lambda)\frac{du_r(r)}{dr} + 2\lambda\frac{u_r(r)}{r}, \text{ at } r = r_i, \\ u_r(r) = 0, \text{ at } r = r_o. \end{cases} \tag{4.72}$$

These boundary conditions are used to solve for C_3 and C_4. Thus,

$$C_3 = \frac{r_i^3\Big(-\overline{p}_i - \frac{1}{A^2}\frac{d^2\overline{p}(r_i)}{dr^2} - \frac{2\lambda}{r_iA^2(2\mu+\lambda)}\frac{d\overline{p}(r_i)}{dr}\Big) - \frac{4r_o^2\mu}{A^2(2\mu+\lambda)}\frac{d\overline{p}(r_o)}{dr}}{r_i^3(2\mu+3\lambda) + 4r_o^3\mu} \tag{4.73}$$

and

$$C_4 = \frac{r_i^2 r_o^2 \Big[r_o \Big(r_i \overline{p}_i + \frac{r_i}{A^2} \frac{d^2 \overline{p}(r_i)}{dr^2} + \frac{2\lambda}{A^2(2\mu+\lambda)} \frac{d\overline{p}(r_i)}{dr} \Big) - \frac{r_i(2\mu+3\lambda)}{A^2(2\mu+\lambda)} \frac{d\overline{p}(r_o)}{dr} \Big]}{r_i^3(2\mu+3\lambda) + 4r_o^3\mu}. \tag{4.74}$$

where $\overline{p}(r_i)$ and $\overline{p}(r_o)$ are the boundary conditions (4.46), and

$$\frac{d\overline{p}(r_i)}{dr} = \frac{-r_o A \overline{p}_v}{r_i \sinh(A(r_o - r_i))} - \frac{A(\overline{p}_i - \overline{p}_v)\cosh(A(r_o - r_i))}{\sinh(A(r_o - r_i))} + \frac{\overline{p}_v - \overline{p}_i}{r_i}, \tag{4.75}$$

$$\frac{d\overline{p}(r_o)}{dr} = \frac{-A\overline{p}_v \cosh(A(r_o - r_i))}{\sinh(A(r_o - r_i))} + \frac{\overline{p}_v}{r_o} - A\frac{r_i}{r_o}\frac{(\overline{p}_i - \overline{p}_v)}{\sinh(A(r_o - r_i))}, \tag{4.76}$$

and

$$\begin{aligned}\frac{d^2\overline{p}(r_i)}{dr^2} &= -(\overline{p}_i - \overline{p}_v)\left[\frac{2}{r_i^2} + \frac{A\cosh(A(r_o - r_i))}{r_i \sinh(A(r_o - r_i))}\right] \\ &\quad + A(\overline{p}_i - \overline{p}_v)\left[\frac{\cosh(A(r_o - r_i))}{r_i \sinh(A(r_o - r_i))} + A\right] + \frac{2r_o A\overline{p}_v}{r_i^2 \sinh(A(r_o - r_i))}.\end{aligned} \tag{4.77}$$

Substituting C_3 from (4.73) and C_4 from (4.74) into the general solution (4.66) results in the formula for the radial displacement of the parenchyma tissue at steady state.

The steady state radial displacement solution is messy; it has been checked using MATLAB that the solution satisfies the radial displacement differential equation and boundary conditions. However, one can evaluate $\frac{d\overline{p}(r)}{dr}$ (4.55) at r_i and r_o as well as $\frac{d^2\overline{p}(r)}{dr^2}$ (4.56) at r_i and simplify the results by the approximation that $\sinh(x) \to \cosh(x)$ as $x \to \infty$. Since the value of A in the argument of sinh and cosh is large enough for this approximation to be accurate to 9 decimal places, the derivates can be written as follows:

$$\frac{d\overline{p}(r_i)}{dr} = -\frac{r_o A\overline{p}_v}{r_i \sinh(A(r_o - r_i))} - \frac{(\overline{p}_i - \overline{p}_v)(1 + r_i A)\cosh(A(r_o - r_i))}{r_i \sinh(A(r_o - r_i))}; \tag{4.78}$$

$$\frac{d\overline{p}(r_o)}{dr} = \frac{\overline{p}_v(1 - r_o A)\cosh(A(r_o - r_i))}{r_o \sinh(A(r_o - r_i))} - A\frac{r_i}{r_o}\frac{(\overline{p}_i - \overline{p}_v)}{\sinh(A(r_o - r_i))}; \tag{4.79}$$

and

$$\frac{d^2\overline{p}(r_i)}{dr^2} = \frac{r_i(\overline{p}_i - \overline{p}_v)\cosh(A(r_o - r_i))}{\sinh(A(r_o - r_i))}\left[\frac{2}{r_i^3} + \frac{2A}{r_i^2} + \frac{A^2}{r_i}\right] + \frac{2r_o A\overline{p}_v}{r_i^2 \sinh(A(r_o - r_i))}. \tag{4.80}$$

Equations (4.78), (4.79), and (4.80) can be substituted in the expression for C_3 given by (4.73) and the expression for C_4 given by (4.74); however, the radial displacement solution (4.66) remains complex nevertheless.

4.3 Results

In this Section, the steady state results for both the pressure and the ventricle displacement are given and compared with Levine's (1999) results for the SEPA hypothesis.

4.3.1 Parameters

The radial values for the brain are chosen to represent a brain that has been altered due to normal pressure hydrocephalus. The ventricle wall and the outer edge of the parenchyma are at $r_i = 4$ cm and $r_o = 8$ cm, as found in Levine (1999) for the SEPA hypothesis. It is assumed that parenchymal compression has occurred (due to the ventricular expansion), since Levine (1999) states that in a normal brain without any ventricular expansion, $r_i = 2$ cm.

All pressure values for the new model are relative to the atmospheric pressure of 760 mmHg. A characteristic feature of normal pressure hydrocephalus is that the ventricular pressure (or the intracranial pressure) is identical to that of a normal brain. The normal range for intracranial pressure is measured to be $0 - 10$ mmHg. At the upper limit of the normal range, $20 - 25$ mmHg, treatment should be initiated to relieve the brain pressure (Ghajar, 2000). Thus, in the mixture-theory based model, the ventricular pressure $\overline{p}_i$ at r_i is taken to be 15 mmHg, as the average of the higher extreme of the normal range and the lower extreme of the upper limit. At $r = r_o$, the pressure is assigned to be the atmospheric pressure of 0 mmHg, since the subarachnoid space is in contact with the sagittal sinus; the sagittal sinus pressure is $3 - 8$ mmHg relative to the atmospheric pressure, and may fall as low as -10 mmHg (Albright et al., 1991); so 0 mmHg is roughly the average. The venous pressure $\overline{p}_v$ in the brain is varied so that its effects on the model can be investigated. The values of $\overline{p}_v$ which are used in the model are -5 mmHg, -2 mmHg, and 0 mmHg.

The parameter A^2 is defined as $\frac{L_p}{K}\frac{S}{V}$, where L_p is the permeability of the veins, $\frac{S}{V}$ is the surface area density of the veins, and K is the hydraulic conductivity of the parenchyma. Assuming that the brain tissue is similar to normal tissue, the values for A^2 are taken from Jain et al., (2007), noting that the values quoted for the capillaries are used for the veins as a crude approximation: $L_p = 3.6 \times 10^{-8}$ cm second^{-1} mmHg^{-1}, $K = 2.5 \times 10^{-7}$ cm^2 second^{-1} mmHg^{-1}, and $\frac{S}{V} = 50 - 250$ cm^{-1}. From these, the dimension of A^2 is easily calculated to be L^{-2}, where L represents length. The values for A_1^2, A_2^2, and A_3^2 are calculated by varying

$\frac{S}{V}$ from the lower extreme of 50 cm^{-1}, to the average of 150 cm^{-1}, and to the higher extreme of 250 cm^{-1}, as seen in Table 4.1. Also, in Levine (1999), the parameter $k = \frac{k'}{\hat{k}}$ (where the permeability coefficient k' comes from Darcy's law and the absorption coefficient $\hat{k}$ comes from Starling's law) has the units cm^2, or the dimension of L^2. One can write the inversely proportional relation between A^2 and k,

$$A^2 = \frac{1}{k}, \tag{4.81}$$

and Table 4.1 shows the corresponding k values as well. For the value k_4, Levine uses 0.1 cm^2 in his analysis, and the corresponding A_4^2 is 10 cm^{-2} by equation (4.81). Since the actual values for k' and $\hat{k}$ are not given when considering k_4, the values for K and L_p are used to calculate the values for $\frac{S}{V}$. In other words, since $k = \frac{k'}{\hat{k}} = 0.1$ cm^2 for Levine, and in the mixture-theory based model, $k = \frac{1}{A^2} = \frac{K}{L_p \frac{S}{V}}$, the vascular surface density is extracted from the equation $10 = \frac{K}{L_p \frac{S}{V}}$ by using the values K and L_p from Jain et al., (2007).

Vascular surface area density $\frac{S}{V}$ (cm^{-1})	A_i^2 (cm^{-2})	k_i (cm^2)
50	$A_1^2 = 7.2$	$k_1 = 0.14$
150	$A_2^2 = 21.6$	$k_2 = 0.05$
250	$A_3^2 = 36$	$k_3 = 0.03$
69	$A_4^2 = 10$	$k_4 = 0.1$

Table 4.1: Parameter values for A^2 and k

The values of the elastic moduli are needed for the displacement distribution. For the mixture-theory based model, the Lamé parameters are taken from Chapter 2; the values $\mu = 3.6 \times 10^4$ mmHg and $\lambda = 1.5 \times 10^5$ mmHg, to ensure consistency with the assumptions made in mixture theory (that asymptotic values for the solid matrix are used, and not those of the biological tissue). Also, the elastic moduli in Levine (1999) are taken for comparison purposes. Levine mentions that the Poisson ratio ν is 0.35 and provides the following values for Young's modulus E: the range $1 - 2 \times 10^4$ Nm^{-2} and 1×10^3 Nm^{-2}, as cited in Taylor and Miller (2004). Converting the Young's modulus values into millimeters of mercury and fixing $\nu = 0.35$, the corresponding Lamé's coefficients are calculated using the following relations:

$$\mu = \frac{E}{2(1+\nu)}, \tag{4.82}$$

and

$$\lambda = \frac{E\nu}{(1+\nu)(1-2\nu)}. \tag{4.83}$$

Table 4.2 shows the Lamé coefficients when Young's modulus is varied with a fixed Poisson ratio.

E (Nm^{-2})	E (mmHg)	μ (mmHg)	λ (mmHg)
1×10^3	7.5	2.8	6.5
1×10^4	75	27.8	64.8
2×10^4	150	55.6	129.6

Table 4.2: Levine (1999) Lamé coefficient values with fixed $\nu = 0.35$

4.3.2 Radial steady state pressure distribution

The radial steady state pressure profiles were obtained from

$$\overline{p}(r) = \frac{-r_o\overline{p}_v}{r}\frac{\sinh(A(r-r_i))}{\sinh(A(r_o-r_i))} + \frac{r_i(\overline{p}_i-\overline{p}_v)}{r}\frac{\sinh(A(r_o-r))}{\sinh(A(r_o-r_i))} + \overline{p}_v, \tag{4.84}$$

using the A^2 values from Table 4.1, and varying the venous pressure $\overline{p}_v$. The results are shown in Figures 4.1-4.4.

From these figures, it is evident that the larger the value of A^2 is – that is, the larger the value of $\frac{S}{V}$ is – the faster the pressure drops from its value at $r = r_i$ to the venous pressure $\overline{p}_v$, before increasing to the atmospheric pressure $\overline{p}_o$ close to $r = r_o$. All figures show that CSF is absorbed at locations between 4.5 cm and 5.5 cm in the parenchyma. Furthermore, the value of $\overline{p}_v$ plays a profound role in the behavior of the steady state pressure distribution. If $\overline{p}_v$ is slightly less than p_o, then the pressure from the ventricle wall drops to $\overline{p}_v$ and rebounds back to p_o close to the outer edge of the parenchyma. If $\overline{p}_v$ is equal to 0 mmHg, then equation (4.84) becomes

$$\overline{p}(r) = \frac{r_i\overline{p}_i}{r}\frac{\sinh(A(r_o-r))}{\sinh(A(r_o-r_i))}, \tag{4.85}$$

which coincides with Levine's (1999) steady state solution (4.8). In this case, CSF absorption occurs approximately within a centimeter from the ventricular wall and the pressure remains constant throughout the parenchyma all the way to the outer edge. This means that most of the CSF absorption occurs very close to the ventricular wall.

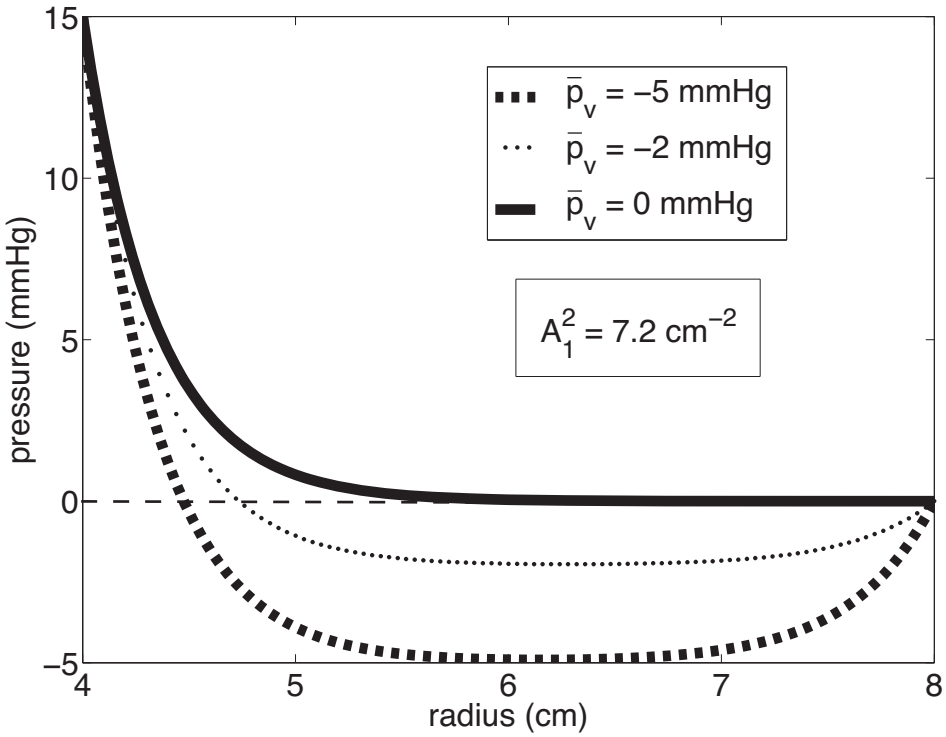

Figure 4.1: Steady state pressure profile with $A_1^2 = 7.2$ cm^{-2}

Finally, it is important to mention the effect of $\overline{p}_v$ below the atmospheric pressure. When $\overline{p}_v$ is less than 0 mmHg, the IFP slightly increases near the outer boundary. This implies that the filtration velocity, given by Darcy's law, reverses its direction and a small amount of CSF from the subarachnoid space enters the brain parenchyma to be absorbed nearby. This effect has been observed by Kenyon (1976a) who refers to it as "retrograde filtration". In Figures 4.1-4.4, the retrograde filtration is hardly noticeable when the venous pressure is very close to atmospheric pressure.

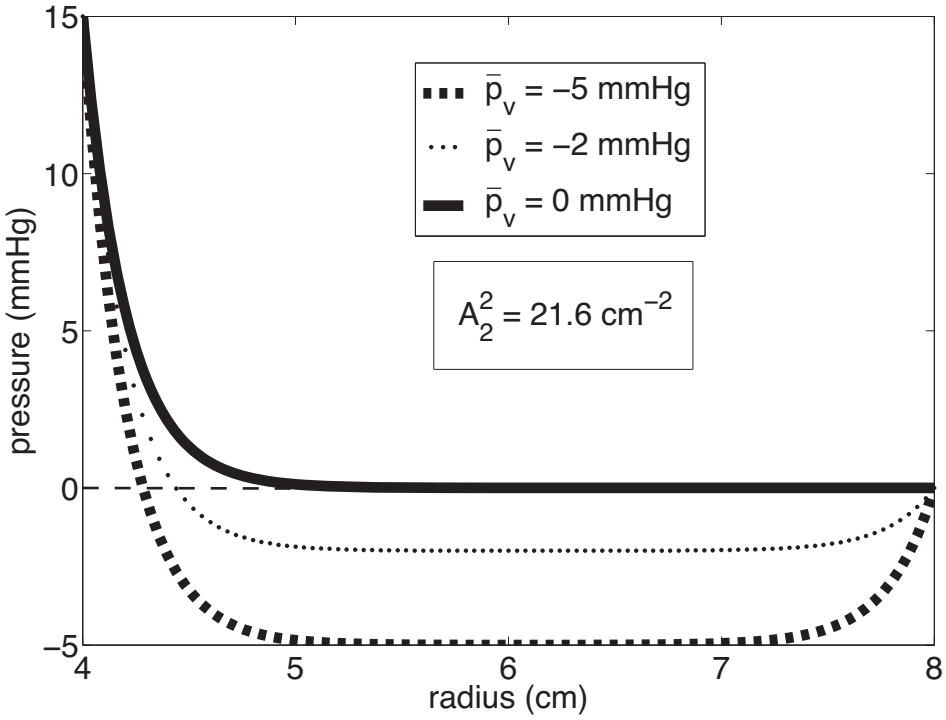

Figure 4.2: Steady state pressure profile with $A_2^2 = 21.6$ cm^{-2}

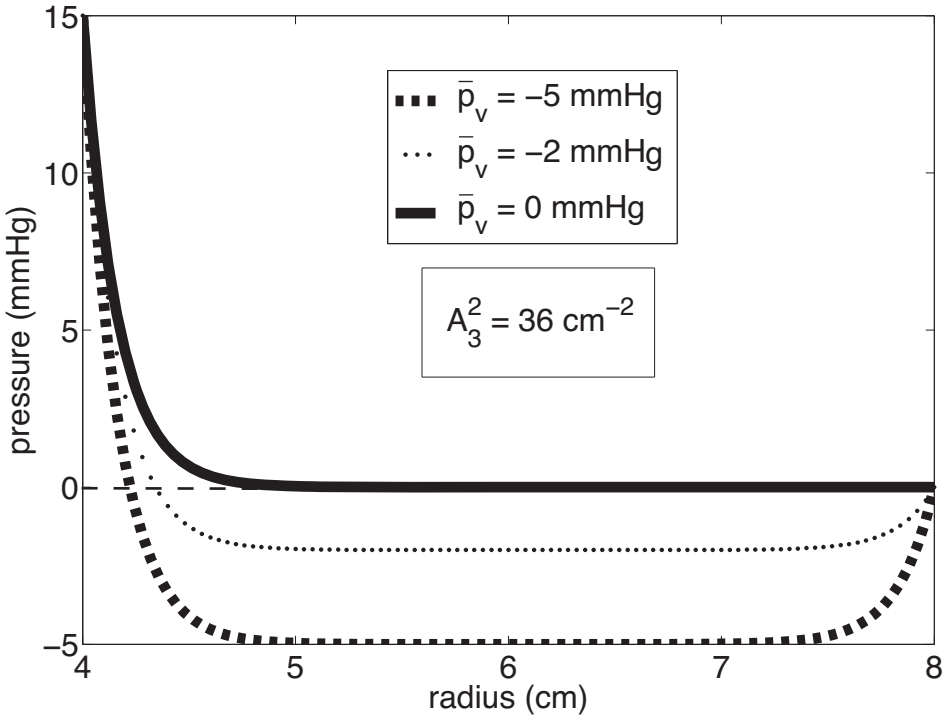

Figure 4.3: Steady state pressure profile with $A_3^2 = 36$ cm^{-2}

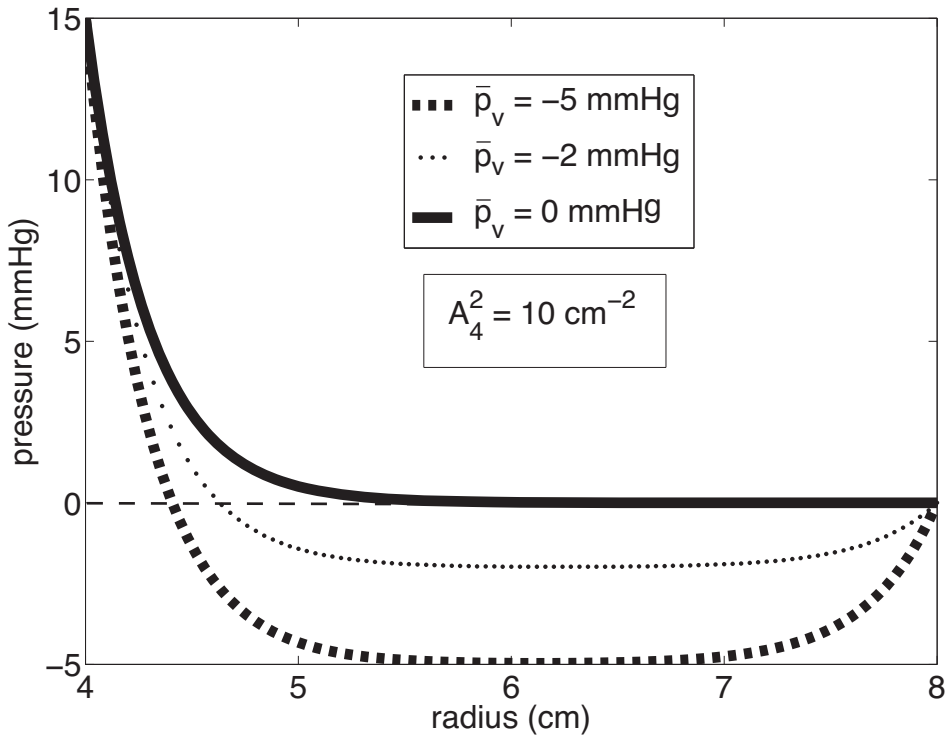

Figure 4.4: Steady state pressure profile with $A_4^2 = 10\ \text{cm}^{-2}$

4.3.3 Radial steady state displacement distribution

According to the mixture theory model, the radial steady state displacement $u_r(r)$ is given by equations (4.66) and (4.73)-(4.77). Its numeric values are presented in Table 4.3; the first column shows the range of values of A^2, as in Table 4.1, and the second column indicates the range of values of the venous pressure. The value of the ventricular radius is $r_i = 4$ cm, as in Levine (1999), under the SEPA hypothesis, and the elastic parameters are $\mu = 3.6 \times 10^4$ mmHg and $\lambda = 1.5 \times 10^5$ mmHg as used before. Since in all cases the values of $u_r(r_i)$ are negligible, it clearly shows that the ventricular displacement is independent of the vascular surface area density $\frac{S}{V}$ and of the venous pressure $\overline{p}_v$.

A_i^2 (cm^{-2})	$\overline{p}_v$ (mmHg)	$u_r(r_i)$ (cm)
$A_1^2 = 7.2$	-5	5.6×10^{-4}
	-2	5.2×10^{-4}
	0	4.9×10^{-4}
$A_2^2 = 21.6$	-5	5.7×10^{-4}
	-2	5.2×10^{-4}
	0	5.0×10^{-4}
$A_3^2 = 36$	-5	5.7×10^{-4}
	-2	5.3×10^{-4}
	0	5.0×10^{-4}
$A_4^2 = 10$	-5	5.6×10^{-4}
	-2	5.2×10^{-4}
	0	5.0×10^{-4}

Table 4.3: Ventricular displacement $u_r(r_i)$ according to the mixture theory model

μ, λ (mmHg)	A_i^2 (cm^{-2})	$\overline{p}_v$ (mmHg)	$u_r(r_i)$ (cm)
2.8, 6.5	$A_1^2 = 7.2$	-5	8.1
		-2	7.6
		0	7.2
	$A_3^2 = 36$	-5	8.4
		-2	7.7
		0	7.3
55.6, 129.6	$A_1^2 = 7.2$	-5	0.41
		-2	0.38
		0	0.36
	$A_3^2 = 36$	-5	0.42
		-2	0.39
		0	0.37

Table 4.4: Ventricular displacement $u_r(r_i)$ according to the elastic parameters suggested by Levine (1999) with $r_i = 4$ cm

The ventricular displacement becomes extremely sensitive when changing the elastic parameters μ and λ (or G and ν in the notation by Levine (1999)). When $\mu = 2.8$ mmHg and $\lambda = 6.5$ mmHg, for any A^2 and $\overline{p}_v$ values, the ventricular displacement ranges from 7.2 cm to 8.4 cm which is far too large. The brain parenchyma would be severely compressed. Also, Levine's model predicts compression of the brain beyond the outer boundary which is set at 8 cm which is clearly not realistic. These values are not an error in the calculations using the mixture theory model. Furthermore, for the case when $\mu = 55.6$ mmHg and $\lambda = 129.6$ mmHg, the ventricular wall displacement, for any A^2 and $\overline{p}_v$ values, ranges from 0.36 cm to 0.42 cm. Here, these displacement values seem acceptable to explain normal pressure hydrocephalus; however, the Lamé parameters represent of the values of the brain tissue and not of the asymptotic values of the solid matrix in accordance to the assumptions made in mixture theory.

Chapter 5

Discussion and conclusion

The center of attention of this Thesis is the development of mathematical models, using theory of poroelasticity (developed in the study of the flow through a porous medium), and their application to biological tissues.

Two mechanisms suggest a time dependence when describing the flow through a porous medium. The first mechanism occurs as the fluid permeates an elastic porous material. The drag force between the fluid and the solid may cause the solid matrix to deform. Conversely, the solid matrix can deform due to a force being applied to it, which may induce a fluid flow in the pores. These mechanisms can be coupled, and the mechanical properties of the material assume a time-dependent character.

The theory of poroelasticity has a long and distinguished history, which one can find in a recent monograph by de Boer (2000). There exist two versions of the theory:

a. Consolidation Theory, developed by M. Biot (1941) in the context of soil mechanics and ground waterflow; and
b. Mixture Theory, whose name derives from early theoretical developments involving mixtures of gases (de Boer, 2000).

The two versions have been shown to be equivalent (e.g. Simon, 1992); however, in this work, the Mixture Theory version of poroelasticity is employed because of its sharper theoretical formulation.

Chapter 2 uses Mixture Theory to derive a mathematical model that explains the mechanism responsible for the increase of the IFP in solid tumors. A similar model, also using Mixture Theory, was previously formulated by Netti et al. (1995, 1997) from a different point of view. The model starts with the IFP steady state in a fully developed tumor. Artificially, the IFP is perturbed from its steady state in order to study the response of the IFP when

the vascular pressure was increased and later, decreased. One of the main findings was that the changes in IFP are closely related to the vascular pressure variations with a time delay of approximately 10 seconds. The time delay is highly influenced by the choice of the Lamé parameters – i.e., the stiffness parameters λ and μ – reputedly valid for soft biological tissue.

As mentioned in the analysis of Chapter 2, the Lamé parameters for biological tissue are inconsistent with one of the fundamental assumptions of Mixture Theory. The parameter should be that of only the solid matrix, and the viscoelasticity of the solid constituent is negligible. In Appendix A where Mixture Theory is formulated, it is pointed out that the asymptotic values of the elastic moduli λ and μ must be used. Although these values have never been reported in literature, the order of magnitude of the elastic moduli should be greater than those reported by Netti et al. (1995, 1997), close to the measured values for saturated soft clay, listed in Table 2.2 and used in the simulations. The elastic moduli values have a profound effect on the identification of the appropriate time scale over which the IFP grows to reach the observed elevated value at steady state.

In fact, Netti et al. (1995, 1997) define the time scale by the parameter

$$T = \frac{R^2}{K(2\mu + \lambda)}, \tag{5.1}$$

which arises from the non-dimensionalization of the mathematical problem, whereas Chapter 2 identifies the time scale which is linked the type of a solid tumor. Based on Chapter 2, equation (2.24),

$$L_p(\hat{t}) = L_p^0 \left[1 + \hat{C}\left(1 - e^{-\hat{D}\hat{t}}\right)\right], \tag{5.2}$$

the IFP steady state is obtained as soon as the value of the vascular permeability $L_p(\hat{t})$ reaches very close to $L_p(\infty)$. In turn, the rate at which steady state is reached depends on the parameter $\hat{D}$ that represents the rate of tumor growth, which is known to vary from tumor to tumor (Bates and Curry, 1996). Some typical values of this parameter are shown in Table 2.3, and are used to simulate the steady state and the transient IFP profile, shown in Figure 2.5-2.7 for a fixed location inside the tumor. These figures clearly show that the pressure trend is the same, but the time for when steady state is reached is different depending on the tumor type.

The existence of different time scales has already been found experimentally by Khosravani et al. (2004) and by Milosevic et al. (2008). With a sudden insertion of a needle into the

center of the tumor (which was part of the measurement system), the transient fluid response was recorded. To understand the cause of the IFP behavior, simulations were created, based on a discrete mathematical model which does not use poroelasticity theory. The conclusion was that the shape and the time period of the pressure recordings were due to the variations of the hydraulic conductivity K in the tumor interstitium. However, the Mixture Theory model in Chapter 2 offers an alternative explanation of the existence of different time scales. It is difficult to say more than this until in situ measurements of K can be done, which requires overcoming serious technical challenges as stated in Milosevic et al. (2008).

A second investigation using Mixture Theory is reported in Chapter 3 of this Thesis, but for the moment its discussion is postponed in order to proceed first with the application found in Chapter 4. As stated in Chapter 1, the objective is to determine whether a Mixture Theory based mathematical model can explain the pathogenesis of normal pressure hydrocephalus under the hypothesis that most of the cerebrospinal fluid (CSF) is effectively absorbed in the brain parenchyma, rather than in the arachnoid villi as commonly believed. The idea is that as CSF crosses the ventricular wall and flows through the parenchymal interstitium to be absorbed by the venous blood, it drags along the solid matrix and produces a finite displacement of the ventricular wall. As the wall expands, the permeability of the wall increases and smaller pressure gradients are needed to push the CSF into the parenchyma, so that the intracranial pressure is indistinguishable from that of the pressure in a normal brain. This hypothesis has been adopted by Levine (1999) and analyzed using Biot's consolidation theory along with the addition of Starling's law – or a reduced form of it.

The mathematical model constructed and used in Chapter 4 shows that Levine's conclusions are not tenable, because the displacements of the ventricular wall implied by the parenchymal absorption hypothesis are negligible. Interestingly enough, a similar conclusion was reached by Sobey and Wirth (2006), where consolidation theory was also used under the assumption that the parenchymal permeability is a function of the dilatation. The use of a Poiseuille-like law describes the fluid mechanics of the CSF flowing in the aqueduct of Sylvius.

In the analysis of Levine (1999), several misunderstandings of consolidation theory appear and need to be addressed. For instance, the nature of the porous medium being the brain is defined as: "The parenchyma consists of three components: a solid matrix permeated by two networks of fluid-filled channels. [...] The first fluid network consists of the interstitial fluid

in the interconnected channels of extracellular space. [...] The second fluid network consists of the blood in the cerebral vessels [...]. Although all of the solid and fluid elements are intrinsically incompressible [...] the three components of the parenchyma are analogous to a porous soil consisting of solid, incompressible elements (the solid matrix) and pores occupied by both water (interstitial fluid) and pockets of air (intravascular blood)" (Levine, 1999, pages 880-881). This is not a proper analogy. The gas phase in Biot's consolidation theory is compressible, while the intravascular blood is not, by the assumption in Levine (1999). In fact, when describing the meaning of the parameters α and Q in the formula for the variation of the pore water content θ,

$$\theta = \alpha\epsilon + \frac{\sigma}{Q}, \tag{5.3}$$

where ϵ is the dilatation and σ is the pore pressure, Biot (1941) states that: "It is quite obvious that the constants α and Q will be of significance for a soil not completely saturated with water and containing air bubbles" (Biot, 1941, page 159).

Another misunderstanding of the poroelasticity theory occurs when the values of elastic moduli for the porous medium are discussed in Levine (1999). Very low values are favored for the shear modulus G (approximately 400 $\frac{N}{m^2}$) and the Poisson ratio ν (about 0.35). Moreover, it is suggested that in later stages of normal pressure hydrocephalus both G and ν increase because the brain becomes more rigid. This contradicts the initial assumption that all the poroelasticity parameters are constant.

These problems do not occur in the derivation of the mathematical model based on Mixture Theory in Chapter 4. As already mentioned in connection with the work done in Chapter 2, the values of the elastic moduli must be chosen so that the viscoelasticity of the solid matrix is negligible. Furthermore, there is no confusion about the pore water content θ as in Biot (1941), for both the water content and the solid content are represented by their respective volume fractions. This follows from the homogenization procedure, which starts from the individual equations for the fluid and the solid and then is averaged to produce a mixture in which each point contains both the fluid and the solid phases. Thus, the fluid and solid volume fractions become scalar fields – see Appendix A for details.

The mathematical models presented in this Thesis are still limited by the assumptions necessary in the formulation of Mixture Theory. Among the assumptions are:

i. Homogeneity and isotropy;

ii. Linearity of the stress-strain relations;

iii. Small strains; and,

iv. Validity of Darcy's law and the modified version of Starling's law (i.e., the complete neglect of the osmotic pressure).

In Chapter 2, a further assumption is made to make the mathematical work more manageable, which is common with most other works (e.g., Netti et al., 1995, 1997). The pore pressure is taken to be proportional to the tissue dilatation. Chapter 3 investigates the validity of this assumption by solving the exact system of PDEs and comparing the results with the proportionality assumption. To simplify the calculations, the case of no sinks or sources is considered in Chapter 3 for a hollow spherical sand drain. This is analogous with the work done by De Leeuw (1965) for a hollow cylindrical sand drain. The conclusion is that the proportionality, in general, is quite poor. As a result, a future direction of research would be to extend the work in Chapter 3 by adding a source and/or sink terms to test against the model used in Chapter 2.

Appendix A

Formulation of mixture theory

The main focus of this Appendix A is to present the formulation of mixture theory in detail. The reader can also refer to Kenyon (1976b) for a more general and in depth derivation of mixture theory.

In mixture theory, the continuum is modeled as a poroelastic medium in which the pores are completely filled with a Newtonian viscous fluid and the solid skeleton is linearly elastic. The medium is initially homogeneous and both phases are intrinsically incompressible; that is, the unjacketed compressibility (Biot and Willis, 1957) is negligible for the range of pore pressure intended here, and compression of the medium occurs only because of a redistribution of the fluid and the solid components. Inertia forces associated with seepage in the matrix are negligible because the Reynolds number based on pore size is much smaller than 1. Furthermore, the inertia in the bulk material is disregarded as long as the relaxation time for the constant strain is much shorter than the consolidation time. Finally, the effects due to matrix viscoelasticity will be negligible provided that the relaxation time for solid dilatation is small compared to the consolidation time and that the asymptotic values of the elastic moduli μ and λ are used to characterize the matrix stiffness (Kenyon, 1976b). Roughly speaking, this means that the rate of change of volume in the bulk material is assumed to be limited by the speed with which fluid can enter the pores, and not by the speed with which the matrix can relax independently of pore fluid flow.

The domain of the homogeneous continuum is taken to be a subset $\mathbf{D} \subset \mathbf{R^3}$. Spatial and temporal coordinates are denoted by r and t respectively. Define $F(r,t)$ to be the difference between the source of fluid and the sink of fluid per unit time while the solid phase

is conserved. On $\mathbf{D}$, the conservation of mass equation for the fluid phase f and the solid phase s in the presence of $F(r,t)$ is written as:

$$\frac{\partial \rho^f}{\partial t} + \nabla \cdot \left(\rho^f \underline{v}^f\right) = F \tag{A1}$$

$$\frac{\partial \rho^s}{\partial t} + \nabla \cdot (\rho^s \underline{v}^s) = 0, \tag{A2}$$

where ρ^f and ρ^s are the apparent densities and $\underline{v}^f$ and $\underline{v}^s$ are the velocities. Adding term by term equations (A1) and (A2), it yields

$$\frac{\partial \rho}{\partial t} + \nabla \cdot (\rho \underline{v}) = F, \tag{A3}$$

where the mass density is $\rho = \rho^f + \rho^s$ and the momentum density is $\rho\underline{v} = \rho^f \underline{v}^f + \rho^s \underline{v}^s$.

The first step is to rewrite equations (A1) and (A2) in terms of true density ρ_T defined as:

$$\text{true mass density of fluid: } \rho_T^f = \Delta M^f / \Delta V^f$$

$$\text{true mass density of solid: } \rho_T^s = \Delta M^s / \Delta V^s.$$

In what follows, ρ_T^f and ρ_T^s are assumed dependent on t only (and not on the location in space). The relation between apparent density and true density of the fluid phase is

$$\rho^f = \frac{\Delta M^f}{\Delta V} = \frac{\Delta M^f}{\Delta V^f}\frac{\Delta V^f}{\Delta V} = \rho_T^f \phi^f \tag{A4}$$

where $\phi^f = \Delta V^f / \Delta V$ is the volume fraction of the fluid. Likewise,

$$\rho^s = \frac{\Delta M^s}{\Delta V} = \frac{\Delta M^s}{\Delta V^s}\frac{\Delta V^s}{\Delta V} = \rho_T^s \phi^s \tag{A5}$$

where $\phi^s = \Delta V^s / \Delta V$ is the volume fraction of the solid. Note that ϕ^f and ϕ^s are functions of both r and t and are related by $\phi^f + \phi^s = 1$ which means that the biphasic material is completely saturated. Thus, using equations (A4) and (A5) in (A1) and (A2) gives

$$\frac{\partial \rho_T^f \phi^f}{\partial t} + \nabla \cdot \left(\rho_T^f \phi^f \underline{v}^f\right) = F \tag{A6}$$

$$\frac{\partial \rho_T^s \phi^s}{\partial t} + \nabla \cdot (\rho_T^s \phi^s \underline{v}^s) = 0. \tag{A7}$$

Next, taking into account the assumption that each phase is incompressible and expanding equations (A6) and (A7), it follows that

$$\frac{\partial \phi^f}{\partial t} + \nabla \cdot \left(\phi^f \underline{v}^f\right) = q(r,t) \tag{A8}$$

$$\frac{\partial \phi^s}{\partial t} + \nabla \cdot (\phi^s \underline{v}^s) = 0, \tag{A9}$$

where the quantity on the right hand side of equation (A8) is $q(r,t) = \frac{F}{\rho_T^f}$.

Adding term by term equations (A8) and (A9), and taking into account the condition of full saturation, $\phi^f + \phi^s = 1$, gives

$$\nabla \cdot \left(\phi^f \underline{v}^f + (1 - \phi^f) \frac{\partial \underline{u}}{\partial t} \right) = q, \tag{A10}$$

where $\underline{u}$ is the solid displacement vector. From equation (A10), the volumetric flux $\underline{M}$ can be extracted:

$$\underline{M} = \left(\phi^f \underline{v}^f + (1 - \phi^f) \frac{\partial \underline{u}}{\partial t} \right) = \underline{N} + \frac{\partial \underline{u}}{\partial t}, \tag{A11}$$

where $\underline{N}$ is the relative velocity of the fluid and the solid:

$$\underline{N} = \phi^f \left(\underline{v}^f - \frac{\partial \underline{u}}{\partial t} \right). \tag{A12}$$

Then, by Darcy's law, it follows that

$$\underline{N} = -\frac{k}{\eta} \nabla p = -K \nabla p, \tag{A13}$$

where k is the permeability of the porous medium, η is the shear viscosity of the fluid and p is the pore fluid pressure. The constant K equals k divided by η. Since $\nabla \cdot \underline{M} = q(r,t)$, the refined result is

$$\frac{\partial e}{\partial t} - K \nabla^2 p = q, \tag{A14}$$

where $e = \nabla \cdot \underline{u}$ is the solid or tissue dilatation.

Now, conservation of momentum equations for each phase are introduced as:

$$\rho^f \left(\frac{\partial \underline{v}^f}{\partial t} + \underline{v}^f \cdot \nabla \underline{v}^f \right) = \nabla \cdot \underline{\underline{\mathbb{T}}}^f \tag{A15}$$

$$\rho^s \left(\frac{\partial \underline{v}^s}{\partial t} + \underline{v}^s \cdot \nabla \underline{v}^s \right) = \nabla \cdot \underline{\underline{\mathbb{T}}}^s, \tag{A16}$$

where $\underline{\underline{\mathbb{T}}}^f$ and $\underline{\underline{\mathbb{T}}}^s$ are the stress tensors for the fluid and the solid respectively. Body forces are neglected in equations (A15) and (A16) due to the very small effect on the continuum. Inertia forces associated with seepage in the matrix are negligible on the grounds that the Reynolds number based on pore size is much smaller than one and that the relaxation time

for constant strain of the bulk material is much shorter than the consolidation time. Thus, neglecting body forces and inertia forces reduces the above equations to:

$$\nabla \cdot \underline{\underline{\mathbb{T}}}^f = 0 \tag{A17}$$

$$\nabla \cdot \underline{\underline{\mathbb{T}}}^s = 0. \tag{A18}$$

Now, the form of the constitutive equation for the fluid phase is

$$\underline{\underline{\mathbb{T}}}^f = \left(-\phi^f p + \xi \nabla \cdot \underline{v}^f\right) \underline{\underline{\mathbb{I}}} + 2\eta \underline{\underline{\mathbb{D}}}, \tag{A19}$$

where p is the pore fluid pressure, ξ is the second viscosity coefficient, $\underline{\underline{\mathbb{I}}}$ is the identity matrix, η is the shear viscosity, and $\underline{\underline{\mathbb{D}}}$ is the rate of strain. Note that the fluid phase is incompressible which implies that $\nabla \cdot \underline{v}^f = 0$, then equation (A19) becomes

$$\underline{\underline{\mathbb{T}}}^f = -\phi^f p \underline{\underline{\mathbb{I}}} + 2\eta \underline{\underline{\mathbb{D}}}, \tag{A20}$$

which is approximately

$$\underline{\underline{\mathbb{T}}}^f \approx -\phi^f p \underline{\underline{\mathbb{I}}}. \tag{A21}$$

Equation (A20) holds under the assumption of mixture theory that the fluid phase is a Newtonian viscous fluid. Hence, equation (A21) implies that the tensor $\underline{\underline{\mathbb{D}}}$ is negligible on the grounds that the contact forces of the solid phase are greater than the viscous forces of the fluid phase. Finally, the constitutive equation for the solid phase is written as:

$$\underline{\underline{\mathbb{T}}}^s = (-\phi^s p + \lambda^s \nabla \cdot \underline{u}) \underline{\underline{\mathbb{I}}} + 2\mu^s \underline{\underline{\epsilon}}, \tag{A22}$$

where λ^s and μ^s are Lamé's elasticity parameters and $\underline{\underline{\epsilon}}$ is the strain tensor.

The relation of these tensors to the other field variables – i.e., the constitutive theory of a general incompressible fluid-solid mixture – has been given by Kenyon (1976b) among others. Specialized to this system, using equations (A21) and (A22), a constitutive equation for the whole mixture is derived. This is done by adding equations (A21) and (A22) and by employing the fact that the biphasic material is completely saturated, $\phi^s + \phi^f = 1$:

$$\underline{\underline{\mathbb{T}}}^m = \underline{\underline{\mathbb{T}}}^f + \underline{\underline{\mathbb{T}}}^s = -p \underline{\underline{\mathbb{I}}} + \tau_{ij}, \tag{A23}$$

where m represents the mixture and τ_{ij} is the contact stress defined as

$$\tau_{ij} = \lambda e \underline{\underline{\mathbb{I}}} + 2\mu \underline{\underline{\epsilon}}. \tag{A24}$$

In order to avoid clutter, the elasticity parameters will be denoted as μ and λ.

In the derivation of mixture theory, Kenyon (1976b) pointed out that the pore fluid pressure p produces an effective bulk area-averaged hydrostatic pressure in the fluid in the mixture of amount $\phi^f p$. Similarly, it produces an effective bulk area-averaged hydrostatic pressure of amount $\phi^s p$ in the solid. It has no other effect on the solid, in the sense that the pore pressure acting on the solid elements does not produce any change in shape and, in particular, does not induce any 'cell–to–cell' contact. Therefore, the contact stress τ_{ij} of equation (A24) coincides with the Terzaghi stress (Terzaghi, 1943).

Then, the equation of motion becomes

$$\nabla \cdot \underline{\underline{\mathbb{T}}}^m = \nabla \cdot \left(\underline{\underline{\mathbb{T}}}^f + \underline{\underline{\mathbb{T}}}^s \right) = 0, \tag{A25}$$

which reduces to

$$-\nabla p + (\mu + \lambda)\nabla(\nabla \cdot \underline{u}) + \mu \nabla^2 \underline{u} = 0. \tag{A26}$$

Taking the divergence of each term and remembering the fact that $e = \nabla \cdot \underline{u}$ is the solid dilatation, equation (A26) can be written as

$$(2\mu + \lambda)\nabla^2 e = \nabla^2 p. \tag{A27}$$

Together with $e = \nabla \cdot \underline{u}$, equations (A14) and (A26) form a closed system of five equations with five unknown variables: e, p, and the three components of $\underline{u}$.

Appendix B

Relation between tissue dilatation and interstitial fluid pressure

In this Appendix, the relation between the tissue dilatation e and the interstitial fluid pressure (IFP) p is discussed in detail. As shown in Appendix A, the form of this relation depends crucially on the harmonic function f given by equation (A30). In particular, when $f = 0$, then e and p are proportional, and this assumption was used by Netti et al. (1995, 1997) as well as in follow-up works - including this one, in particular in Chapter 2. It is, therefore, clearly of interest to ascertain whether this assumption can be justified on physical and/or mathematical grounds.

It should be noted that this problem is not new, for it was first investigated by researchers studying the dynamics of fluids in porous media (Verruijt, 1969; Bear, 1988), particularly in the study of unsteady ground water flow in compressible soils. The appeal of the assumption $f = 0$ is due to the fact that the entire three-dimensional system of partial differential equations embodying consolidation theory (Biot, 1941), as well as mixture theory, is reduced to a single parabolic equation for the pore pressure. But despite many attempts, the hypothesis $f = 0$ could be justified only for a single case, namely that of cylindrical body satisfying the conditions of plane strain and axial symmetry, as shown by De Leeuw (1965).

First, the general relation between e and p, namely

$$p - (2\mu + \lambda)e = f, \tag{B1}$$

is employed to eliminate the gradient of e and p from the equation of motion, as follows. Assuming that $\underline{u}$ is radial symmetric, i.e., $\underline{u} = u(r)\underline{e_r}$, where $\underline{e_r}$ is the unit vector of the r component, and using spherical coordinates, equation (B1) is shown to imply

$$(2\mu + \lambda)\frac{\partial e}{\partial r} + \frac{\partial f}{\partial r} = \frac{\partial p}{\partial r}. \tag{B2}$$

Now, under the same assumption, the equation of motion (same as equation (A27) in Appendix A) becomes

$$\mu\left(\frac{2}{r}\frac{\partial u_r}{\partial r}+\frac{\partial^2 u_r}{\partial r^2}-\frac{2u_r}{r^2}\right)+(\mu+\lambda)\frac{\partial e}{\partial r}=\frac{\partial p}{\partial r}. \tag{B3}$$

The relation $e=\nabla\cdot\underline{u}$ can be written as

$$e=\frac{2u_r}{r}+\frac{\partial u_r}{\partial r}, \tag{B4}$$

and so

$$\frac{\partial e}{\partial r}=\frac{2}{r}\frac{\partial u_r}{\partial r}+\frac{\partial^2 u_r}{\partial r^2}-\frac{2u_r}{r^2}. \tag{B5}$$

This allows for the pressure gradient to be represented as

$$\frac{\partial p}{\partial r}=(2\mu+\lambda)\left(\frac{2}{r}\frac{\partial u_r}{\partial r}+\frac{\partial^2 u_r}{\partial r^2}-\frac{2u_r}{r^2}\right)+\frac{\partial f}{\partial r}. \tag{B6}$$

Substituting equations (B5) and (B6) into (B3) yields

$$\frac{\partial f}{\partial r}=\mu\left(\frac{2}{r}\frac{\partial u_r}{\partial r}+\frac{\partial^2 u_r}{\partial r^2}-\frac{2u_r}{r^2}\right)-\mu\left(-\frac{2u_r}{r^2}+\frac{2}{r}\frac{\partial u_r}{\partial r}+\frac{\partial^2 u_r}{\partial r^2}\right)=0 \tag{B7}$$

Thus, under radial symmetry assumed above, the harmonic function f depends only on time.

Furthermore, the assumption that all field quantities depend on r and t forces the solutions of $\nabla^2 f=0$ to be in the form

$$f(r,t)=\frac{a(t)}{r}+b(t), \tag{B8}$$

where $a(t)$ and $b(t)$ are arbitrary functions of time. However, since $\frac{\partial f}{\partial r}=0$, as shown in equation (B7), it follows that

$$\frac{\partial f}{\partial r}=-\frac{a(t)}{r^2}=0. \tag{B9}$$

This implies that $a(t)=0$ which results in

$$f=b(t), \tag{B10}$$

i.e., f being an arbitrary function of time.

Appendix C

Calculation of the analytic solution for the approximated case in Chapter 3

Referring to Chapter 3, Section 3.2, the Laplace inverse of solution (3.44), namely

$$P(r,s) = \frac{r_i\alpha\sinh(\sqrt{\frac{s}{\gamma}}(r_o - r)) + r_o\beta\sinh(\sqrt{\frac{s}{\gamma}}(r - r_i))}{rs\sinh(\sqrt{\frac{s}{\gamma}}(r_o - r_i))}, \qquad (C1)$$

can be computed analytically. The techinque used here is adopted from Powers (1999), pages 379-381, since rarely does the inverse Laplace of transcendental functions appears in a table of transforms. It is based on the following result:

Theorem

Let p and q be polynomials, q of lower degree than p, and let p have only simple roots, $r_1, r_2, ..., r_k$. Then

$$\mathcal{L}^{-1}\left(\frac{q(s)}{p(s)}\right) = \frac{q(r_1)}{p'(r_1)}e^{r_1 t} + \frac{q(r_2)}{p'(r_2)}e^{r_2 t} + ... + \frac{q(r_k)}{p'(r_k)}e^{r_k t}. \qquad (C2)$$

By extending the above theorem to transcendental functions, the inverse transform of Equation (C1) is computed in the following way.

Part A

When $r_0 = 0$, multiply equation (C1) by $s - r_0 = s$ to find A_0 and take the limit as s approaches r_0. The right hand side goes to A_0. On the left hand side,

$$\begin{aligned} A_0(r) &= \lim_{s\to 0} \frac{r_i\alpha\sinh(\sqrt{\frac{s}{\gamma}}(r_o - r)) + r_o\beta\sinh(\sqrt{\frac{s}{\gamma}}(r - r_i))}{r\sinh(\sqrt{\frac{s}{\gamma}}(r_o - r_i))} \\ &= \lim_{s\to 0} \frac{r_i(r_o - r)\alpha\cosh(\sqrt{\frac{s}{\gamma}}(r_o - r)) + r_o(r - r_i)\beta\cosh(\sqrt{\frac{s}{\gamma}}(r - r_i))}{r(r_o - r_i)\cosh(\sqrt{\frac{s}{\gamma}}(r_o - r_i))} \\ &= \frac{r_i(r_o - r)\alpha + r_o(r - r_i)\beta}{r(r_o - r_i)}. \end{aligned} \qquad (C3)$$

Thus, the portion of $p(r,t)$ corresponding to $s=0$ is

$$\frac{r_i(r_o-r)\alpha + r_o(r-r_i)\beta}{r(r_o-r_i)}, \tag{C4}$$

which is easily recognizable as the steady state solution.

Part B

When $r_n = \frac{-n^2\pi^2\gamma}{(r_o-r_i)^2}$ for $n=1,2,3,...$, the term $A_n(r)$ needs to be represented as

$$A_n(r) = \frac{q(r_n)}{u'(r_n)}. \tag{C5}$$

From equation (C1), the numerator is $q = r_i\alpha\sinh(\sqrt{\frac{s}{\gamma}}(r_o-r)) + r_o\beta\sinh(\sqrt{\frac{s}{\gamma}}(r-r_i))$, and the denominator is $u = rs\sinh(\sqrt{\frac{s}{\gamma}}(r_o-r_i))$. Take $\sqrt{r_n} = \frac{in\pi\sqrt{\gamma}}{(r_o-r_i)}$ in all the calculations. Then,

$$\begin{aligned} A_n(r) = \frac{q(r_n)}{u'(r_n)} &= \frac{r_i\alpha\sinh(\frac{r_o-r}{\sqrt{\gamma}}\frac{in\pi\sqrt{\gamma}}{(r_o-r_i)}) + r_o\beta\sinh(\frac{r-r_i}{\sqrt{\gamma}}\frac{in\pi\sqrt{\gamma}}{(r_o-r_i)})}{r\left[\sinh(\frac{r_o-r_i}{\sqrt{\gamma}}\frac{in\pi\sqrt{\gamma}}{(r_o-r_i)}) + \cosh(\frac{r_o-r_i}{\sqrt{\gamma}}\frac{in\pi\sqrt{\gamma}}{(r_o-r_i)})\right]} \\ &= \frac{r_i\alpha\sinh(\frac{r_o-r}{r_o-r_i}in\pi) + r_o\beta\sinh(\frac{r-r_i}{r_o-r_i}in\pi)}{r\left[\sinh(in\pi) + \frac{in\pi}{2}\cosh(in\pi)\right]}. \end{aligned} \tag{C6}$$

Using the identities $\sinh(ix) = i\sin(x)$ and $\cosh(ix) = \cos(x)$, equation (C6) becomes

$$\begin{aligned} A_n(r) &= \frac{r_i\alpha i\sin(\frac{r_o-r}{r_o-r_i}n\pi) + r_o\beta i\sin(\frac{r-r_i}{r_o-r_i}n\pi)}{r\left[\frac{in\pi}{2}\cos(n\pi)\right]} \\ &= \frac{2(-1)^n}{rn\pi}\left[r_i\alpha\sin\left(\frac{r_o-r}{r_o-r_i}n\pi\right) + r_o\beta\sin\left(\frac{r-r_i}{r_o-r_i}n\pi\right)\right]. \end{aligned} \tag{C7}$$

Hence, the portion of $p(r,t)$ that arises from each r_n is

$$A_n(r)\exp(r_nt) = \frac{2(-1)^n}{rn\pi}\left[r_i\alpha\sin\left(\frac{r_o-r}{r_o-r_i}n\pi\right) + r_o\beta\sin\left(\frac{r-r_i}{r_o-r_i}n\pi\right)\right]\exp\left(\frac{-(n\pi)^2\gamma}{(r_o-r_i)^2}t\right). \tag{C8}$$

Assembling the piece from *Part A* and *Part B* gives the full solution

$$\begin{aligned} p(r,t) = \alpha\frac{r_i}{r}&\left[\frac{r_o-r}{r_o-r_i} + \sum_{n=1}^{\infty}\frac{2(-1)^n}{n\pi}\sin\left(\frac{r_o-r}{r_o-r_i}n\pi\right)\exp\left(\frac{-(n\pi)^2\gamma}{(r_o-r_i)^2}t\right)\right] \\ + \beta\frac{r_o}{r}&\left[\frac{r-r_i}{r_o-r_i} + \sum_{n=1}^{\infty}\frac{2(-1)^n}{n\pi}\sin\left(\frac{r-r_i}{r_o-r_i}n\pi\right)\exp\left(\frac{-(n\pi)^2\gamma}{(r_o-r_i)^2}t\right)\right]. \end{aligned} \tag{C9}$$

Appendix D

Calculations of constants for the general solution in Chapter 3

In this Appendix, the details of the calculation of the constants needed in Chapter 3, Section 3.3 are given. Using the boundary conditions (3.83) and (3.85),

$$\begin{cases} P(q_i, s) = \frac{\alpha}{s}, \\ P(q_o, s) = \frac{\beta}{s}, \\ \tau_{rr}(q_i, s) = 0, \\ \tau_{rr}(q_o, s) = 0. \end{cases} \tag{D1}$$

together with equations (3.63) and (3.81)

$$P(q, s) = (2\mu + \lambda)\sqrt{\frac{\pi}{2q}}\left[A(s)I_{\frac{1}{2}}(q) + B(s)I_{-\frac{1}{2}}(q)\right] + G(s), \tag{D2}$$

and

$$\begin{aligned} \tau_{rr}(q, s) = {} & \lambda\sqrt{\frac{\pi}{2q}}\left[A(s)I_{\frac{1}{2}}(q) + B(s)I_{-\frac{1}{2}}(q)\right] \\ & + 2\mu\sqrt{\frac{\pi}{2q}}\left[A(s)\left(I_{\frac{1}{2}}(q) - \frac{2}{q}I_{\frac{3}{2}}(q)\right) + B(s)\left(I_{-\frac{5}{2}}(q) + \frac{1}{q}I_{-\frac{3}{2}}(q)\right)\right] - 4\sqrt{\frac{s}{\gamma}}\frac{C(s)}{q^3}, \end{aligned} \tag{D3}$$

one obtains four equations for the four unknown constants – $A(s)$, $B(s)$, $G(s)$, and $C(s)$:

$$\frac{\alpha}{s} = \underbrace{(2\mu + \lambda)\sqrt{\frac{\pi}{2q_i}}I_{\frac{1}{2}}(q_i)}_{\Gamma_i} A(s) + \underbrace{(2\mu + \lambda)\sqrt{\frac{\pi}{2q_i}}I_{-\frac{1}{2}}(q_i)}_{\Phi_i} B(s) + G(s); \tag{D4}$$

$$\frac{\beta}{s} = \underbrace{(2\mu + \lambda)\sqrt{\frac{\pi}{2q_o}}I_{\frac{1}{2}}(q_o)}_{\Gamma_o} A(s) + \underbrace{(2\mu + \lambda)\sqrt{\frac{\pi}{2q_o}}I_{-\frac{1}{2}}(q_o)}_{\Phi_o} B(s) + G(s); \tag{D5}$$

$$0 = \underbrace{\left[(2\mu+\lambda)I_{\frac{1}{2}}(q_i) - \frac{4\mu}{q_i}I_{\frac{3}{2}}(q_i)\right]}_{\Omega_i} A(s)$$
$$+ \underbrace{\left[\lambda I_{-\frac{1}{2}}(q_i) + 2\mu I_{-\frac{5}{2}}(q_i) + \frac{2\mu}{q_i}I_{-\frac{3}{2}}(q_i)\right]}_{\Lambda_i} B(s) - \underbrace{4\sqrt{s}\frac{1}{\sqrt{\gamma}}\frac{1}{{q_i}^3}\sqrt{\frac{2q_i}{\pi}}}_{M_i\sqrt{s}} C(s); \qquad (D6)$$

$$0 = \underbrace{\left[(2\mu+\lambda)I_{\frac{1}{2}}(q_o) - \frac{4\mu}{q_o}I_{\frac{3}{2}}(q_o)\right]}_{\Omega_o} A(s)$$
$$+ \underbrace{\left[\lambda I_{-\frac{1}{2}}(q_o) + 2\mu I_{-\frac{5}{2}}(q_o) + \frac{2\mu}{q_o}I_{-\frac{3}{2}}(q_o)\right]}_{\Lambda_o} B(s) - \underbrace{4\sqrt{s}\frac{1}{\sqrt{\gamma}}\frac{1}{{q_o}^3}\sqrt{\frac{2q_o}{\pi}}}_{M_o\sqrt{s}} C(s). \qquad (D7)$$

For simplicity, equations (D4)-(D7) are written as:

$$\frac{\alpha}{s} = \Gamma_i A(s) + \Phi_i B(s) + G(s); \qquad (D8)$$

$$\frac{\beta}{s} = \Gamma_o A(s) + \Phi_o B(s) + G(s); \qquad (D9)$$

$$0 = \Omega_i A(s) + \Lambda_i B(s) - M_i\sqrt{s}C(s); \qquad (D10)$$

$$0 = \Omega_o A(s) + \Lambda_o B(s) - M_o\sqrt{s}C(s). \qquad (D11)$$

Equations (D10) and (D11) can be rewritten as:

$$0 = \frac{\Omega_i}{M_i}A(s) + \frac{\Lambda_i}{M_i}B(s) - \sqrt{s}C(s); \qquad (D12)$$

$$0 = \frac{\Omega_o}{M_o}A(s) + \frac{\Lambda_o}{M_o}B(s) - \sqrt{s}C(s). \qquad (D13)$$

Now, equation (D8) is subtracted from (D9), and equation (D14) is subtracted from (D13) which yields:

$$(\Gamma_o - \Gamma_i)A(s) + (\Phi_o - \Phi_i)B(s) = \frac{\beta - \alpha}{s}, \qquad (D14)$$

and

$$\left(\frac{\Omega_o}{M_o} - \frac{\Omega_i}{M_i}\right)A(s) + \left(\frac{\Lambda_o}{M_o} - \frac{\Lambda_i}{M_i}\right)B(s) = 0, \qquad (D15)$$

respectively. The determinant of the linear system of equations (D14) and (D15) is

$$\Delta = (\Gamma_o - \Gamma_i)\left(\frac{\Lambda_o}{M_o} - \frac{\Lambda_i}{M_i}\right) - (\Phi_o - \Phi_i)\left(\frac{\Omega_o}{M_o} - \frac{\Omega_i}{M_i}\right). \quad (D16)$$

Solving for A(s) and B(s) yields

$$A(s) = \frac{\left(\frac{\beta-\alpha}{s}\right)\left(\frac{\Lambda_o}{M_o} - \frac{\Lambda_i}{M_i}\right)}{\Delta} = \frac{(\beta-\alpha)(\Lambda_o M_i - \Lambda_i M_o)}{s(M_i M_o)\Delta} = \frac{\overline{A}(s)}{s} \quad (D17)$$

and

$$B(s) = \frac{-\left(\frac{\beta-\alpha}{s}\right)\left(\frac{\Omega_o}{M_o} - \frac{\Omega_i}{M_i}\right)}{\Delta} = \frac{(\alpha-\beta)(\Omega_o M_i - \Omega_i M_o)}{s(M_i M_o)\Delta} = \frac{\overline{B}(s)}{s}, \quad (D18)$$

respectively. Finally, the constant G(s) is given by either

$$G(s) = \frac{\alpha}{s} - \Gamma_i A(s) - \Phi_i B(s), \quad (D19)$$

or

$$G(s) = \frac{\beta}{s} - \Gamma_o A(s) - \Phi_o B(s). \quad (D20)$$

(The constant $C(s)$ is not needed.) The expansion of equations (D17), (D18) and (D19) yields

$$A(s) = \frac{\overline{A}(s)}{s} = \frac{(\beta-\alpha)(\Lambda_o M_i - \Lambda_i M_o)}{s[(\Gamma_o - \Gamma_i)(\Lambda_o M_i - \Lambda_i M_o) - (\Phi_o - \Phi_i)(\Omega_o M_i - \Omega_i M_o)]}, \quad (D21)$$

$$B(s) = \frac{\overline{B}(s)}{s} = \frac{(\alpha-\beta)(\Omega_o M_i - \Omega_i M_o)}{s[(\Gamma_o - \Gamma_i)(\Lambda_o M_i - \Lambda_i M_o) - (\Phi_o - \Phi_i)(\Omega_o M_i - \Omega_i M_o)]}, \quad (D22)$$

and

$$G(s) = \frac{\overline{G}(s)}{s} = \frac{\alpha}{s} - \Gamma_i\left(\frac{(\beta-\alpha)(\Lambda_o M_i - \Lambda_i M_o)}{s[(\Gamma_o - \Gamma_i)(\Lambda_o M_i - \Lambda_i M_o) - (\Phi_o - \Phi_i)(\Omega_o M_i - \Omega_i M_o)]}\right) - \Phi_i\left(\frac{(\alpha-\beta)(\Omega_o M_i - \Omega_i M_o)}{s[(\Gamma_o - \Gamma_i)(\Lambda_o M_i - \Lambda_i M_o) - (\Phi_o - \Phi_i)(\Omega_o M_i - \Omega_i M_o)]}\right). \quad (D23)$$

Finally, plugging in equations (D21), (D22) and (D23) into equation (D2) gives the solution for the test case:

$$P(q,s) = (2\mu+\lambda)\sqrt{\frac{\pi}{2q}}\left[\frac{\overline{A}(s)}{s} I_{\frac{1}{2}}(q) + \frac{\overline{B}(s)}{s} I_{-\frac{1}{2}}(q)\right] + \frac{\overline{G}(s)}{s}. \quad (D24)$$

The constants are rather complicated. However, writing each modified Bessel function in terms of hyperbolic functions, or starting from scratch where solving the problem is done solely using hyperbolic functions, allows the constants to be slightly simplified. First, the

determinant of the system of equations (D4)-(D7), modified by the substitution $q_i = \sqrt{A}r_i$ and $q_o = \sqrt{A}r_o$, where $A = \frac{s}{\gamma}$, becomes:

$$\begin{aligned}\Delta_* = \frac{2\mu+\lambda}{A^{\frac{3}{2}}}\Bigg[&(2\mu+\lambda)A\sinh(\sqrt{A}(r_o-r_i))\left(\frac{r_i^2}{r_o}-\frac{r_o^2}{r_i}\right)\\&+4\mu\sinh(\sqrt{A}(r_o-r_i))\left(\frac{1}{r_o}-\frac{1}{r_i}\right)\\&+4\mu A^{\frac{1}{2}}\cosh(\sqrt{A}(r_o-r_i))\left(\frac{r_i}{r_o}+\frac{r_o}{r_i}\right)-8A^{\frac{1}{2}}\mu\Bigg].\end{aligned} \tag{D25}$$

Then, with $A(s)$, $B(s)$ and $G(s)$ written using hyperbolic functions,

$$\begin{aligned}A(s)_* = \frac{\beta-\alpha}{sA^{\frac{3}{2}}\Delta_*}\Big[&(2\mu+\lambda)A(r_i^2\cosh(\sqrt{A}r_i)-r_o^2\sinh(\sqrt{A}r_o))\\&+4\mu(\cosh(\sqrt{A}r_i)-\cosh(\sqrt{A}r_o))-4\mu\sqrt{A}(r_i\sinh(\sqrt{A}r_i)-r_o\sinh(\sqrt{A}r_o))\Big];\end{aligned} \tag{D26}$$

$$\begin{aligned}B(s)_* = \frac{\alpha-\beta}{sA^{\frac{3}{2}}\Delta_*}\Big[&(2\mu+\lambda)A(r_i^2\sinh(\sqrt{A}r_i)-r_o^2\sinh(\sqrt{A}r_o))\\&+4\mu(\sinh(\sqrt{A}r_i)-\sinh(\sqrt{A}r_o))-4\mu\sqrt{A}(r_i\cosh(\sqrt{A}r_i)-r_o\cosh(\sqrt{A}r_o))\Big];\end{aligned} \tag{D27}$$

and, the constant $G(s)_*$ has two possible forms, one of which is

$$\begin{aligned}G(s)_* = \frac{\alpha}{s}+\frac{(2\mu+\lambda)(\alpha-\beta)}{sr_iA^{\frac{3}{2}}\Delta_*}\Big[&(2\mu+\lambda)Ar_o^2\sinh(\sqrt{A}(r_o-r_i))\\&+4\mu\sinh(\sqrt{A}(r_o-r_i))+4\mu\sqrt{A}(r_i-r_o\cosh(\sqrt{A}(r_o-r_i))\Big]\end{aligned} \tag{D28}$$

Now, substituting (D26), (D27) and (D28) into the equation (3.63) in Chapter 3, Section 3.3, with $q = \sqrt{A}r$, yields

$$P(r,s) = (2\mu+\lambda)\left[\frac{A(s)_*}{r\sqrt{A}}\sinh(\sqrt{A}r)+\frac{B(s)_*}{r}\cosh(\sqrt{A}r)\right]+G(s)_*\ . \tag{D29}$$

Simplifying further, the Laplace-transformed expression for the test case in terms of hyperbolic functions is

$$\begin{aligned}P(r,s) = \frac{(2\mu+\lambda)(\alpha-\beta)}{sA^{\frac{3}{2}}\Delta_*}\Bigg[&\frac{1}{r}\Big\{(2\mu+\lambda)A\left[r_i^2\sinh(\sqrt{A}(r_i-r))-r_o^2\sinh(\sqrt{A}(r_o-r))\right]\\&+4\mu\left[\sinh(\sqrt{A}(r_i-r))-\sinh(\sqrt{A}(r_o-r))\right]\\&-4\mu\sqrt{A}\left[r_i\cosh(\sqrt{A}(r_i-r))-r_o\cosh(\sqrt{A}(r_o-r))\right]\Big\}\\&+\frac{1}{r_i}\Big\{(2\mu+\lambda)Ar_o^2\sinh(\sqrt{A}(r_o-r_i))\\&+4\mu\sinh(\sqrt{A}(r_o-r_i))+4\mu\sqrt{A}(r_i-r_o\cosh(\sqrt{A}(r_o-r_i))\Big\}\Bigg]+\frac{\alpha}{s}.\end{aligned} \tag{D30}$$

Equation (D30) is still messy; however, it is more manageable than the one that uses Bessel functions.

References

M. Abramowitz and I. A. Stegun. *Handbook of Mathematical Functions With Formulas, Graphs, and Mathematical Tables.* National Bureau of Standards Applied Mathematics Series, Washington, 1964.

A. L. Albright, I. F. Pollack, and P. D. Adelson. *Principles and practice of pediatric neurosurgery.* Thieme New York, New York, 1999.

G. H. Algire and H. W. Chalkley. Vascular reactions of normal and malignant tissues in vivo. I. Vascular reactions of mice to wounds and to normal and neoplastic transplants. *J. Nati. Cancer Inst.*, 6:73-85, Aug 1945.

D. O. Bates and F. E. Curry. Vascular endothelial growth factor increases hydraulic conductivity of isolated perfused microvessels. *Am. J. Physiol. Society (Heart Circ. Physiol.)*, 271:H2520-H2528, Dec 1996.

L. T. Baxter and R. K. Jain. Transport of fluid and macromolecules in tumors I. Role of interstitial pressure and convection. *Microvasc. Res.*, 37:77-104, Jan 1989.

J. Bear, *Dynamics of Fluids in Porous Media.* American Elsevier Publishing Company, Inc., New York, 1988.

J. Bear and A. Verruijt, *Modeling groundwater flow and pollution.* D. Reidel Publishing Company, New York, 1987.

M. A. Biot. General theory of three-dimensional consolidation. *J. Appl. Phys.*, 12:155-164, Feb 1941.

M. A. Biot and D. G. Willis. The Elastic Coefficients of the Theory of Consolidation. *J. Appl. Mech.*, 24:594-598, Dec 1957.

Y. C. Boucher, L. T. Baxter, and R. K. Jain. Interstitial Pressure Gradients in Tissue-Isolated and Subcutaneous Tumors: Implications for Therapy. *Cancer Res.*, 50:4478-4484, Aug 1990.

J. E. Bowles. *Foundation analysis and design, fourth edition.* McGraw-Hill Book Company, New York, 1988.

P. Carmeliet and R. K. Jain. Molecular mechanisms and clinical applications of angiogenesis. *Nature*, 473:298-307, Sep 2011.

Y. S. Chang, L. L. Munn, M. V. Hillsley, R. O. Dull, J. Yuan, S. Lakshminarayanan, T. W. Gardner, R. K. Jain, and J. M. Tarbell. Effect of vascular endothelial growth factor on cultured endothelial cell monolayer transport properties. *Microvasc Res*, 59:26577, Mar 2000.

B. D. Curti, W. J. Urba, W. G. Alvord, J. E. Janik, J. W. Smith II, K. Madara, and D. L. Longo. Interstitial pressure of subcutaneous nodules in melanoma and lymphoma patients: changes during treatment. *Cancer Res*, 53:2204-2207, May 1993.

R. de Boer. *Theory of Porous Media. Highlights in the Historical Development and Current Status.* Springer, New York, 2000.

E. H. De Leeuw. The Theory of Three-dimensional Consolidation Applied to Cylindrical Bodies. *Proceedings of the 6th Int. Conf. of Soil Mechanics and Foundation Eng.*, 1:287-290, 1965.

Y. C. Fung. *Biomechanics.* Springer-Verlag, New York, 1990.

J. Ghajar. Traumatic brain injury. *The Lancet*, 356:923-929, Sep 2000.

S. Goel, D. G. Duda, L. Xu, L. L. Munn, Y. Boucher, D. Fukumura, and R. K. Jain. Normalization of the vasculature for treatment of cancer and other disease. *Physiol. Rev.*, 91:1071-1121, Jul 2011.

P. M. Gullino. Angiogenesis and oneogenesis. *J Nat Cancer Inst*, 61:639-643, 1976.

P. M. Gullino, S. H. Clark, and F. H. Grantham. The interstitial fluid of solid tumors. *Cancer Res*, 24:780-797, Jun 1964.

R. Gutmann, M. Leunig, J. Feyh, A. E. Goetz, K. Messmer, E. Kastenbauer, and R. K. Jain. Interstitial hypertension in head and neck tumors in patients: correlation with tumor size. *Cancer Res.*, 52:1993-1995, Apr 1992.

C. H. Heldin, K. Rubin, K. Pietras, and A. Ostman. High interstitial fluid pressure – an obstacle in cancer therapy. *Nature Rev., Cancer*, 4:806-813, Oct 2004.

R. K. Jain. Transport of molecules in the tumor interstitium: A review. *Cancer Res.*, 47:3039-3051, Jun 1987a.

R. K. Jain. Transport of molecules across tumor vasculature. *Cancer Metastasis Rev.*, 6:559-594, Dec 1987b.

R. K. Jain. Normalizing tumor vasculature with anti-angiogenic therapy: a new paradigm for combination therapy. *Nat. Med.*, 7:987-989, Sep 2001.

R. K. Jain. Molecular regulation of vessel maturation. *Nat. Med.*, 9:685-693, 2003.

R. K. Jain. Normalization of tumor vasculature: an emerging concept in antiangiogenic therapy. *Science.*, 307:58-62, 2005.

R. K. Jain. Taming vessels to treat cancer. *Scientific American.*, 298:56-63, Jan 2008.

R. K. Jain and L. T. Baxter. Mechanisms of heterogeneous distribution of monoclonal antibodies and other macromolecules in tumors: Significance of elevated interstitial pressure. *Cancer Res.*, 48:7022-7032, Dec 1988.

R. K. Jain, R. T. Tong, and L. L. Munn. Effect of Vascular Normalization by Antiangiogenic Therapy on Interstitial Hypertension, Peritumor Edema, and Lymphatic Metastasis: Insights from a Mathematical Model. *Cancer Res.*, 67:2729-2715, Mar 2007.

D. E. Kenyon. Transient filtration in a porous elastic cylinder. *ASME J. Appl. Mech.*, 43:594-598, Dec 1976a.

D. E. Kenyon. The theory of an incompressible solid-fluid mixture. *Arch. Rat. Mech. Anal.*, 62:131-147, Jun 1976b.

H. Khosravani, B. Chugh, M. F. Milosevic, and K. H. Norwich. Time response of interstitial fluid pressure measurements in cervix cancer. *Microvascular Res.*, 68:63-70, Jul 2004.

J. R. Less, M. C. Posner, Y. Boucher, D. Borochovitz, N. Wolmark, and R. K. Jain. Interstitial hypertension in human breast and colorectal tumors. *Cancer Res*, 52:6371-6374, Nov 1992.

D. N. Levine. The pathogenesis of normal pressure hydrocephalus: A theoretical analysis. *Bull. Math. Biol.*, 61:875-916, Sep 1999.

S. J. Lunt, A. Fyles, R. P. Hill, and M. Milosevic. Interstitial fluid pressure in tumors: therapeutic barrier and biomarker of angiogenesis. (Report). *Future Oncology*, 10:793-805, Dec 2008.

M. Milosevic, S. J. Lunt, E. Leung, J. Skliarenko, P. Show, A. Fyles, and R. P. Hill. Interstitial permeability and elasticity in human cervix cancer. *Microvascular Res*, 75:381-390, Nov 2008.

S. D. Nathanson and L. Nelson. Interstitial fluid pressure in breast cancer, benign breast conditions, and breast parenchyma. *Ann Surg Oncol.*, 1:333-338, 1994.

P. A. Netti, L. T. Baxter, Y. Boucher, R. Skalak, and R. K. Jain. Time-dependent behavior of interstitial fluid pressure in solid tumors: implications for drug deliver. *Cancer Res.* 55:5451-5458, Nov 1995.

P. A. Netti, L. T. Baxter, Y. Boucher, R. Skalak, and R. K. Jain. Macro- and Microscopic Fluid Transport in Living Tissues: Application to Solid Tumors. *AIChE Journal*, 43:818-834, Mar 1997.

J. Nolte. *The human brain: An introduction to its functional anatomy.* The C. V. Mosby Company, Toronto, 1981.

T. M. Pocock, R. R. Foster, and D. O. Bates. Evidence of a role for TRPC channels in VEGF-mediated increased vascular permeability in vivo. *Am J Physiol Heart Circ Physiol*, 286:H1015H1026, Oct 2003.

D. L. Powers. *Boundary value problems, fourth edition.* Harcourt/Academic Press, New York, 1999.

P. H. Schurr and C. E. Polkey. *Hydrocephalus.* Oxford University Press, New York, 1993.

B. R. Simon. Multiphase poroelastic finite element models for soft tissue structures. *Appl. Mech. Rev.*, 45:191-217, 1992.

A. Smillie, I. Sobey, and Z. Molnar. A hydroelastic model of hydrocephalus. *J. Fluid Mech.*, 539:417-443, Apr 2005.

I. Sobey and B. Wirth. Effect of non-linear permeability in a spherically symmetric model of hydrocephalus. *Mathematical Medicine and Biology*, 23:339361, 2006.

Z. Taylor and Z. Miller. Reassessment of Brain Elasticity for Analysis of Biomechanisms of Hydrocephalus. *Journal of Biomechanics*, 37:1263-1269, Aug 2004.

G. Tenti, J. M. Drake, and S. Sivaloganathan. Brain biomechanics: mathematical modeling of hydrocephalus. *Neurol. Res.*, 22:19-24, Jan 2000.

Terzaghi, K. *Theoretical Soil Mechanics.* John Wiley and Sons, New York, 1943.

R. T. Tong, Y. Boucher, S. V. Kozin, F. Winkler, D. J. Hicklin, and R. K. Jain. Vascular Normalization by Vascular Endothelial Growth Factor Receptor 2 Blockade Induces a

Pressure Gradient Across the Vasculature and Improves Drug Penetration in Tumors. *Cancer Res.*, 64:3731-3736, Jun 2004.

A. Verruijt. *Flow Through Porous Media (R.J.M. De Wiest, ed.).* Academic Press, New York, 1969.

A. Verruijt. *Theory of groundwater flow.* Gordon and Breach Science Publishers Inc., New York, 1970.

D. V. Widder. *Advanced Calculus, Second Edition.* Dover Publications, Inc., Mineola, 1989.

J. S. Young, C. E. Lumsden, and A. L. Stalker. The significance of the "tissue pressure" of normal testicular and of neoplastic (Brown-Pearce carcinoma) tissue in the rabbit. *J. Pathol. Bacteriol.*, 62:313-333, Jul 1950.